# OPTIMIZATION OF WIND AUGMENTERS FOR URBAN POWER GENERATION

by

Hans Hamm, B. Eng Aerospace

Ryerson University, 2003

A thesis

presented to Ryerson University

in partial fulfillment of the requirements for the degree of

Master of Applied Science

in the Program of Mechanical Engineering

Toronto, Ontario, Canada, August ©

I hereby declare that I am the sole author of this thesis or dissertation. I authorize Ryerson University to lend this thesis or dissertation to other institutions or individuals for the purpose of scholarly research.

Signature:

I further authorize Ryerson University to reproduce this thesis or dissertation by photocopying or by other means, in total or in part, at the request of other institutions or individuals for the purpose of scholarly research.

Signature:

# Abstract

Hans Hamm, Master of Applied Science, 2006

Wind power is the most available renewable energy source to date due to the relatively low costs and advances in the field. Consequently, there is a high demand for innovative wind technology. Furthermore, providing energy near consumers, such as in inner city dwellings and urban settings, provides a more efficient and more reliable energy source. The use of architecture to augment wind energy extraction is still unresolved and the area of research is still in its infancy. The few studies conducted have shown substantial benefits by using buildings to collect wind to increase the power efficiency of wind turbines beyond the Betz limit. This study utilized computational fluid dynamics to analyze building shapes to optimize wind turbine power production. Results indicate an increase in power of up to approximately $4-8$ times compared to that for the undisturbed free stream flow. Furthermore, a porous medium was used to simulate the momentum loss due to the presence of the wind turbine. The trends remained similar despite the momentum loss caused by the presence of the wind turbine. The porous medium results showed an increase of power approximately $2-3$ times. The study extended the geometry to 3D to support the 2D results. The test case indicated the 3D results had a higher performance in comparison to 2D due to the 3D interactions of the vortex shedding dampening the variance of velocity in the gap region. Furthermore, a certain geometry performs better at different angles of attack proving the optimal geometry will be specifically tailored to

the typical wind directions associated with the desired building location.

# Acknowledgements

I would like to acknowledge Dr. Paul Walsh for his personal and academic guidance. He has been a great inspiration and mentor during my entire university career. I would also like to acknowledge my grandfather Carl, my mother Ingrid and father Hans Sr. for their support and encouragement. Last and not least my friends, in particular Dr. Rob Kriz, Melissa Rush, Laura Herbert, Doug Herbert and Jon Bahen for being great comrades. They have helped me to stay healthy both mentally and physically. I love all of you!

# Table of Contents

# List of Figures

# List of Tables

# Nomenclature

$t$ - Time
$u_i$, $u_j$ - Velocity in tensor notation
$x_i$, $x_j$ - Direction in tensor notation
$u$ - General velocity
$\bar{u}$ - Mean velocity
$u'$ - Fluctuating component of velocity
$p$ - Pressure
$\bar{p}$ - Mean pressure
$p'$ - Fluctuating component of pressure
$T$ - Temperature
$\bar{T}$ - Mean temperature
$T'$ - Fluctuating component of temperature
$\rho$ - Density
$\nu$ - Kinematic viscosity
$\mu$ - Viscosity
$e$ - Internal energy
$k$ - Thermal conductivity coefficient
$\Phi$ - Rate of dissipation of mechanical energy per unit mass
$Sr$ - Strouhal number
$Re$ - Reynolds number
$f_r$ - Frequency of shedding cycle
$L$ - Characteristic length
$V_o$ - Wind velocity
$\tau_{i,j}$ - Molecular stresses
$\phi$ - Conserved variable
$S_\phi$ - Source term
$\Gamma_{phi}$ - Diffusion parameter
$A$ - Surface area
$\forall$ - Volume
$N_{faces}$ - The number of faces enclosing cell
$\phi_f$ - The value of $\phi$ convected through face $f$

$\rho_f \vec{v_f} \cdot \vec{A_f}$ - The mass flux through the face $f$
$\vec{A_f}$ - Area of the face $f$
$(\nabla\phi)_n$ - The magnitude of $\nabla\phi$ normal to face $f$
$\mu_t$ - Turbulent viscosity
$\bar{\nu}$ - Transport variable
$G_\nu$ - Production of turbulent viscosity
$Y_\nu$ - Destruction of turbulent viscosity
$S_{\bar{\nu}}$ - User defined source term
$\sigma_{\bar{\nu}}$, $C_{D2}$ - Spalart Allmaras constants
$f_{v1}$ - Viscous dampening function
$\chi$ - Ratio of transport variable $\bar{\nu}$ over kinematic viscosity $\nu$
$C_{b1}$, $\kappa$ - Turbulent production constants in Spalart-Allmaras model
$d$ - Distance from the wall in
$S$ - Deformation tensor based on magnitude of vorticity
$\Sigma_{i,j}$ - mean rate-of-rotation tensor
$C_{w2}$, $C_{w3}$ - Turbulent destruction constants
$\mu_o$ - Reference viscosity
$T_o$ - Reference temperature
$S$ - Effective temp / Sutherland constant
$y^+$ - Y-Plus function
$u_T$ - Friction velocity
$y_p$ - distance from point $P$ to the wall
$P$ - node located adjacent to the wall
$A$, $B$, $C$, $D$ - Enclosed spline points
$a$, $A_1$, $A_2$, $g$, $b_x$ - Enclosed spline parameters
$S^2$ - Variance
$\bar{X}$ - Mean
$N$ - Number of data points
$X$ - Data value

# Chapter 1

# Introduction

Wind power is one of the most promising renewable energy sources available, due to technical advances in the field and its relatively low cost. The use of wind turbines has been popular in Europe for decades, supplying sustainable energy to its citizens, notably Denmark, Germany and Spain which gets 20% of it's electricity, reported by The European Wind Energy Association [1]. Wind power generation is becoming increasingly popular in North America due to the rising costs of fossil fuels and demands for clean energy; thus, innovative wind energy sources will become an expanding area of research. A global break down of the wind power markets are shown in Figure 1.1, provided by the Global wind Energy Council [2].

The history of the use of non-renewable fossil fuels is believed to follow a bell shape curve and the peak is defined as Hubbert's peak. Early in the curve, the pre-peak, the production of oil increases due to the addition of infrastructure. Late in the curve or post-peak, the production declines due to resource depletion. It has been stated by Caltech's physicist Dr. Goodstein [3] that Hubbert's peak phenomena will most likely occur as early as this decade and no later than the next decade. After Hubbert's peak, the fossil fuel resources availability will forever decline and increase in price. Thus, it is important to

TOP TEN WIND POWER MARKETS 2004: CUMULATIVE MW INSTALLED

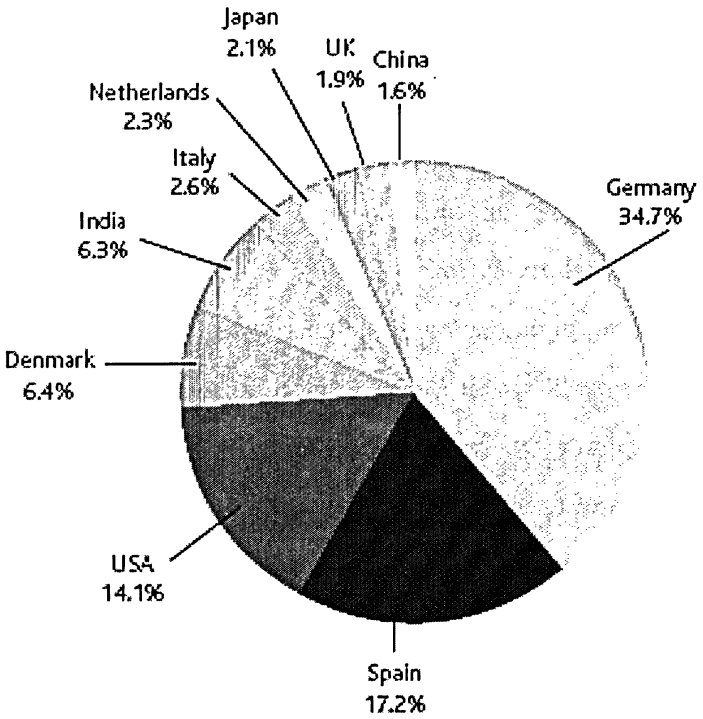


| Country | Total capacity End 2004 (MW) |
|---|---|
| Germany | 16,649 |
| Spain | 8,263 |
| USA | 6,750 |
| Denmark | 3,083 |
| India | 3,000 |
| Italy | 1,261 |
| Netherlands | 1,081 |
| Japan | 991 |
| UK | 889 |
| China | 769 |
| **Total** | **42,735** |

**Source : GWEC**

Figure 1.1: Global Wind Energy Market Statistics [2]

start developing more energy sources to ensure our society has an alternative to fossil fuel resources.

If a point in time is reached were fossil fuel sources become too expensive for every day use, there are few technologies that will provide the same reliability, mobility and power that fossil fuels currently offer. The world of interconnected highways and airways that are relied upon on a daily basis will be prohibitively expensive as fuel prices sore. It is not feasible to think that wind energy will be the ultimate answer to the emerging energy crisis, but it could begin to reduce the demand for coal and oil burning power plants today, reducing the dependence on fossil fuels.

Wind is the most accessible renewable energy since its available to all people and has the potential to be used as an embedded source. Embedded power generation focuses on shifting the power production from large centralized plants to smaller facilities that are closer to their points of use. Using wind turbines in the urban environment has been promoted by a number of researchers, Campbell *et al* [4], Grant and Kelly [5], Igra [6] and Kogan [7], using various methods.

A number of techniques have been explored to develop urban wind turbines. An area of research not yet thoroughly explored and optimized is the integration of wind turbines into large architectural structures. Integrated wind turbines into high-rise structures may play a vital role in creating this paradigmatic shift by utilizing pressure differentials created by buildings to increase power production. This thesis is focused on developing a new concept of the way in which buildings are designed and shaped in order to optimize this effect.

## 1.1 Literature Review

### 1.1.1 The Betz Limit

Wind turbines extract energy from the wind by removing some of its kinetic energy. The maximum amount of energy that can be extracted from the wind is approximately 59.3% of its original kinetic energy, a concept that was determined by Betz back in 1919 [9], and is appropriately termed the Betz limit. This limit has become a common benchmark for estimating maximum efficiencies when designing wind farms. Betz used the one dimensional Bernoulli relation to model turbines in an incompressible fluid. He assumed the turbine was in constant, uniformly distributed pressure, with constant velocity. Furthermore he was assumed no rotational affects or tip losses. Using a ratio of turbine power, to the power of uninterrupted flow, he was able to determine a maximum efficiency. Referring to Figure 1.2, he defined $V_1$ as the undisturbed air before the wind turbine and $V_2$ as the wind after the wind passed through the wind turbine. Thus, the average wind speed at the turbine is,

$$V = \frac{V_1 + V_2}{2} \tag{1.1}$$

where the mass flow through the turbine is,

$$\dot{m} = \rho A_R V \tag{1.2}$$

where, $A_R$ is the rotor sweeping area. The power extracted by the turbine is equal to the change in kinetic energy.

$$P = 1/2\dot{m}V_1^2 - 1/2\dot{m}V_2^2 = 1/2\dot{m}(V_1^2 - V_2^2) \tag{1.3}$$

Substituting in equation 1.2 into equation 1.3 results in,

$$P = 1/2\rho A_R(V_2 + V_1)(V_1^2 - V_2^2) \tag{1.4}$$

where the power of the undisturbed air is,

$$P_o = \frac{\rho A_R V_1^3}{2} \tag{1.5}$$

Betz then defined the ratio of turbine power over the power uninterrupted flow so,

$$\frac{P}{P_o} = PR = \frac{1}{2}(1 - VR^2)(1 + VR) \tag{1.6}$$

where, $PR$ is the power ratio and $VR = V_2/V_1$ is the velocity ratio. Differentiating equation 1.6 with respect to the $VR$ and equating equal to zero results in the optimal $PR$,

$$VR = \frac{V_2}{V_1} = \frac{1}{3} \tag{1.7}$$

which is clearly seen in Figure 1.3. Substituting back into equation 1.6 results in,

$$PR = \frac{16}{27} \approx 0.593 \tag{1.8}$$

for optimal power.

If the wind turbines could extract 100% of the energy, the wind would stop all together, causing the wind to flow around the turbines. If a turbine had no blades, no blockage would result but no power would be produced. Therefore, a maximum exists corresponding to the Betz limit. However, due to mechanical losses, the efficiency of a lift type turbine is more typically around 35 % to 45 %. Furthermore, due to energy transmission, the generator and storage devices, the energy extracted drops to 10% to 30 % of the original energy available in the wind. However, using ducted or shrouded wind

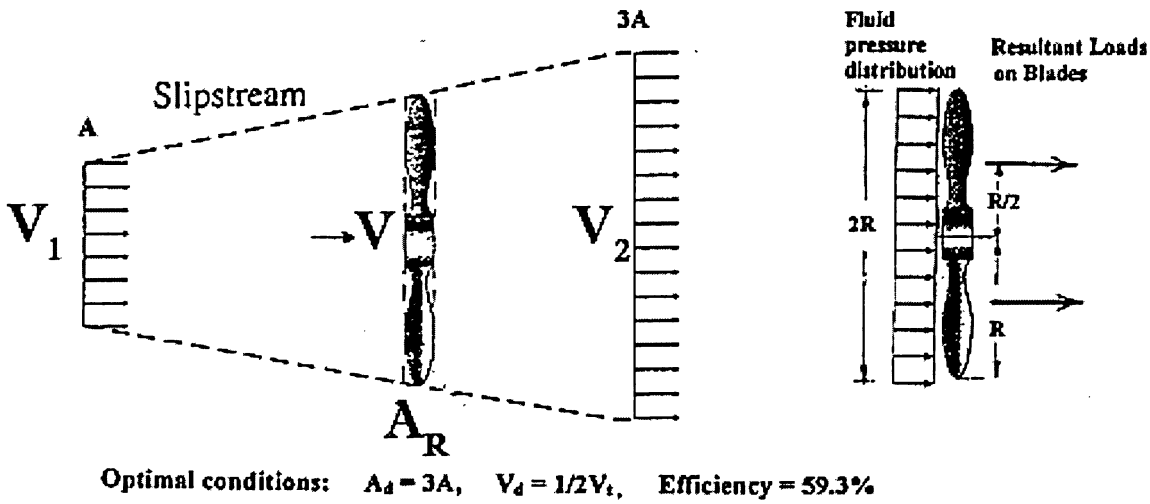


Figure 1.2: Betz Limit [10]

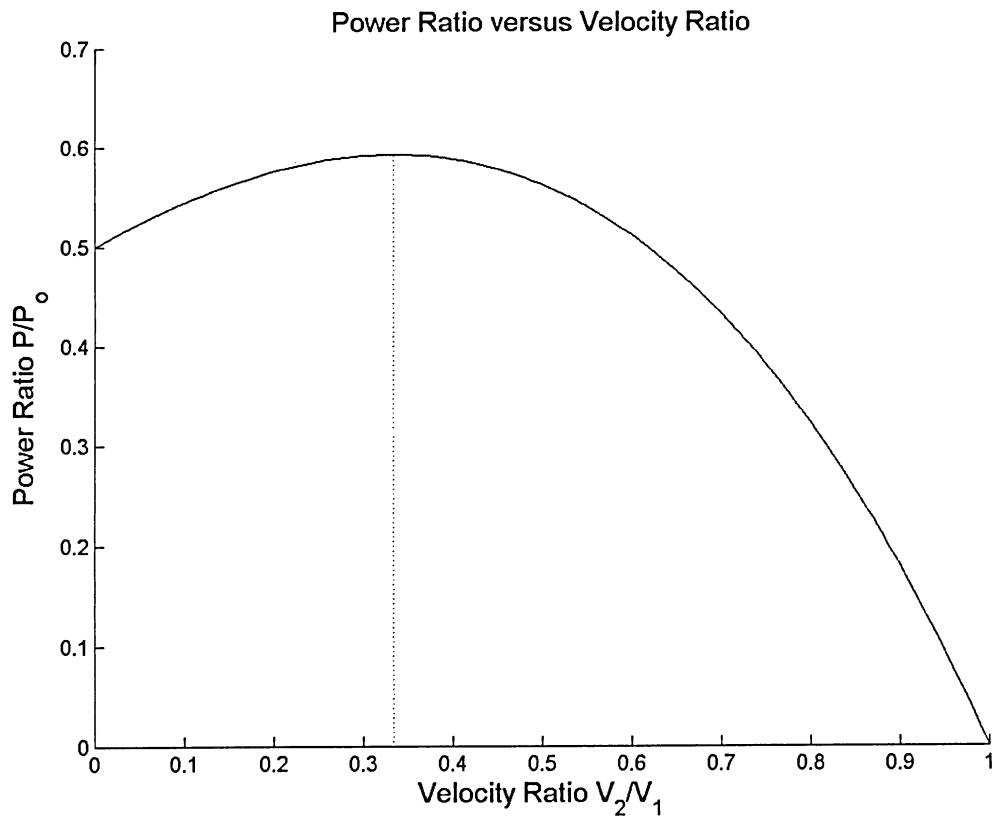


Figure 1.3: Power Ratio versus Velocity Ratio

turbines, the efficiency can be increased beyond the Betz limit to compensate. By using augmentation devices more flow is drawn into the turbine, increasing the energy density of the flow and therefore increasing the power production. However, the turbine itself cannot extract more than the Betz limit but across the augmentation device it can.

### 1.1.2 Lift Type Wind Turbines

Wind turbines fall under two categories: drag type and lift type. Lift type wind turbines are preferred over drag type since for a given sweeping area a lift type turbine can produce more power. Lift type wind turbines use airfoils to generate lift. A portion of this lifting force is canted in the rotation direction causing the turbine to spin. A drag type wind turbine uses an object's aerodynamic drag in a moving fluid to generate power. Therefore, drag type turbines are limited by the speed of the wind resulting in low rotation rates, while lift type turbines can produce higher rotation rates and in turn create more power.

The first lift type wind rotor to produce electricity was developed in 1891 by Dane Poul La Cour using primitive airfoils [11]. However, by 1918, fossil-fuel steam plants produced cheaper energy, overshadowing the wind energy business. Large scale wind energy production was initiated by the Russians in 1931 with the Balaclava Wind generator producing about 200 000 kWh during its two year operation [12]. The development of light weight airframe technology in the aeronautical industry greatly improved wind turbine efficiency. Further advances in the field were pioneered by a German professor, Dr. Ulrich Hutter, using ultra-light horizontal-axis designs built from fiberglass and plastics [13]. The primary purpose of his research was to reduce bearing and structure failures caused by loads associated with vortex shedding. The most innovative design by Dr. Hutter was a rotor that teetered to wind gusts and wind shear, greatly increasing the lifespan of the wind turbine. Greater strides in efficiency for both the vertical and horizontal axis wind turbines were initiated by the US government in response to the 1973 oil embargo.

Included in this research, was shrouded and augmented wind turbines discussed in more detail in subsequent sections. However, by 1981 most of the research funding ceased and was reallocated as tax breaks for wind energy producers [11].

### 1.1.3 Shrouded Wind Turbines

The use of augmentation to increase energy extraction has been widely studied since the early 60's [6]-[7]. There are three primary benefits to use shrouding: 1) reduce blade size, 2) increase rotational speed, 3) reduce tip losses. For example, the power obtained from shrouded turbines can be as high as 3.5 times the maximum power available from an ideal turbine, of equal diameter under the same conditions, as reported by Kogan and Seginer [8]. However, the design suggested by Kogan and Seginer is unrealistic for commercial use since the length of the shroud to turbine diameter is 7:1, making the augmentation structure so enormous that it is economically unrealistic for development. Further revisions to shrouded designs have been able to reduce the shroud length to turbine diameter ratio of 3:1, by using high lift airfoils and high lift devices suggested by Igra [6], while still increasing the power by almost 2.3 times, shown in Figure 1.4. Since these shrouds are essentially circular wings, the increase in power obtained is directly related to the cross-sectional lift of the shroud itself, studied extensively by Fletcher [15]. He showed that by increasing the angle of incidence the shroud actually increased the lift on the airfoil by creating a low pressure region in the center of the circular wing, drawing more air through the center and in-turn increasing the power output of the turbine, up until stall angle. Furthermore, by using flap devices to increase the exit area, a maximum power ratio of 2.3 is obtained at $0^o$ angle of incidence. However, these flap devices also increased the camber of the airfoil such that if the angle of incidence varies beyond 0 degrees, a substantial power loss occurs, due to separation. Although the size of the shroud can still be reduced, the development of such structures and associated high lift devices would still be very expensive. It would be more advantageous to use existing structures in some manner to

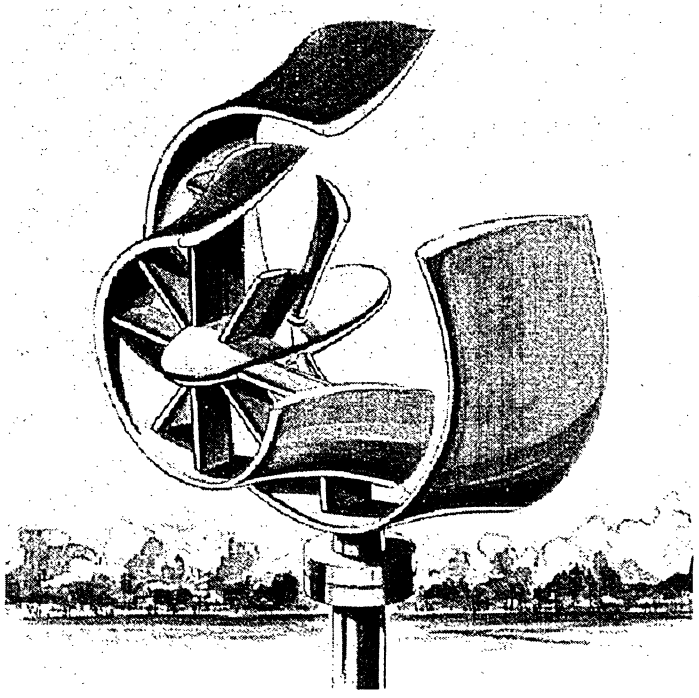

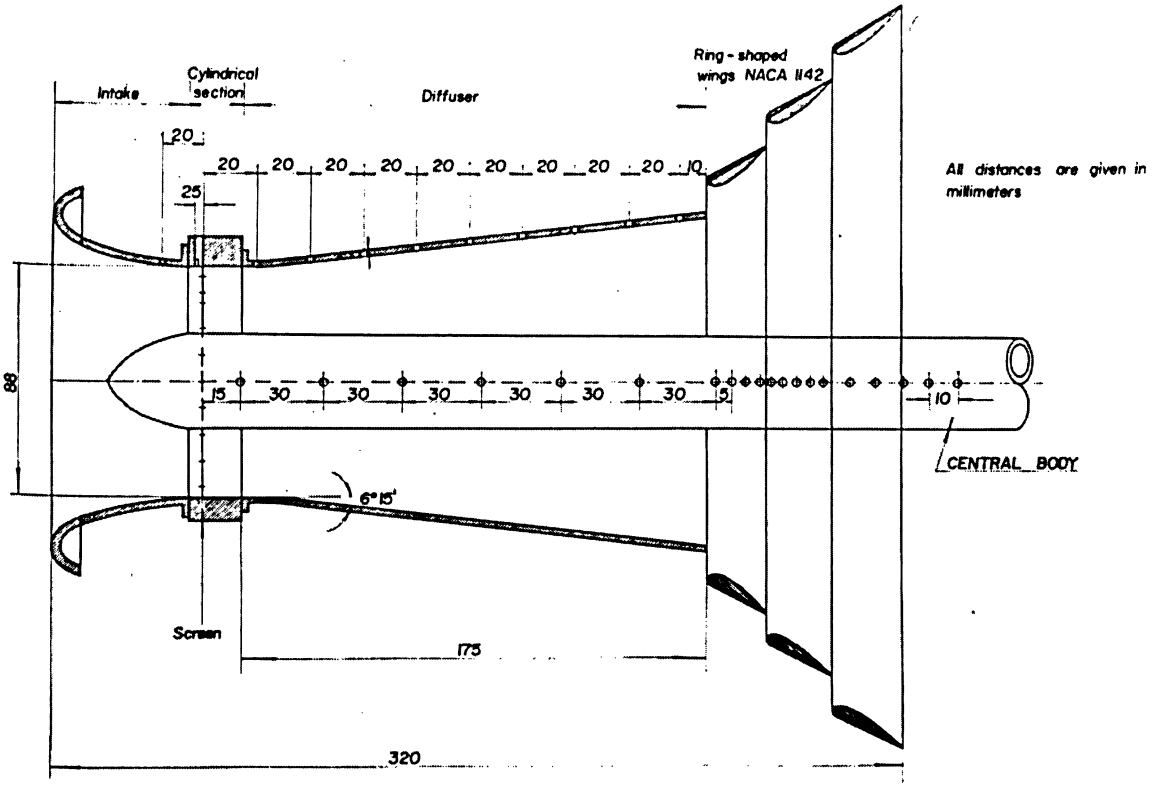


Figure 1.4: Shrouded Wind Turbine(Top) [14] and Short diffuser type using high lift devices (Bottom) [6]

create the same effect. The use of architecture in this manner is beneficial since structure sizes are large (to increase the wind tunnel effect) and the structure itself is utilized for residential and commercial dwellings, serving a dual purpose.

### 1.1.4 Ducted Wind Turbines

Ducted wind turbines is another technology used to increase the efficiency of wind power generation by utilizing the pressure differences that exist between architectural surfaces, shown in Figure 1.5. The ducted wind turbine was first suggested by Webster in 1979 [14] which is considered a micro-grid technology. This is a small wind energy conversion device that can be integrated into the facade of a building and may be a useful means of producing energy to sustain part of the buildings power demands. Some mathematical models developed by Grant and Kelly [5] used rectangular cross-section ducts that are integrated into roof edges of rectangular-section buildings, which improved the power coefficient well beyond the Betz limit ($C_p = 0.597$) to approximately $C_p = 1.5$. The reason behind the considerable increase in power is directly related to the pressure differential created by the flow over the building in contrast to conventional wind turbines where the pressure is created by the airflow through the wind turbine blades itself. These models showed ducted wind turbines as a good potential source for micro-grid power production and is comparable to the energy yields from photo voltaic materials as reported by Grant and Kelly [5].

### 1.1.5 Architecturally Augmented Wind Turbines

Architecturally augmented wind turbines use the same approach as ducted wind turbines in that they utilizes the pressure differentials created by buildings to increase the efficiency of wind turbines. The augmentation of wind turbines using architecture, can be done by retro-fitting existing building or specifically shape buildings to enhance the augmentation.

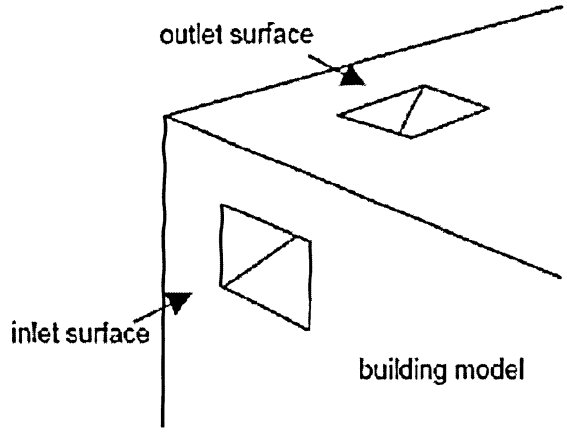


Figure 1.5: Illustration of Ducted Wind Turbines

Several projects have been explored with this idea. Research done by Campbell *et al* [4] explored the full integration of wind turbines such that it drove the architectural form. The key findings of the Wind Energy for the Built Environment (WEB project) are: the optimal geometry contains smooth, rounded, fully 3-D building forms, the best footprints are 'kidney' or 'boomerang' shapes, the shapes connecting towers or wings/infills closely fitting turbines are highly effective in preventing flow separation and loss of wind enhancements, benefits of using architecture to enhance wind turbines can be obtained for angles of incidences up to $40^o - 50^o$. Research done by Campbell *et al.* [4] suggests the integration of wind turbines could provide at least 20% to 100% of the annual electricity demand of the building (i.e. lighting, computers, and other equipment). Furthermore, the WEB project conducted experimental testing on a two-story prototype. The results showed:

1. An increase of velocity 1 $m/s$ with wind speeds of $2 - 3$ $m/s$

2. An enhanced power production for angles of incidences up to $75^o$

3. The infills surrounding the turbines further increased the power production

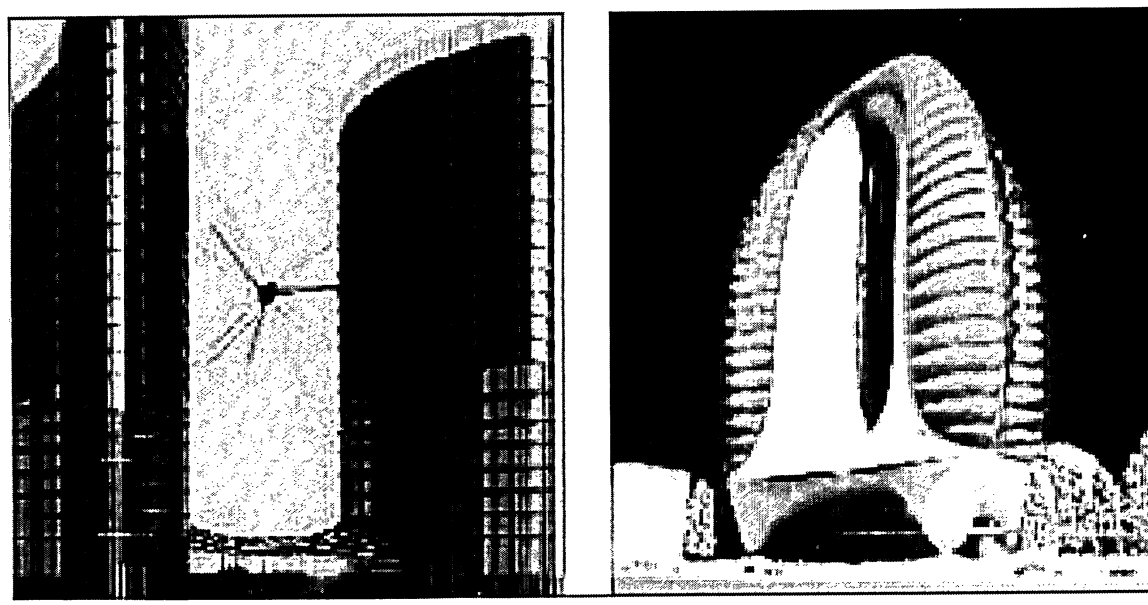

Figure 1.6: Illustration of Architecturally Augmented Wind Turbines: Horizontal Wind Turbine Type (Left) Vertical Wind Turbine Type (Right) [16]

Campbell *et al* [4] also indicated a variety of important points about the architectural, structural and environmental integration. First, the depth of floor plans might hinder natural lighting and ventilation, making the building less energy efficient. Second, the space adjacent to the wind turbines will be less appealing aesthetically and acoustically. However, these areas could be used for lifts, stairs, cores and other service areas. Third, due to the induced vibrations caused by the wind turbines rotation the building structure will have to be stiffened to compensate for the added loads.

Mertens [16] describes some of the specific technology and design issues in the use of wind turbines in Building Augmented Wind Turbines (BAWT). There are three different situations that can be used in a BAWT: between diffuser shaped buildings; on top of or along side a building or in a duct through a building.

Mertens suggests when using diffuser shaped buildings, like the situation shown in the left portion of Figure 1.6, the wind turbine can only be 20% of the characteristic length of the building. For example, if a round building is $100m$ in diameter, the wind turbine can

only be $20m$ in diameter. On the other hand, the wind turbine has to be as big as possible in order to generate an appreciable amount of energy. He further discusses what types of wind turbines would be most suitable. Martens suggests using a normal Darrieus vertical axis wind turbine which operates independent of wind direction and has relatively decent fatiguing properties [20]. However, if a horizontal axis wind turbine is used, a Well's rotor is most appropriate since it can operate in winds from two opposite directions without pitching, given its symmetric airfoil shape. The analysis of building geometry falls under multi-element bluff body flow. The pressure fields in multi-element bluff body flow are highly dependent on the building arrangement, due to the high dependence on the vortex shedding patterns behind these buildings.

### 1.1.6 Flow Between a Pair of Cylinders

Vortex shedding is the result of the unsteady flow behind single or multiple bluff bodies. Bluff bodies have been studied extensively in engineering. Flow over a single cylinder is of great importance to understanding vortex dynamics and vortex shedding structures. However, in this study the analysis consists of two bluff bodies. Investigation into the flow between a pair of circular cylinders has been studied by Bearman and Wadcock [18], Kim and Durbin [19]. Their results showed the wake behind a pair of cylinders becomes unsteady and an asymmetric wake pattern develops, which alternates from one side to another in a random manner. This random phenomena occurs under two criteria: when the gap ratio $g/d < 1$ (where $g$ is the gap size between the cylinders and $d$ the diameter of the cylinder), when the Reynolds number is above $2 \times 10^3$. The random wake affects the entire flow field and surface pressure distributions, lift, drag and mass flow between the bluff bodies.

## 1.2 Statement of Purpose

1. Determine the addition of power per unit area that can be achieved using augmentors over standard HAWT. By drawing a larger area of wind into a smaller region, the wind increases in energy (Venturi Effect) and thus the power that can be extracted is greater.

2. Determine a range of incidence angles that can be achieved to still produce power.

3. Determine how low the wind velocity can be to still allow a turbine to produce power given a 15 km/hr bottom limit for a standard wind turbine [21].

4. Find what gains there are due to 3D effects.

5. Determine an optimal configuration.

# Chapter 2

# Governing Equations

## 2.1 Incompressible Flows

A flow is said to be incompressible if the density of the flow does not change during its motion, and it is standard practice to assume below Mach 0.3 the flow density remains constant. The flow of air over urban structures is invariably below Mach 0.3 leading to the assumption of incompressible flow.

The Navier-Stokes equations for incompressible unsteady flow are solved using finite volume computational methods in order to analyze the various building geometries. The incompressible continuity equation is,

$$\frac{\partial u_i}{\partial x_i} = 0 \tag{2.1}$$

the momentum equation,

$$\frac{\partial u_i}{\partial t} + u_j \frac{\partial u_i}{\partial x_j} + \frac{1}{\rho}\frac{\partial p}{\partial x_i} = \nu \frac{\partial^2 u_i}{\partial x_j^2} \tag{2.2}$$

and the energy equation,

$$\rho\frac{\partial e}{\partial t}+\rho u_j\frac{\partial e}{\partial x_j}=-p\frac{\partial u_j}{\partial x_j}+\frac{\partial}{\partial x_j}\left(k\frac{\partial T}{\partial x_j}\right)+\Phi \tag{2.3}$$

where $e$ is the internal energy per unit mass, $\Phi$ is the rate of dissipation of mechanical energy per unit mass, $\nu$ is the kinematic viscosity, $k$ is the coefficient of thermal conductivity and $T$ is the temperature.

## 2.2 Unsteady Flow

Vortex shedding in the wake of urban structures necessitates the use of unsteady numerical models. Vortex shedding occurs when the boundary layer separates from a surface and forms a free shear layer which is highly unstable. This shear layer will eventually roll into a discrete vortex and detach from the surface, which is called vortex shedding. In flow past a cylinder, another type of, but similar type of flow instability occurs, called Von Karman vortex street. This vortex pattern occurs in the wake as a result of alternating vortices shed on both top and bottom surfaces alternatively at a discrete frequency which is a function of Reynolds number. The vortex shedding evident in bluff body simulations leads to the non-dimensional parameter called the Strouhal number describing oscillating flow, shown in equation 2.4.

$$Sr=\frac{f_r L}{V} \tag{2.4}$$

where $f_r$ is the frequency of vortex shedding, L is the characteristic length and V is the velocity of the fluid. Based on single cylinder experiments, a Strouhal number of 0.21, valid for flow over a cylinder at $Re > 1000$, is provided by White [22], using $L = 20\ m$ and $V = 4.16\ m/s$ gives a period of $30s$ per shedding cycle. Thus simulations were conducted using a $0.1s$ time step, two orders less than the shedding period, in order to accurately

model the vortex shedding that occur with the presence of two element simulations.

## 2.3 Turbulent Flow

Modelling turbulence is important for high Reynolds numbers flow in order to model the effects of turbulence in boundary layers. The existence of turbulence is dependent on Reynolds number. For example, for flow over a flat plat, turbulence will start to set in at $Re_x = 91000$ and full turbulence will occur at $Re_x = 10^6$ [23]. Full turbulence is characterized by seemingly random fluctuations in all relevant flow field variables ($u$, $v$, $T$, $\rho$, $P$, *species concentration*). The rapid mixing of components caused by turbulence effects heat transfer, momentum and mass flux.

### 2.3.1 The Reynolds Averaged Navier Stokes Equations

The large size of many structures implies that the adjacent flow field will be characterized by a high Reynolds number. Therefore, turbulent flow will result and the appropriate governing equations are the Reynolds Averaged Navier-Stokes equations (RANS), which include the added turbulence terms. In the Reynolds approach, turbulence is characterized as a sum of a mean velocity ($\bar{(u)}$) plus a fluctuating component:

$$u = \bar{u} + u' \tag{2.5}$$

Likewise for pressure and temperature,

$$p = \bar{p} + p' \tag{2.6}$$

$$T = \bar{T} + T' \tag{2.7}$$

where $\bar{u}$ and $u'$ are the mean and fluctuating components, respectively. By substituting the mean and fluctuating components of the dependent variables into the Navier-Stokes equations and taking the time average, the RANS equations (Reynolds average Navier-Stokes) are obtained. Furthermore, it can be shown that turbulence stress and heat transfer are a function of the fluctuating component and mean component of the velocity. See Appendix A.1.1 for averaging definitions.

### Continuity Equation

The continuity equation is unaffected by the fluctuating components since no nonlinear terms are present. The continuity equation for incompressible turbulent flow in tensor notation is,

$$\frac{\partial(u_i)}{\partial x_i} = 0 \tag{2.8}$$

For a full derivation of the continuity equation, consult Appendix A.1.2.

### Momentum Equations

The added turbulent terms evolved from the nonlinear terms (convective terms) after adding fluctuating components into the momentum equations. After time averaging, the remaining terms left in the momentum equation have a similar form to the continuity equation (linear terms) which results in no added turbulence terms. The time averaged momentum equation is given in Equation 2.9.

$$\rho\frac{\partial u_j}{\partial t} + \rho u_i\frac{\partial u_j}{\partial x_i} = -\frac{\partial p}{\partial x_j} + \frac{\partial}{\partial x_i}\left[\mu\left(\frac{\partial u_i}{\partial x_j} + \frac{\partial u_j}{\partial x_i}\right)\right] + \frac{\partial(-\rho\overline{u_j'u_i'})}{\partial x_i} \tag{2.9}$$

Note that all the terms except the last one are time averaged mean terms, thus the nomenclature has omitted the "bar". The molecular stresses are:

$$\tau_{ij} = \mu \left( \frac{\partial u_i}{\partial x_j} + \frac{\partial u_j}{\partial x_i} \right) \tag{2.10}$$

The added terms at the end of Equation 2.9 are the turbulence stress terms which are approximated using turbulence models. See Appendix A.1.3 for full derivation.

## 2.4 Finite Volume Method

To analyze the flow domain around architectural structures, the commercial computational fluid dynamic (CFD) software FLUENT was used. FLUENT utilizes a finite volume method to model fluid dynamic problems. The finite volume method descritizes the flow domain into control volumes to convert the governing equations to algebraic equations. The technique begins with the integration of the governing equations about each control volume which describes the conservation of quantities such as momentum, mass and energy. For illustration purposes, a steady state integral form of the general conservation equation will be used.

$$\iint_A \rho\phi\vec{v} \cdot d\vec{A} = \iint_A \Gamma_\phi \nabla\phi \cdot d\vec{A} + \iiint_\forall S_\phi d\forall \tag{2.11}$$

Where $\phi$ is any conserved variable, $S_\phi$ is the appropriate source term, $\Gamma_\phi$ is the diffusion parameter, $A$ is the surface area and $\forall$ is the volume of the specific control volume. Equation 2.11 is applied to each control volume in the flow domain. For illustration purposes, a steady-state problem will be assumed. Using Gauss's theorem, the integral

equation 2.11 can be discretized to:

$$\sum_{f}^{N_{faces}} \rho_f \vec{v_f} \phi_f \cdot \vec{A_f} = \sum_{f}^{N_{faces}} \Gamma_\phi (\nabla \phi)_n \cdot \vec{A_f} + S_\phi \forall \tag{2.12}$$

where $N_{faces}$ is the number of faces enclosing a cell, $\phi_f$ is the value of $\phi$ convected through face $f$, $\rho_f \vec{v_f} \cdot \vec{A_f}$ is the mass flux through the face, $\vec{A_f}$ area of the face $f$, $(\nabla \phi)_n$ is the magnitude of $\nabla \phi$ normal to face $f$. By default, FLUENT stores discrete values of the scalar $\phi$ at the cell centers shown in Figure 2.1.

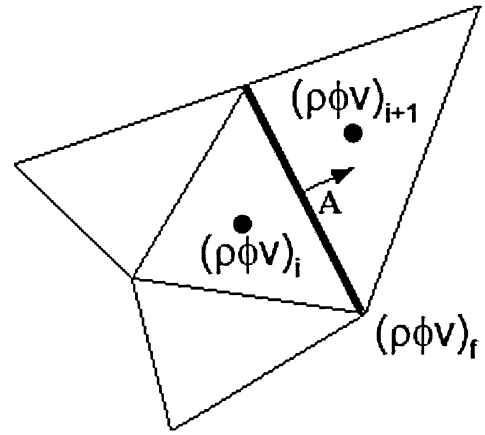


Figure 2.1: Control Volume Used to Illustrate Discretization of a Scalar Transport Equation

The face values of $\phi_f$ are required for the convection terms in Equation 2.12 and must be interpolated from the cell center values. This is achieved using an upwind scheme. Upwinding means the face value of $\phi_f$ is derived from quantities in the cell upstream or "upwind", as defined by the local characteristic directions. A second order upwinding scheme was chosen for momentum, energy and modified turbulent viscosity. By default the diffusion terms in Equation 2.12 are central difference and are second-order accurate on smooth computational grids.

### 2.4.1 Second Order Upwind Schemes

For second order accurate schemes the quantities at the cell faces are computed using a multidimensional linear reconstruction approach [24]. Using a Taylor series expansion of the cell centered solution, a higher order accuracy is achieved and the face value of $\phi_f$ is computed using the following expression,

$$\phi_f = \phi + \nabla\phi \cdot \nabla\Delta s \tag{2.13}$$

where $\phi$ and $\nabla\phi$ are the cell-centered value and its gradient in the upstream cell, respectively and $\nabla\Delta s$ is the displacement vector from the upstream cell centroid to the face centroid. The gradient $\nabla\phi$ in each cell is computed using the divergence theorem in discrete form which is given as,

$$\nabla\phi = \frac{1}{\forall}\sum_{f}^{N_{faces}} \bar{\phi}_f \vec{A} \tag{2.14}$$

where $\bar{\phi}_f$ is the average of two adjacent cells to the face in question

## 2.5 Turbulence Modeling and The Closure Problem

It has been shown that fluctuating properties of turbulent flow give rise to effective turbulent shear stresses. Then, by analogy to their molecular counter parts, these quantities can be expressed in terms of an eddy viscosity $\nu_t$ to be able to obtain some measurable quantity through experiment. It is because of these extra terms the "closure problem" arises. There are too many variables and not enough equations. Hence, turbulence models have to allow the development of the eddy viscosity in the relation to the mean flow. The primary goal of many turbulence models is to find some prescription for the eddy viscosity to model the Reynolds stresses. These may range from relatively simple algebraic models

like the Prandtl mixing length, to the more complex models such as the Reynolds stress models which solve an additional equation for each independent Reynolds stress.

### 2.5.1 Spalart-Allmaras Model

The Spalart-Allmaras turbulence model is a simple one equation model that solves a transport equation for kinematic eddy viscosity, outlined by Spalart and Allmaras [25]. This model was developed for wall bounded flows and has shown good results for adverse pressure gradients problems such as airfoils at high angles of attack. In FLUENT, the Spalart-Allmaras turbulent model has two approximations implemented for viscous-affected regions. The first is when the mesh is resolved enough that the viscous sub-layer will be fully modeled as described by the original Spalart-Allmaras formulation. The second uses a wall function when the mesh is too coarse near the wall, or, in other words, when few nodes are placed adjacent to the wall, an approximation of the viscous sub-layer is invoked.

The turbulent eddy viscosity $\mu_t$ is computed from,

$$\mu_t = \rho\tilde{\nu} f_{v1} \tag{2.15}$$

were, $\tilde{\nu}$ is the transported variable and is identical to the turbulent viscosity expect in the near-wall region. The transport equation for $\tilde{\nu}$ is given by,

$$\frac{\partial}{\partial t}(\rho\tilde{\nu}) + \frac{\partial}{\partial x_i}(\rho\tilde{\nu}u_i) = G_\nu + \frac{1}{\sigma_{\tilde{\nu}}}\left[\frac{\partial}{\partial x_j}\left((\mu + \rho\tilde{\nu})\frac{\partial\tilde{\nu}}{\partial x_j}\right) + C_{b2}\rho\left(\frac{\partial\tilde{\nu}}{\partial x_j}\right)^2\right] - Y_\nu + S_{\tilde{\nu}} \tag{2.16}$$

where $G_\nu$ is the production of turbulent viscosity and $Y_\nu$ is the destruction of turbulent viscosity that occurs in the near-wall region due to wall blocking and viscous damping. $\sigma_{\tilde{\nu}} = 2/3$ and $C_{b2} = 0.622$ are constants and $\nu$ is the molecular kinematic viscosity. $S_{\tilde{\nu}}$ is a user-defined source term. In Equation 2.15 the viscous dampening function, $f_{v1}$ is given

by,

$$f_{v1} = \frac{\chi^3}{\chi^3 + C_{v1}^3} \tag{2.17}$$

and

$$\chi \equiv \frac{\tilde{\nu}}{\nu} \tag{2.18}$$

The turbulent production term is given as,

$$G_\nu = C_{b1}\rho\tilde{S}\tilde{\nu} \tag{2.19}$$

The turbulent destruction term is given by,

$$Y_\nu = C_{w1}\rho f_w \left(\frac{\tilde{\nu}}{d}\right)^2 \tag{2.20}$$

For details on the Spalart-Allmaras model consult reference [25].

## 2.6 Sutherland Viscous Model

Boundary layers develop due to viscous interactions with solid surfaces. Furthermore, viscosity is a strong function of temperature but only a weak function of pressure. The Sutherland viscous model is most appropriate since it accounts for the changes in temperature due to viscous heating. The simulations used Sutherland's viscosity model (1893) which is based on kinetic theory using idealized intermolecular-force potential (molecules have strong repulsive forces at short distances). The model relates temperature and viscosity as,

$$\mu = \mu_0 \left(\frac{T}{T_0}\right)^{3/2} \frac{T_0 + S}{T + S} \tag{2.21}$$

where $\mu$ is the viscosity, $T$ is the static temperature, $\mu_0$ is the reference viscosity value, $T_0$ is a reference temperature and $S$ is an effective temperature and is called the Sutherland constant which is characteristic of the gas. For air at moderate temperatures and pressures the constants are set at $\mu_o = 1.7894 \times 10^{-5}\ kg/m\ s$, $T_0 = 273.11\ K$, and $S = 110.56$ K by Sutherland [26].

## 2.7 Segregated Solvers

The segregated and coupled approaches to solving the discretized equations differ in the way the equation coupling is addressed. Segregated solvers compute solutions for each equation independently over the entire domain, whereas couple solvers compute all equations simultaneously using a block implicit procedure. Initially, the study assumed a coupled solution method because it was unknown if the problem was strongly coupled or not. After several solutions were conducted using a compressible solver (ideal gas law), it was noticed that the density field of the fluid remain relatively unchanged, shown in Figure 2.2. The plot shows the density varied between 1.176208 $kg/m^3$ and 1.176991 $kg/m^3$, which is less than 0.07% difference. Thus, the solution was not coupled heavily and the more computationally efficient segregated method was used.

To use an implicit solver, the non-linear system of equations needs to be linearized. The segregated (and coupled) solution method linearize the equations implicitly with respect to those equations dependent variables using Newton's method. For instance, the x-momentum equation is linearized to produce a system of equations in which the $u$ velocity is the unknown. A point implicit (Gauss-Seidel) linear equation solver is used along with an algebraic multigrid (AMG) method to solve the resultant algebraic system of equations for the dependent variable ($u$ in this example).

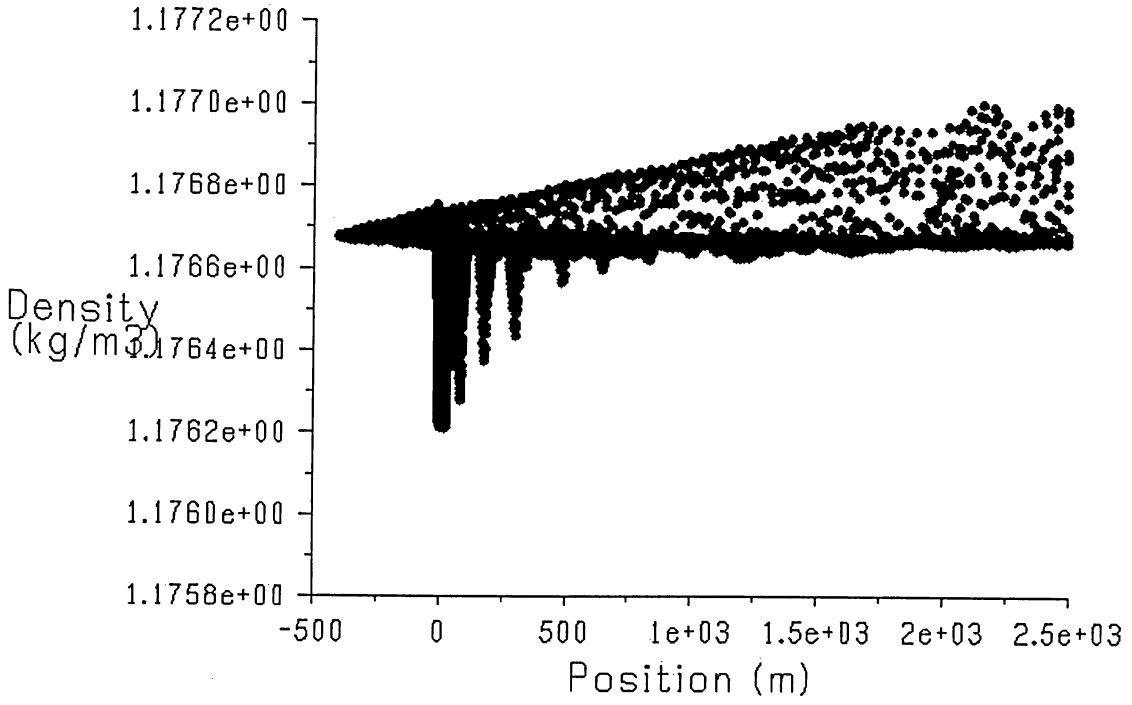


Figure 2.2: Density Plot using ideal gas law, position in the x-direction (max. density=1.176208 $kg/m^3$, min. density=1.176991 $kg/m^3$, $b_x/D_o = 20/20$, $g/D_o = 3/20$, $a/D_o = 15/20$ see Figure 5.1

## 2.8 Boundary Conditions

### 2.8.1 Velocity Inlet at Far-Field

A velocity-inlet type boundary condition was chosen since the flow conditions are considered incompressible because the flow is well below Mach 0.3. The velocity-inlet condition was used for both inlet and exit flows, shown in Figure 2.3 as $a - b$, $b - d$ and $d - f$ (identical for lower bounds under symmetry line $a - f$). This type of boundary condition allows the total (or stagnation) properties of the flow to float such that they will rise to whatever value necessary to solve for the velocity distribution. Thus, it was necessary to specify a reference pressure of 0 Pascals at the far-field ($-400m$, $400m$) to set the gauge pressure such that all cases were compared based on the same pressure datum. FLUENT's

treatment of the velocity inlet condition uses velocity components defined by the user at the boundary to compute inlet mass flow rate, momentum fluxes, and fluxes of energy. The mass flow rate entering a fluid cell adjacent to a velocity inlet boundary is computed as shown in Equation 2.22.

$$\dot{m} = \int \rho \vec{v} \cdot d\vec{A} \tag{2.22}$$

Note the density is considered to be constant throughout the domain including the far-field boundary.

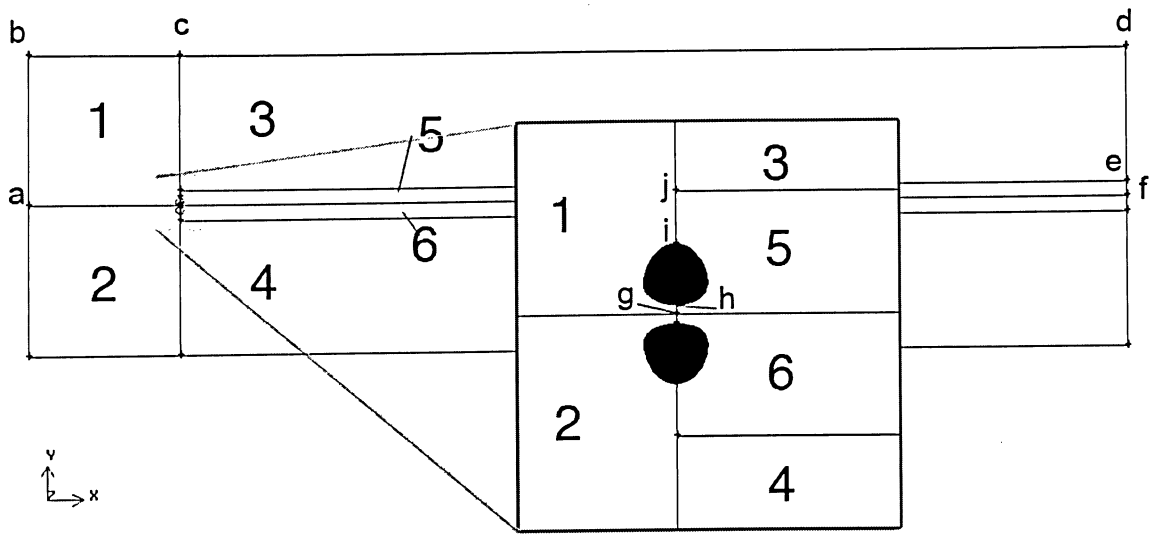


Figure 2.3: Close-Up of schematic around geometry (Numbers represent interior sections in the domain)

### Treatment of Velocity Inlet Condition at Flow Exits

Using a segregated solver in combination with the velocity-inlet condition, the flow exit condition is calculated by using the boundary condition value for the velocity component normal to the exit flow area. It does not use any other boundary conditions that have been input by the user. All flow conditions, except the normal velocity components, are

assumed to be those of the upstream cell. This is a valid boundary type as long as the boundaries are located a minimum of 20 chord lengths from the geometry.

### 2.8.2 Wall Boundary Condition

The wall boundary condition is used for solid wall boundary interaction with fluid regions. The viscous flow problem at hand requires a no-slip boundary condition, and shear stresses are calculated based on the local flow field. The no-slip condition implies the velocity of the fluid at the wall is zero with an increasing velocity gradient normal to the wall defining the boundary layer. A sufficient amount of nodes need to be placed adjacent to the wall in order to capture the boundary layer which is dictated by the y-plus function given in Equation 3.3 in subsequent sections.

### 2.8.3 Porous Media Condition

A porous media boundary condition was implemented in between the buildings to simulate the momentum loss due to the wind turbines. The porous medium is used just to simulate the back pressure and does not account for wake or tip effects caused by the wind turbine. In the Navier-Stokes equations, a porous media is modeled by the addition of momentum source term. The source terms are comprised of two terms: one for the viscous loss or the Darcy term and a second inertial loss term. The inertial loss term is a momentum sink, which causes a pressure gradient over the porous cell which is proportional to the fluid velocity squared. In a simple homogenous porous medium the added source term is given in equation 2.23.

$$\nabla P = -\left(\frac{\mu}{\alpha} + C_2 \frac{1}{2} \rho \nu_{mag} \nu_i\right) \Delta n_i \tag{2.23}$$

where $\mu$ is the viscosity of the fluid, $\alpha$ is the permeability (associated with the Darcy loss), $\rho$ is the fluid density, $v_{mag}$ is the magnitude of velocity, $v_i$ is the velocity for the $i^{th}$ momentum equation and $\Delta n_i$ is the thickness of the porous medium in the respective direction and $C_2$ is the inertial losses or pressure loss coefficient. The study assumed pressure loss was only experienced normal to the wind turbine sweeping area and thus the equation reduces to a one dimensional approximation. Furthermore, it was also assumed no viscous losses were experienced due to the presence of the wind turbine, leaving only a pressure loss. The pressure loss was assumed to be a modest 40%, meaning 40% of the wind energy was being extracted by the wind turbine. Therefore, the pressure loss coefficient was assumed to be a $C_2 = 0.4$ with a corresponding thickness set to $\Delta n_i = 1\ m$. An example of the pressure drop across the gap region, a plot of gage pressure along the x-axis through the gap region is shown in Figure 2.4. The figure shows the contrast between the porous media condition and without the porous media condition, using the case $b_x/D_o = 20/20$, $a/D_o = 15/20$, $g/D_o = 3/20$ at $0^o$ angle of incidence. The pressure drop is based on the local velocity in the cells just before the porous media which was found to be $V_2 = 5.555\ m/s$. Based on Equation 2.23 the pressure drop, shown in Figure 2.4, is,

$$\Delta P_x = -\left(C_2 \frac{1}{2} \rho \nu_{mag} \nu_i\right) \Delta n_i = -\left(0.4 \frac{1}{2} (1.225)(5.555)^2\right)(1) = -7.56\ Pa$$

which is verified by taking the difference in cell values which was computed to be $\Delta P_x = -7.52\ Pa$

## 2.9 Power Ratio

To determine the effectiveness of the augmentors at capturing large volumes of wind driven mass flow, a power ratio variable was developed. The power ratio is based on the energy

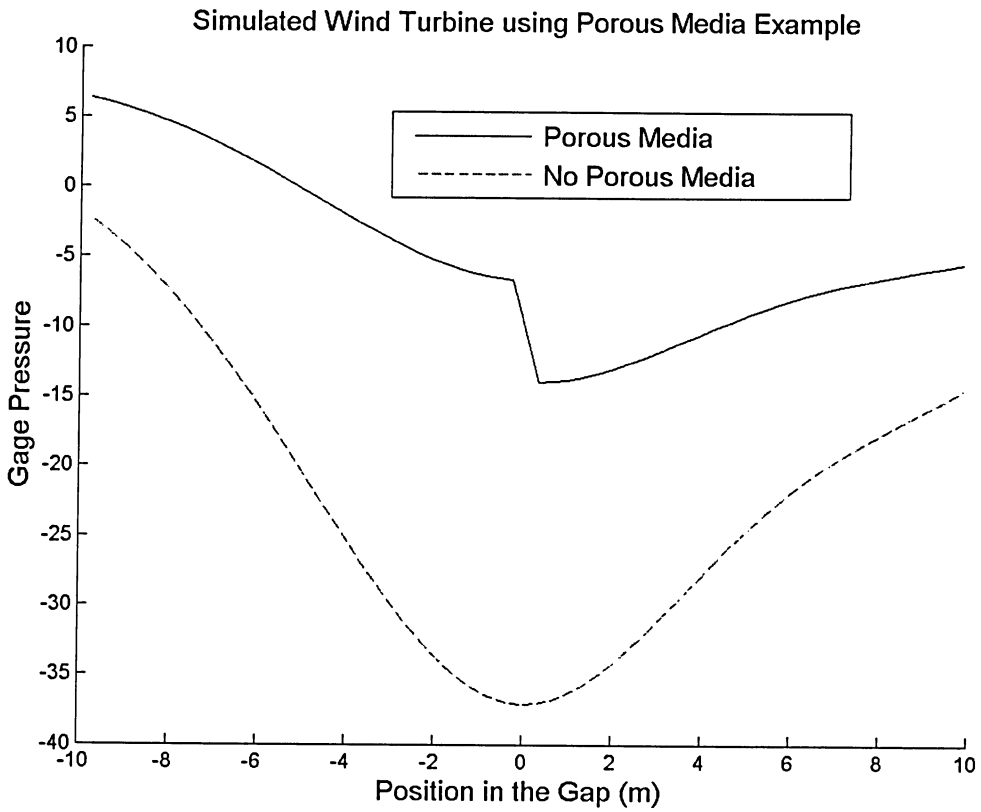


Figure 2.4: Example Porous Media Condition using $b_x/D_o = 20/20$, $a/D_o = 15/20$, $g/D_o = 3/20$ at $0^o$ angle of incidence

density of the wind upstream in the undisturbed flow relative to the gap region between the augmentors. The rate of energy passing through a given area $A$ is defined as,

$$\frac{dE}{dt} = \iint_A e\rho(V \cdot n)dA \tag{2.24}$$

where $e$ is the energy per unit mass,

$$e = u + \frac{1}{2}V^2 + gz \tag{2.25}$$

The hydrostatic term $gz$ is negligible and the internal energy $u$ remains relatively constant due to a lack of heat transfer and compressibility,

$$e = \frac{1}{2}V^2 \tag{2.26}$$

Therefore the energy rate or flux becomes,

$$\dot{E} = \frac{dE}{dt} = \frac{1}{2}\rho \iint_A V^2(V \cdot n)dA \tag{2.27}$$

where $\rho$ is taken out of the integral because it is considered constant. This is then averaged per unit length squared by diving by the area $A$.

$$\frac{\dot{E}}{A} = \frac{1}{2A}\rho \iint_A V^2(V \cdot n)dA \tag{2.28}$$

Equation 2.28 is effectively the power density. The power ratio is defined by normalizing the power density at the gap region (station 2) with the power density at the pressure far-field (station 1) shown in Figure 2.5.

$$PR = \frac{\frac{\dot{E}_2}{A_2}}{\frac{\dot{E}_1}{A_1}} = \frac{\frac{1}{2A_2}\rho \iint_{A_2} V_2^2(V_2 \cdot n)dA_2}{\frac{1}{2A_1}\rho \iint_{A_1} V_1^2(V_1 \cdot n)dA_1} \tag{2.29}$$

However, since the velocity at the far-field is a constant based on static far-field conditions Equation 2.29 becomes,

$$PR = \frac{\frac{1}{2A_2} \iint_{A_2} V_2^2(V_2 \cdot n)dA_2}{\frac{1}{2}V_1^3} \tag{2.30}$$

The integral in the gap region is performed by using all the cell values, $V_2$ in the gap region. Note from the relationship between power and velocity; if the velocity is doubled the power is increased eight fold.

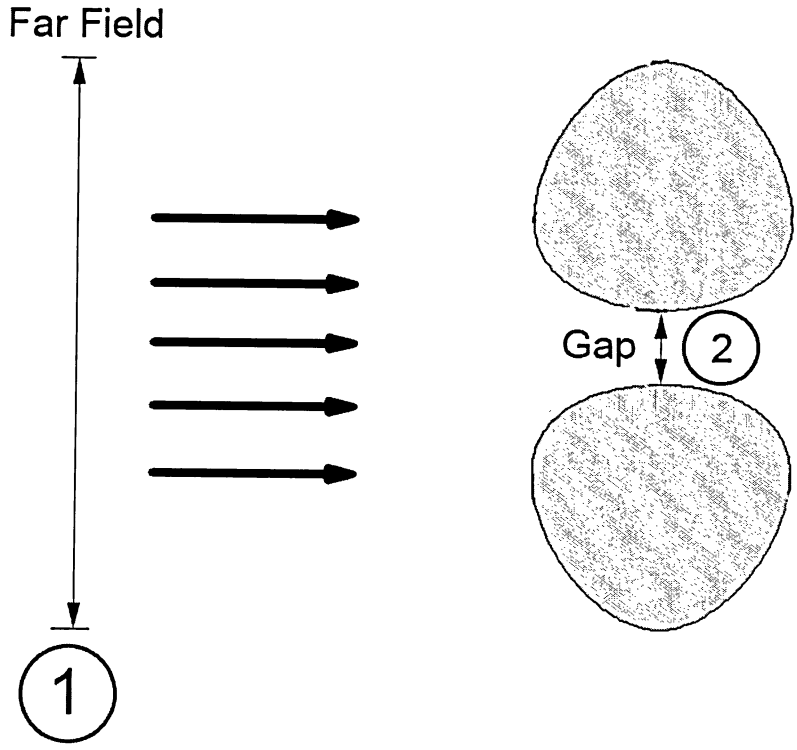


Figure 2.5: Schematic for Power Ratio Derivation

## 2.10 Project Constraints

The building dimensions were constrained in order to optimize the natural lighting effects to ensure energy efficiencies were not lost due to artificial lighting. Natural lighting is transferred via windows and skylights. As an architectural standard, keeping one dimension under $20m$ allows the building to be primarily illuminated by natural light. By exceeding $20m$, a portion of the building will have to be illuminated by artificial means not only increasing the energy demands from the building but decreasing the health and productivity of its residences.

Furthermore, to constrain the project further, the ambient flow conditions needed to be defined. For simplicity, the study assumed a steady ambient flow. However, in most urban areas this would be far from realistic since city dwellings flows are highly turbulent. Further work should be conducted with a transient ambient flow to determine how the variation in ambient flow effects the flow field and power ratio through the gap.

# Chapter 3

# Grid Development

## 3.1 2D Grid generation

In computational fluid dynamics, grids are used to descritize the flow domain allowing the discrete fluid equations to be solved for every grid interface. The program Gambit is Fluent's geometry and mesh generation software that was used to descritize the flow domains around various shapes. Initially, the study assumed a compressible, unsteady, viscous fluid which dictated the size of the domain. However, the final simulations used incompressible, unsteady, viscous flow since the flow was well below Mach 0.1. Typically the extremities of the flow domain are set between 20 chord lengths and 100 chord lengths for a pressure-far field type boundary, shown in Figure 2.3.

**Mesh 1** An entirely structured scheme was used to mesh the domain. To reduce computation time, a symmetry plane was used that bisected the gap region along the x-axis. Attempts were made to use Gambit's grid boundary layer generation function to capture boundary layer development and separation. However, grid distortion appeared after the automated grid smoothing algorithm was completed in the surface mesh generation process.

**Mesh 2** To avoid the grid distortion but still control the mesh near the wall, the geometry was enclosed with a rectangular interior boundary. Thus, the off wall spacing could be adjusted easily while also controlling the mesh density around the object, shown in Figure 3.1. These first sets of simulations solved with relative ease. However, once the angle of incidence of the wind was changed the symmetry boundary condition could no longer be used, thus the entire flow domain needed to be modeled. Furthermore, when performing a grid dependency analysis, increasing the nodes density convergence could no longer be achieved. It was also realized that the problem was not a steady solution since the residuals had a periodic nature to them. By using a transient method, the simulations revealed an unsteady phenomena called vortex shedding.

**Mesh 3** To capture the vortices, a wake region (region 5 and 6 in Figure 2.3) was created that was entirely made of a triangular unstructured mesh. By using an unstructured mesh in this region, the vortices could be fully analyzed since the unstructured mesh is uniform in all directions, shown in the bottom of Figure 3.1. After conducting the simulations using the revised meshing scheme, it was noticed that the simulations were computationally expensive and taking an unreasonable amount of time to converge. It was concluded that the mixed structured and unstructured domains complicated the information transfer between blocks in the domain.

**Mesh 4 (Final)** The final mesh used Gambit's structured boundary layer function with the remainder of the domain being generated using an unstructured triangular meshing scheme. The domain was broken into six domains shown in Figure 2.3. Two of the domains were developed directly aft of the geometry for the purpose of con-

trolling the element density in the wake region, as in Mesh 3. A large number of elements were placed in the wake region so the complex vortex shedding pattern could be modeled accurately. The progression to the unstructured meshing scheme proved beneficial for a number of reasons: modeling the complexity of the wake pattern, relative ease of modeling various geometries using identical meshing schemes, and the smooth meshing transitions from the structured boundary layer mesh to the rest of the unstructured domain. The solution scheme was then adjusted in order to save computational time since the unstructured meshes require more computational resources. The solution was adjusted by assuming an incompressible flow given the relatively low Mach number (much less than 0.1), which required a velocity inlet condition at the far-field. Furthermore, as recommend by the FLUENT users manual, a segregated solver scheme was used for unsteady-unstructured meshes and weakly coupled problems, which reduced the computational time significantly.

## 3.2 Grid Study

In any numerical simulation it is important to perform a parametric or grid study of the problem in order to assess the dependency of the solution on grid size and configuration. If a solution can be shown to be grid independent, then only the modeled physics are producing the phenomena and not the manner in which the fluid equations are solved on a particular grid. The grid effect on power ratio $PR$ (as shown in Equation 2.30) at an angle of incidence of $0^o$ are shown in Figure 3.2 and given in Table 3.1. The plot shows the $PR$ approaching asymptotically the Richardson extrapolated value of 6.05.

The domain was broken into six sections in order to control the mesh upstream of the geometry and in the wake region. The entire domain is shown in Figure 2.3 with an enlarge image around the geometry. Areas 5 and 6 were created in order to fully resolve the wake region of the geometry. Furthermore, around the geometry surface, a non-uniform

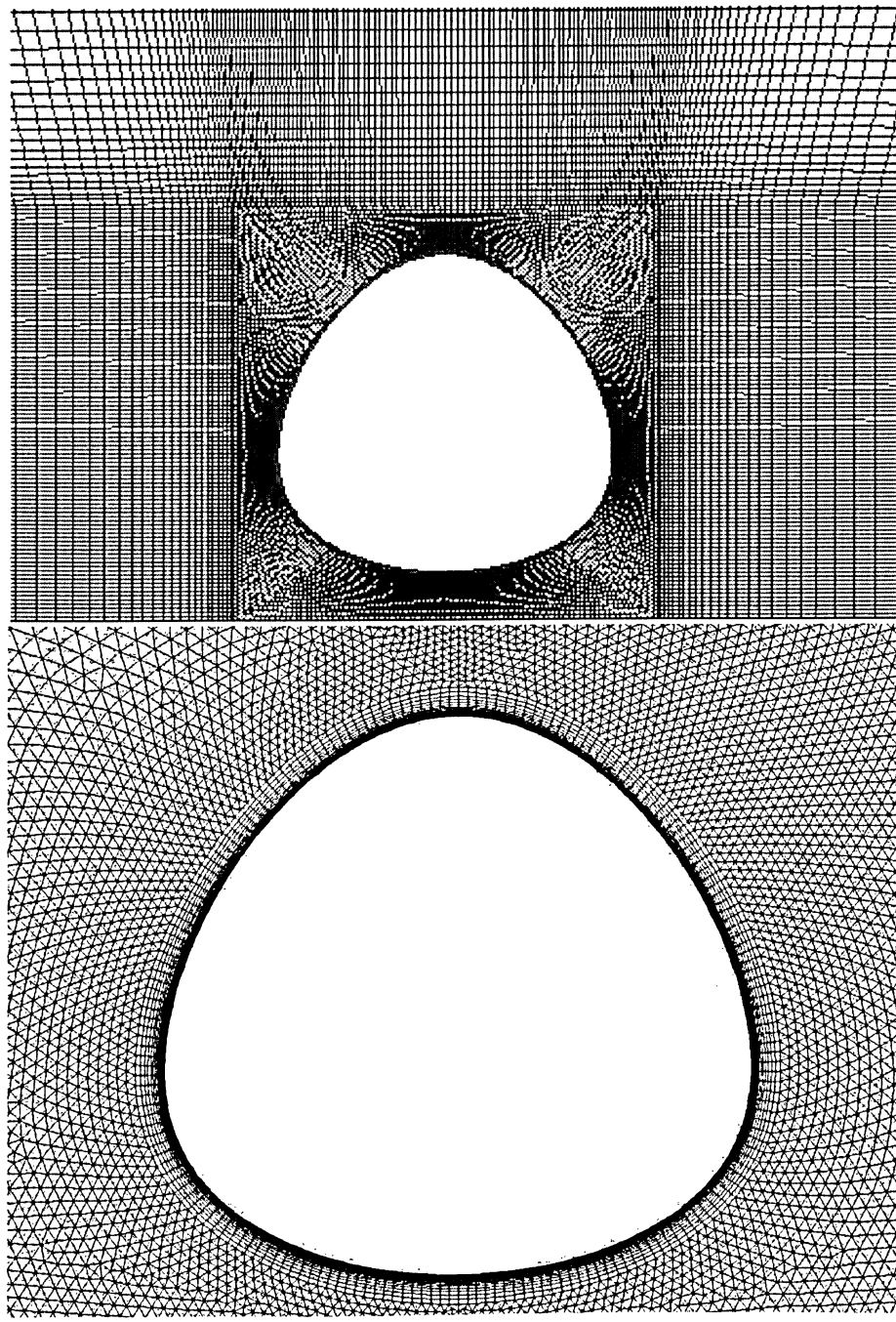

Figure 3.1: Structured Symmetric Mesh example (Top) Final Unstructured Mesh (Bottom)

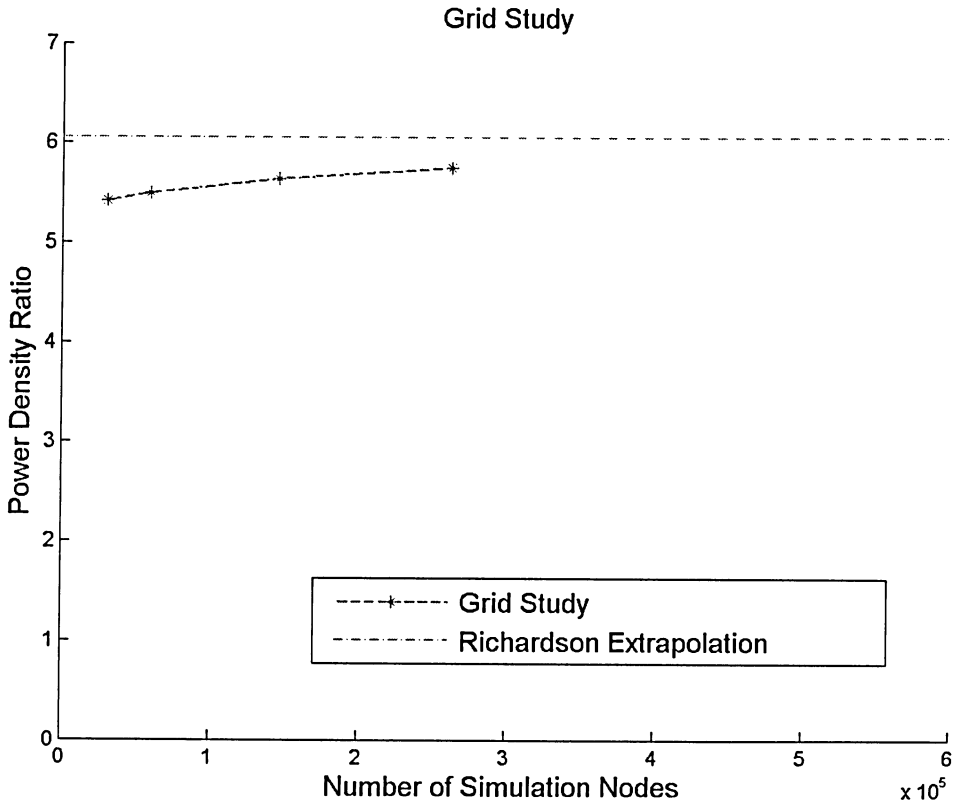


Figure 3.2: Grid Study of enclosed spline at $b_x/D_o = 40/20$, $g/D_o = 3/20$, $a/D_o = 10/20$ at $0^o$ angle of incidence

structured mesh with high node density nearest to the wall was used in order to model the boundary layer including the viscous sub-layer. As suggested by Spallart and Allmaras [25], in order to fully model the viscous sub-layer, a sufficient number of nodes needed to be placed at a very close distance adjacent to the wall. The parameter that dictates the off-Jetwall spacing of the first node is call the Y-plus function and is defined by,

$$y^+ = \frac{\rho u_T y_P}{\mu} \tag{3.1}$$

where $u_T = \sqrt{\tau_w/\rho_w}$ is the friction velocity ($\tau_w$ and $\rho_w$ is the shear stress and density at the wall, respectively), $y_P$ is the distance from point $P$ to the wall, point $P$ is the first

node above the wall, $\rho$ is the fluid density, and $\mu$ is the fluid viscosity at point $P$. In order to capture the viscous layer effectively the $y^+$ should be less than 10. A sample plot is given in Figure 3.3, showing the $y^+$ is predominately below the value of 4 on the surface of the augmentor.

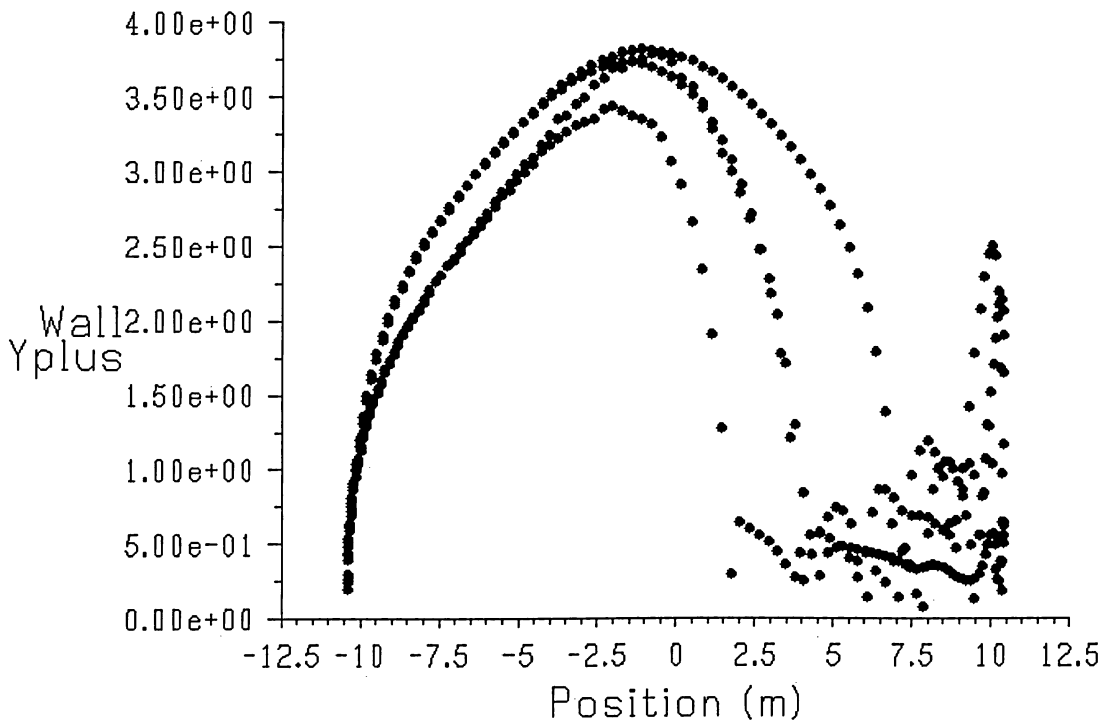


Figure 3.3: Y-plus plot for geometry surface (Case: $b_x/D_o = 40/20$, $g/D_o = 3/20$, $a/D_o = 15/20$, 59,549 nodes at $0^o$)

Table 3.1: Grid Study

| Node Density | Power Density Ratio |
|---|---|
| 30,843 | 5.42 |
| 59,549 | 5.4975 |
| 146,090 | 5.646 |
| 263,000 | 5.7522 |

The methodology behind increasing node density was to place extra nodes where the greatest changes occurring in the flow field; in the wake region and in the boundary layer.

To increase the node density around the object, the number of nodes in the structured boundary layer was increased, as well as the number of nodes on the geometry surface. The node density in the wake region was refined by increasing the nodes closes to the geometry, to obtain meshes with 30,843, 59,549, 146,090 and 263,220 nodes, respectively. The node density increased primarily on the surface of the geometry, in the wake region area 5 and 6 and just upstream of the geometry where area 1 and 2 are joined. The node density break down is provided in table 3.2 and the specific line break down of node density is provided in Table C.1 in Appendix B. The power ratio changed only 5.8 % over

Table 3.2: Node Density Break down for Grid Study by Area

| Area | Course | Medium | Fine | X-Fine |
|---|---|---|---|---|
| 1, 2 | 6294 | 11922 | 25640 | 42684 |
| 3, 4 | 1702 | 3700 | 9356 | 13035 |
| 5, 6 | 7918 | 15361 | 39187 | 77137 |

31, 000 to 263,000 nodes. The difference between 146, 000 nodes and 263,000 nodes is less than 2 % indicating the solution is not grid dependent and all meshes are adequate solutions.

## 3.3 3D Grid Development

To support the 2D results the best case at $0^o$ was chosen to to be extended to 3D. A building height of $h/D_o = 100/20$ was chosen. A schematic is shown in Figure 3.4. A structured grid was chosen given the limited computational facilities at hand. To avoid the grid distortion with the structured mesh noticed in the 2D Mesh 1 attempt, the geometry was bounded by an interior face similar to the 2D Mesh 2 attempt, shown Figure 3.5. Furthermore, by creating an internal boundary around the geometry, it was possible to more accurately control the off wall spacing of the nodes, creating a higher density near the wall where the large velocity gradients occur. The geometry was then extended to a

$100m$ in height, with the far field in the vertical direction $z$ taken to be 300 $m$. The y-plus values on the surface in the $z$ direction is shown in Figure 3.6. Note the y-plus along the walls are close to a value of 10 while the roof-top is much higher. This is not a concern since the flow is known to be separated at the roof-edge. The y-plus is less important on the roof-top since a separation occurs on the edge and does not to be calculated from the development of the boundary and its response to adverse pressure gradients.

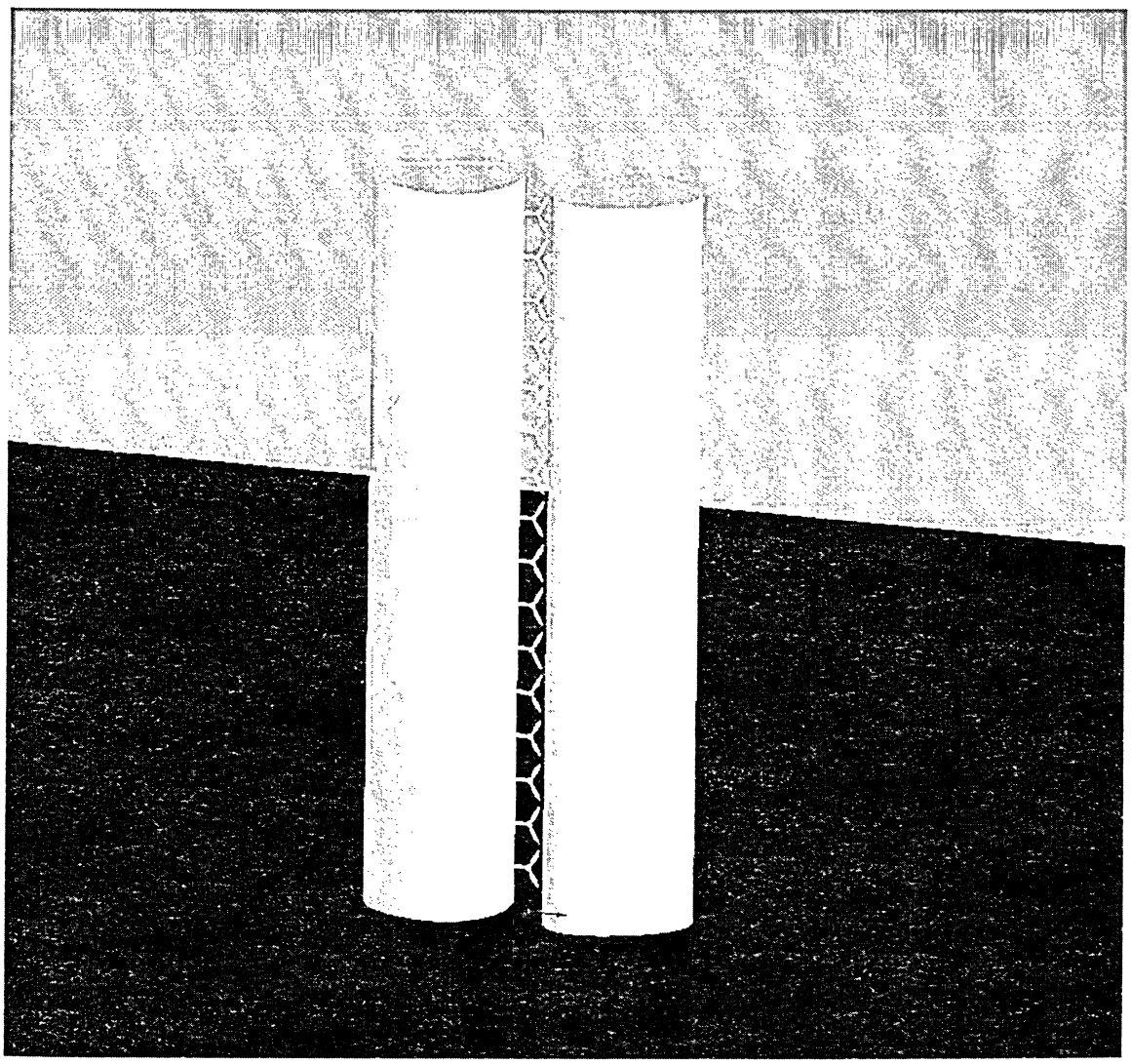

Figure 3.4: Illustration of 3D geometry $b_x/D_o = 20/20$, $g/D_o = 3/20$, $a/D_o = 15/20$, $h/D_o = 100/20$ and $D_o = 20m$

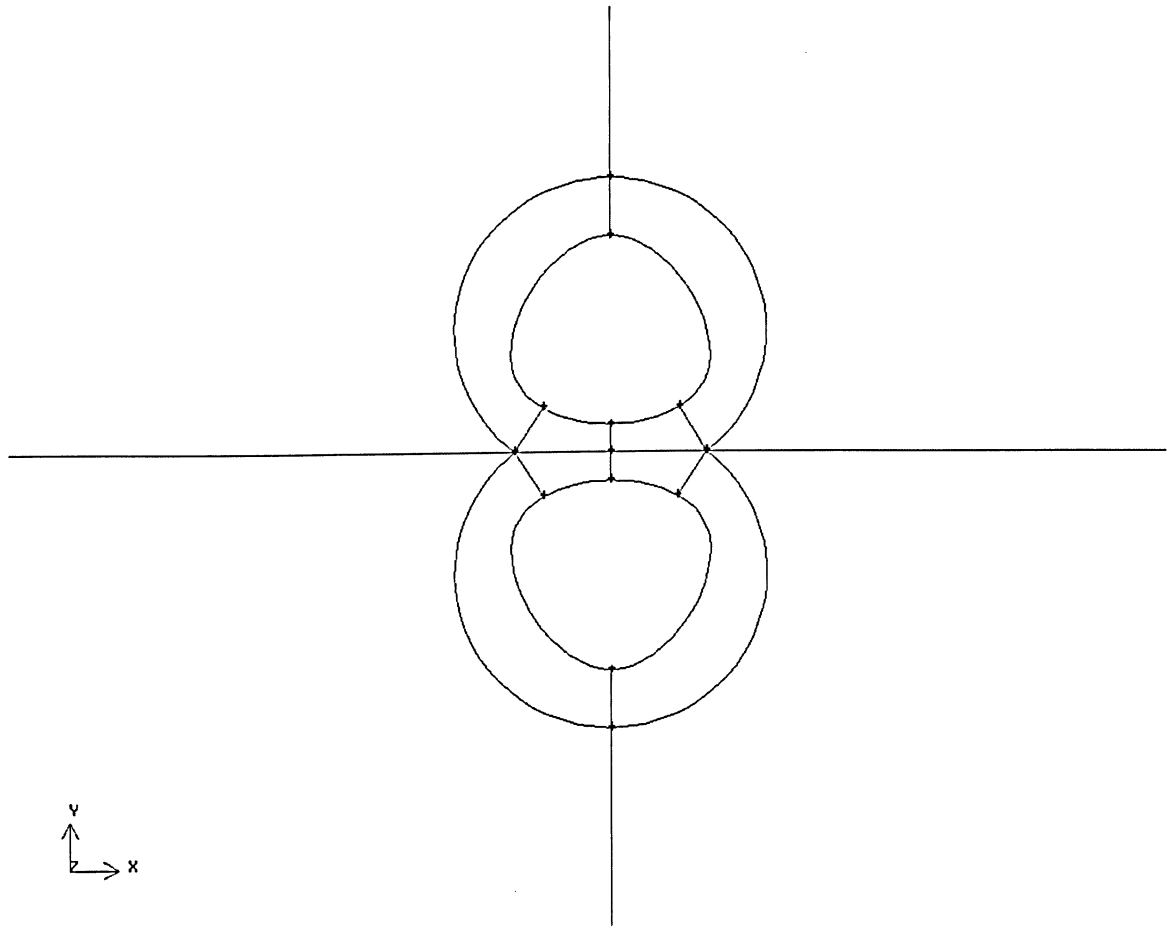


Figure 3.5: Interior boundaries for 3D grid development $b_x/D_o = 20/20$, $g/D_o = 3/20$, $a/D_o = 15/20$ and $D_o = 20m$

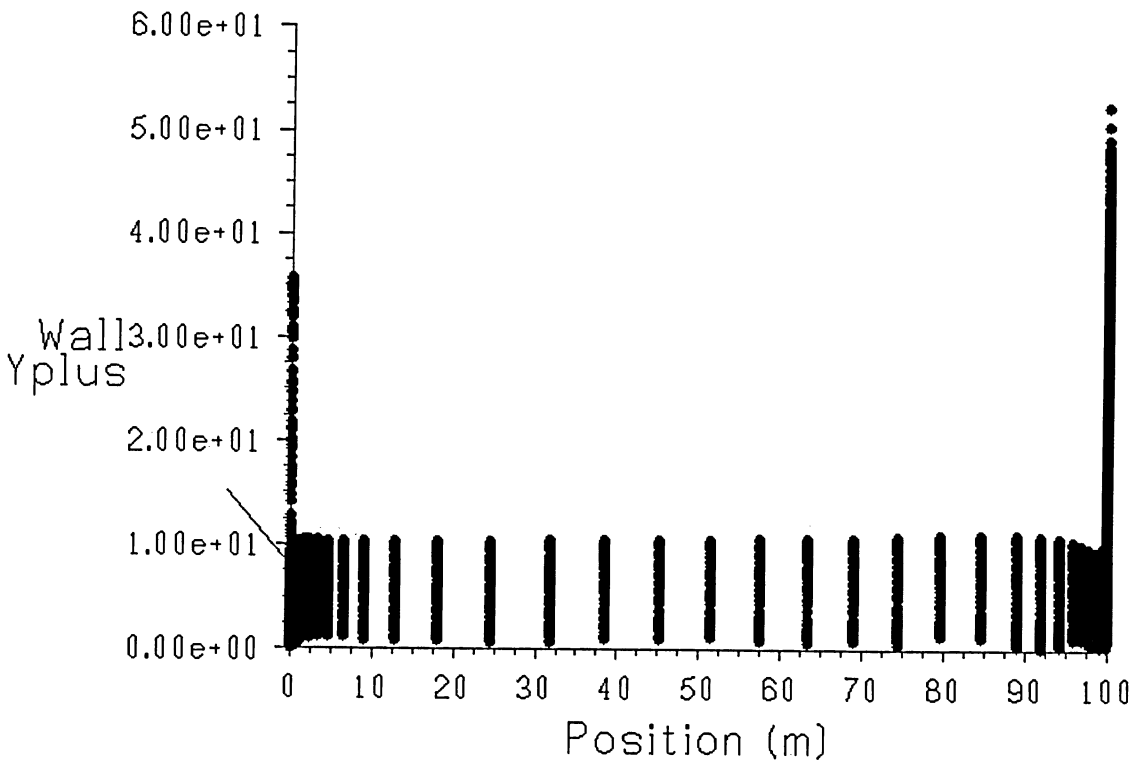


Figure 3.6: 3D y-plus position in the vertical direction using $0^o$ angle of incidence case $b_x/D_o = 20/20$, $g/D_o = 3/20$, $a/D_o = 15/20$ and $D_o = 20m$

# Chapter 4

# Time Step Study

Analogous to the grid refinement study, a time study also needed to be conducted since there are transient phenomena present in the solution. The transient behavior caused by the vortex shedding will be effected by the time marching scheme. To determine the effect of time step size on the solution, the time step sizes were reduced, and the power ratio and variance were compared, shown in Figure 4.1, and the values are presented in table 4.1. The difference between $\Delta t = 0.1s$ and $\Delta t = 0.001s$ in the power ratio is less than 5% which translates to a difference in mean velocity of 1.6% which is within numerical error as determined by the grid refinement study. Furthermore, at the throat of the augmentor where the turbine will be located, the variance of velocity is about 7.4% difference between $\Delta t = 0.1s$ and $\Delta t = 0.001s$. Given the number of simulations to optimize the geometry, it was assumed that $\Delta t = 0.1s$ was sufficient since it is the power ratio ($PR$) that determines the optimal shape where the variance of velocity is used just to determine the detrimental effects on the turbine.

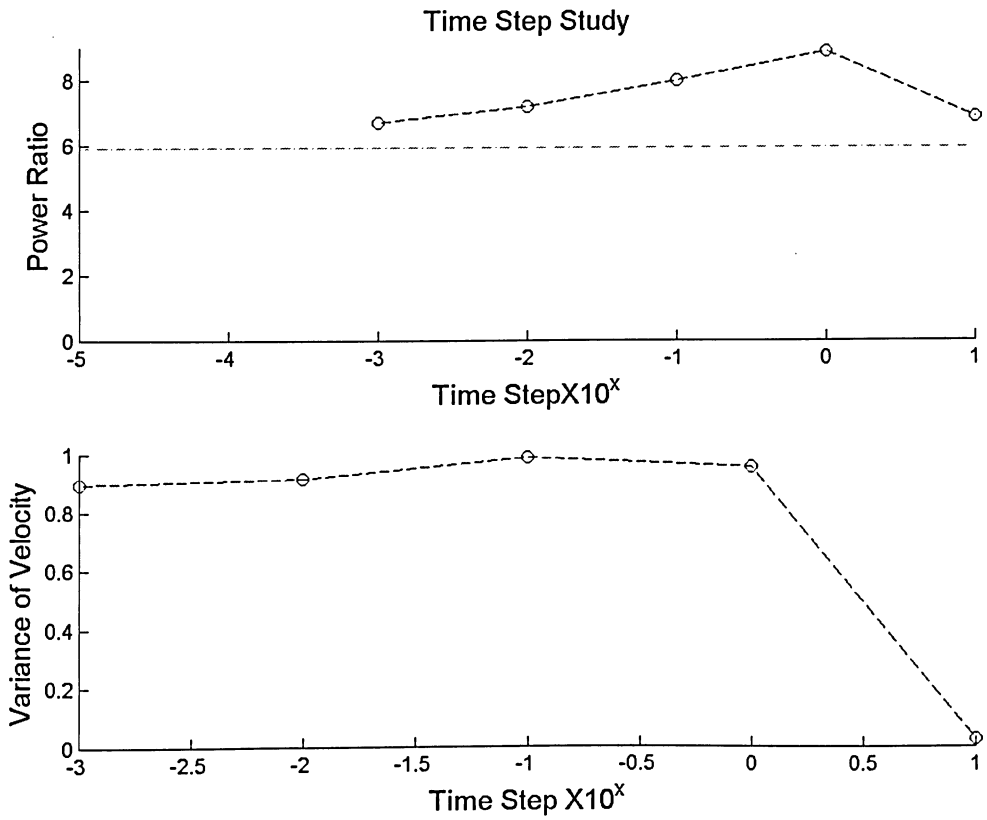


Figure 4.1: Time Step Study

## 4.1 Time Step Convergence

Given this is a transient problem, the length of time the code is run will have an influence on the mean values below a limit. Above a certain run time, the results for the mean, such as power ratio, will remain unchanged. Therefore, a time convergence study was conducted such that the mean of $PR$ was calculated from $t = 0$ to time step $t = t_i$, defined in Equation 4.1.

$$\bar{PR}_i = \frac{\sum_{t=0}^{t=t_i} PR_i}{N_i} \tag{4.1}$$

Table 4.1: Time Step Study at $0^o$ angle of incidence case: $b_x/D_o = 20/20$, $g/D_o = 3/20$, $a/D_o = 15/20$

| Time Step Size | Power Ratio | Variance of Velocity |
|---|---|---|
| 0.001 | 7.9147 | 1.0671 |
| 0.01 | 8.0215 | 0.9172 |
| 0.1 | 8.3090 | 0.9884 |
| 1 | 8.5992 | 0.9554 |
| 10 | 7.8960 | 0.0248 |

where, $N_i$ and $PR_i$ are the number of time steps and the power ratio at time $t_i$, respectively. The results of the study are shown in Figure 4.2. The Figure shows the value of velocity approaching a steady mean value.

The mean power ratio was considered converged when the percent difference was well below 0.005% which occurred at $730s$ seconds. Therefore, all simulations were run to $t = 730$ seconds shown in the bottom of Figure 4.3. This plot shows the error between successive time steps does not exceed 0.005% for several hundred time steps.

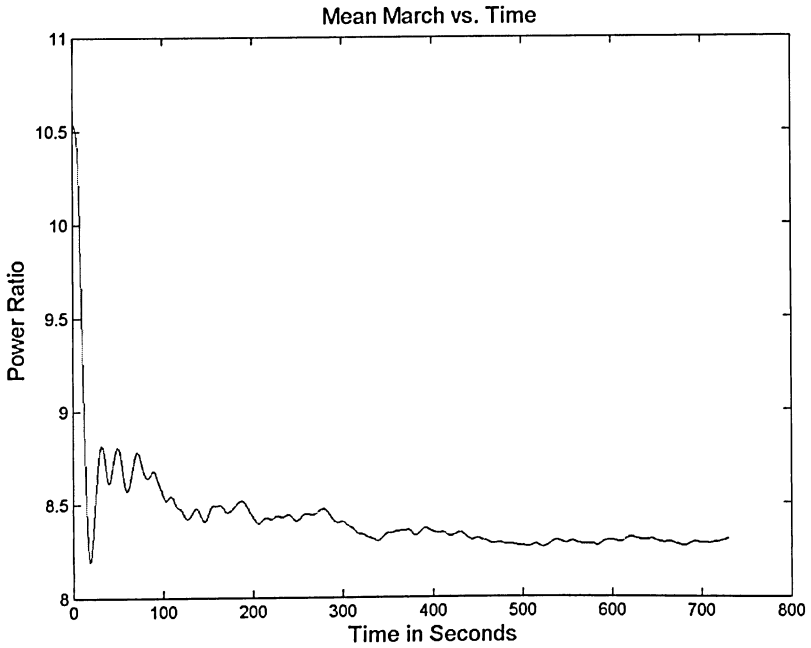


Figure 4.2: Time to steady mean study for $g/D_o = 3/20$, $b_x/D_o = 20/20$, $a/D_o = 15/20$ at angle of incidence of $0^o$

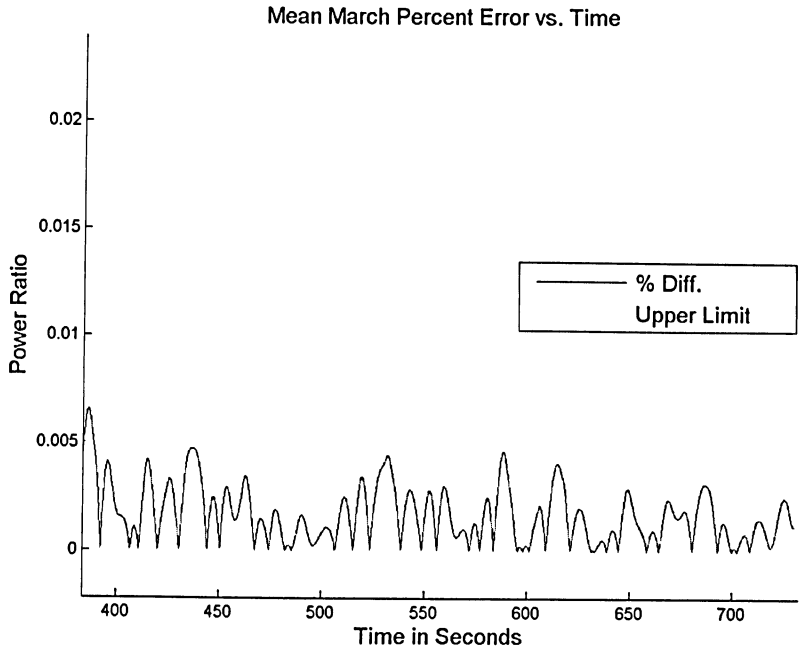


Figure 4.3: Percent Error for $g/D_o = 3/20$, $b_x/D_o = 20/20$, $a/D_o = 15/20$ at angle of incidence of $0^o$

# Chapter 5

# Results

## 5.1 Enclosed Spline Family

The study sought to find an optimal geometry in order to augment wind turbines, in addition to serving as a suitable shape for architectural uses. A relatively simple family of geometries considered were four-point enclosed splines shown schematically in Figure 5.1. The points A and C are constrained vertically and points B and D are constrained horizontally, resulting in a symmetric geometry about line B-D. Symmetry in this manner was sought so that the wind can be used in either direction. Furthermore, the spline slopes at B and D were constrained to be horizontal (slope of zero). By varying the parameters $a$, $A_1$, $g$ and $b_x$ independently, a family of geometries were created and analyzed to determine a set of trends. The parameters were normalized using the characteristic length $D_o$ which remained constant throughout the study. The parameter $b_x/D_o$ is defined as the thickness parameter. The $g/D_o$ parameter is defined as the gap parameter. The $a/D_o$ defined as the oblateness parameter. In the following sections, the effects of varying these parameters will be explored.

The baseline conditions set for the free stream conditions were set at a pressure of

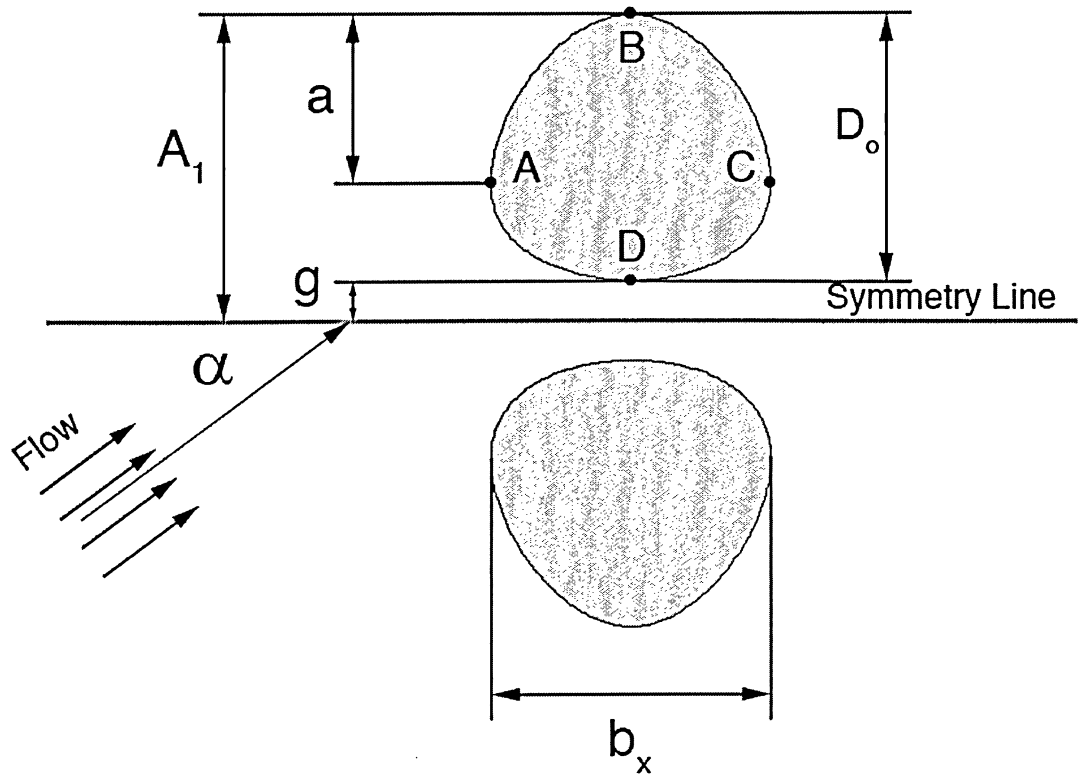


Figure 5.1: Enclosed Spline and Geometry Definitions

$P_o = 101\ 325\ Pascals$ , density at $\rho_o = 1.225\ kg/m^3$ and the temperature at $T_o = 300^o\ K$. A uniform flow of $V_o = 4.16$ m/s was used for the entire study except for the Reynolds number effects study were the velocity was increased to $V_o = 8.32,\ 12.48$ m/s.

To simulate the momentum loss of the wind turbine, a porous media boundary condition was implemented in the throat area for some cases. The idea of using porous materials to simulate the momentum loss in turbines has been used experimentally to study shrouded wind turbines. Fletcher used screens in his experiments since the model sizes didn't allow for actual wind turbines [15]. Implementing a porous media does not necessarily mimic the presence of a wind turbine but does ensure the trends found would still remain similar given an identical back pressure.

## 5.2 Two Dimensional Results

### 5.2.1 The Effects of Varying the Oblateness $a$ Parameter

This section is devoted to determining how the power ratio is effected by varying the oblateness parameter $a$ parameter, which is plotted in Figure 5.2. The simulation held the following parameters constant: the width parameter $b_x/D_o = 20/20$, the gap parameter $g/D_o = 3/20$ and $A_1 = 23$. All dimensions are in meters. No porous medium was used for the results. The free stream conditions were set to a pressure of $P_o = 101\ 325\ Pascals$ , the density of air at $\rho_o = 1.225\ kg/m^3$, temperature of $T_o = 300^o\ K$ and a uniform velocity of $V_o = 4.16\ m/s$.

Decreasing the $a$ value increased the curvature near the gap region and decreased the curvature on the outer parts of the geometry. The plot shows, for high values of $a$, the power ratio is increased for low angles of attack. However, at high angles of attack, increasing the $a$ value decreases the power ratio relative to smaller $a$ values. At low angles of attack, the increase in power ratio is associated with the increase in curvature near the

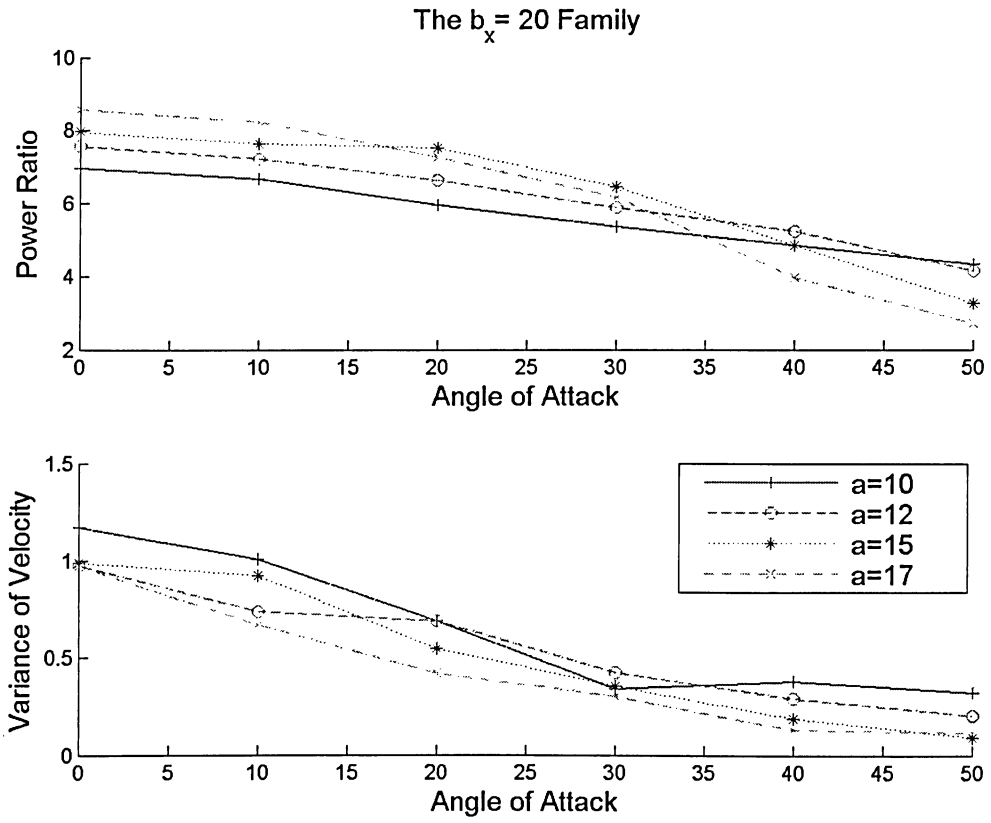


Figure 5.2: The effects of varying the $a$ parameter on power ratio and variance of velocity holding $b_x/D_o = 20/20$, $g/D_o = 3/20$ constant

gap region. Increasing the curvature increases the pressure gradient, drawing more flow into the gap region.

Figure 5.3 shows a high difference in pressure between the gap region and upstream of the geometry. In Table 5.1, area-weighted average values of static pressure at the gap region and the pressure at locations $x/D_o = -10/20$ and $y/D_o = 0/20$ are given. The decrease in power ratio at high angles of attack is associated with the high pressure

Table 5.1: Gage Pressure Values in Gap region (x=0m) and 20m upstream (x=-10m)

| bx | a | aoa | p (Pascals) at x=-10m | p (Pascals) at x=0 |
|---|---|---|---|---|
| 20 | 10 | 0 | 5.90 | -16.18 |
| 20 | 17 | 0 | -2.15 | -30.79 |
| 20 | 10 | 50 | 3.56 | -14.03 |
| 20 | 17 | 50 | -1.69 | -18.68 |

region near the inlet of the geometry, as seen in the lower image in Figure 5.4. In the $a/D_o = 17/20$ case, shown in Figure 5.4, the flow is diverted around the geometry instead of into the gap region shown Figure 5.5. In contrast to the $a/D_o = 17/20$ case, the $a/D_o = 10/20$ case has more room for the flow to divert into the gap region around the high pressure zone given the relative nature of the geometry. However, the velocity profile in the gap region is not symmetric and a high velocity region is created just below the upper geometry in the gap region, shown in Figure 5.6. This plot shows the velocity is not symmetric due to the oblateness difference, resulting in a higher velocity on the upper augmentor in comparison to the lower one, which is primarily the reason for the increase in power ratio. It should also be noted that the stability of the flow in the gap region for case $a/D_o = 10/20$ shows considerable variation in velocity just aft of the gap region due to shedding vortices not seen in the $a/D_o = 17/20$ case, shown in the Appendix B in Figures B.4 and Figure B.5.

The second plot provided in Figure 5.2 shows the variance of velocity in the gap with

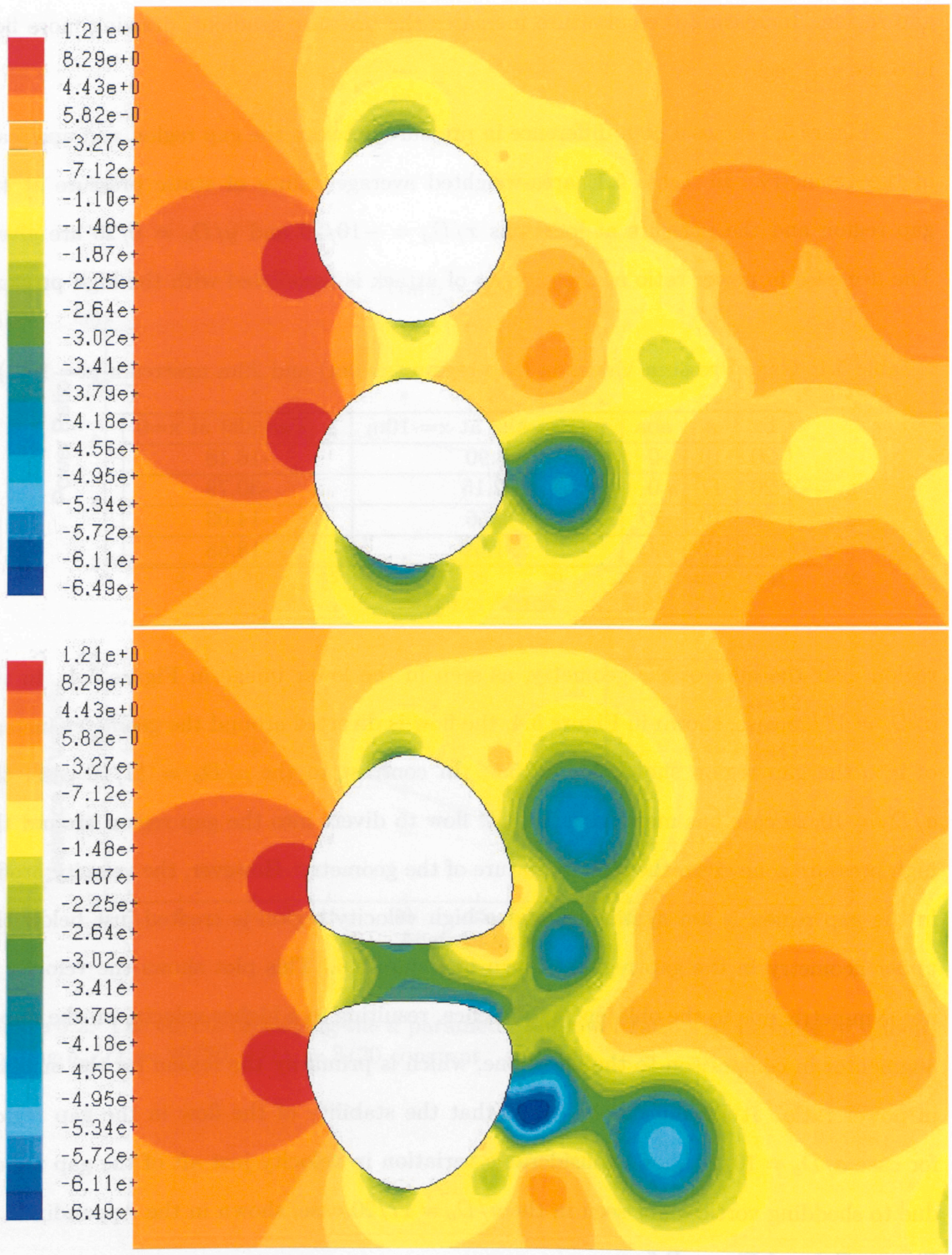


Figure 5.3: Static Pressure Plots for $g/D_o = 3/20$, $b_x/D_o = 20/20$, $a/D_o = 10/20$ (Top) and $a/D_o = 17/20$ (Bottom) at angle of incidence of $0^o$ at time=730s

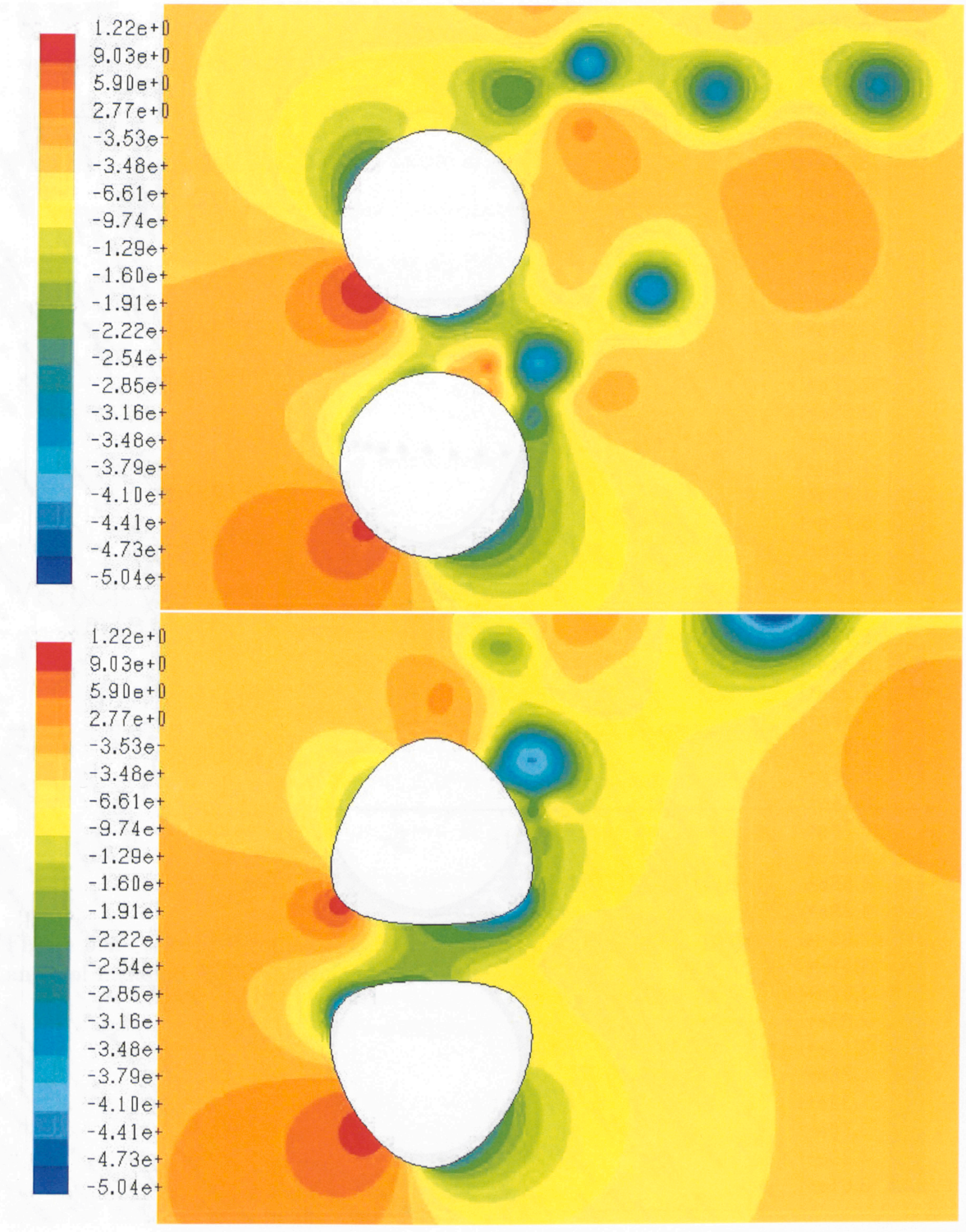


Figure 5.4: Static Pressure Plots for $a/D_o = 10/20$ (top)and $a/D_o = 17/20$ (bottom) at an angle of incidence of $50^o$ and $g/D_o = 3/20$ at time=730s

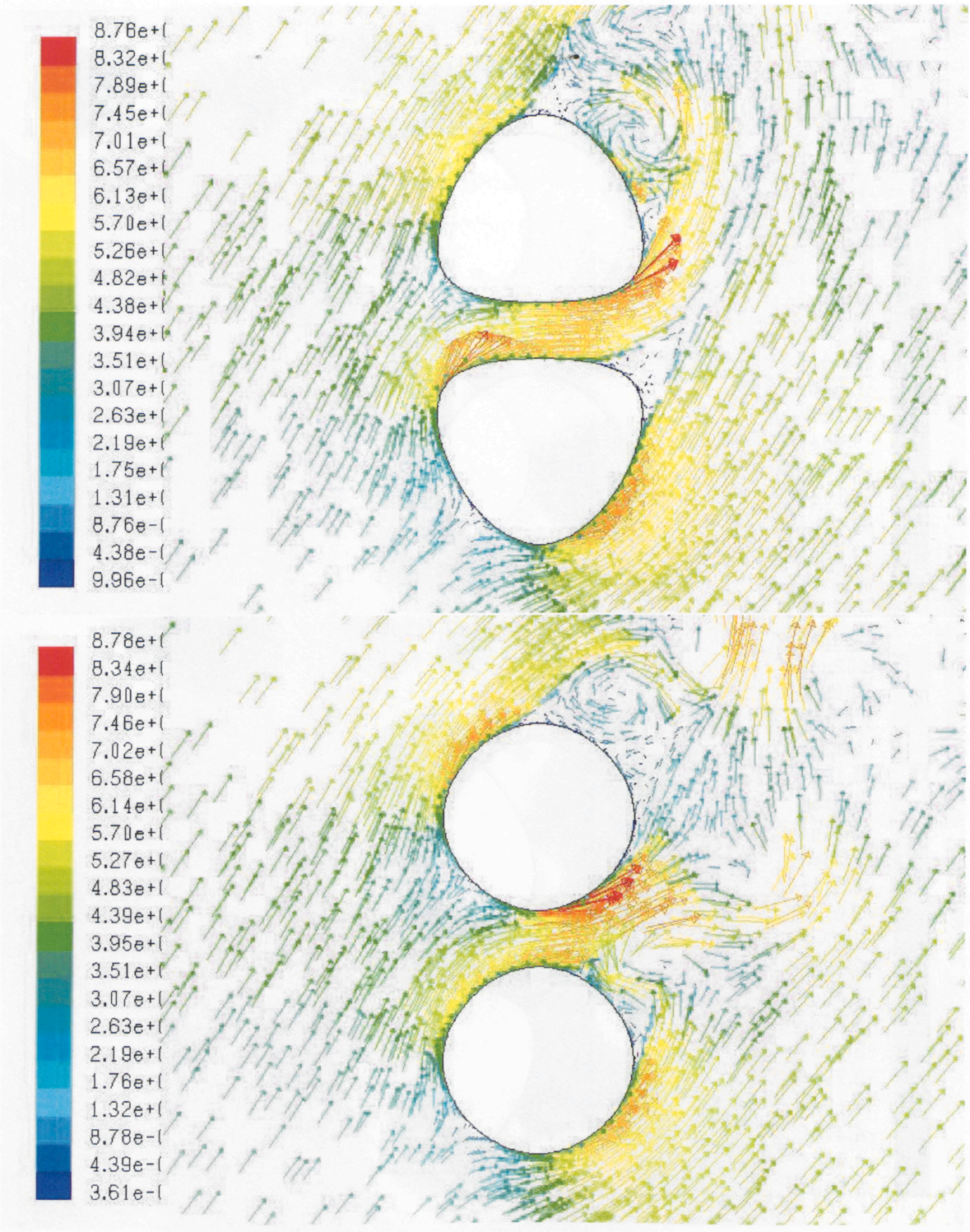


Figure 5.5: Vector Plot of $a/D_o = 17/20$ (Top) $a/D_o = 10/20$ (Bottom) $b_x/D_o = 20/20$, , $g/D_o = 3/20$ at angle of incidence of $50^o$ at time=730s

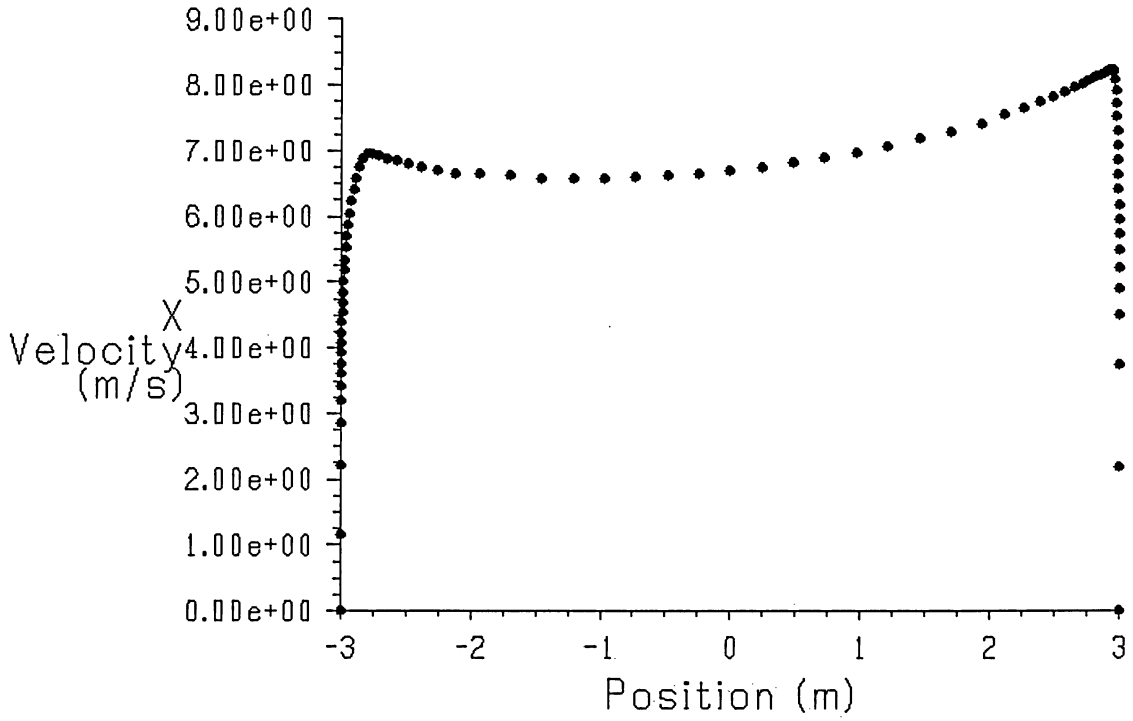


Figure 5.6: Velocity Profile at $A_2$ for $b_x/D_o = 20/20$, $a/D_o = 10/20$, $g/D_o = 3/20$ at angle of incidence of $50^o$ at time=730s

angle of incidence. For all cases, increasing the angle of incidence decreases the variance. This trend can be explained by wake interaction with the gap region. As the angle of incidence increases, the wake of the leading geometry decreases due to the presence of the secondary geometry, shown in Figure 5.5 or in streamline plot in Figure B.3 in Appendix B. The secondary geometry is shedding the strongest vortices and the leading geometry is hardly shedding any at all. Furthermore, due to the high angle of attack, the secondary wake is rotated towards the outer part of the geometry, moving it away from the gap region and thus decreasing its effects on variance in velocity in the gap region.

#### Variation of $a$ Parameter With the Presence of a Simulated Wind Turbine

The next part of the study was to implement a porous media in the gap region to simulate the momentum loss and associated pressure drop caused by the wind turbine. The effects of adding the turbine on the oblateness $a$ parameter study are plotted in Figure 5.7. The trend is similar to Figure 5.2 except the power ratio has been decreased substantially for all cases. The general decrease in power ratio is due to a reduced mass flow through the turbine. Adding the porous medium causes a back pressure in the gap region decreasing the pressure gradient and in turn drawing in less flow. Furthermore, the $a = 15$ case has slightly outperformed the $a = 17$ case the change is small contrary to the simulations performed without the presence of the wind turbine. This indicates the curvature has less of an effect on the power ratio with the presence of the wind turbine since the turbine induces a back pressure decreasing the pressure gradient.

### 5.2.2 The Effects of Varying the Thickness $b_x$ Parameter

The effects of decreasing the thickness $b_x$ parameter increases the power ratio at all angles of attack, using a constant oblateness $a/D_o = 15/20$ and gap size $g/D_o = 3/20$, which is shown in Figure 5.8. These parameters were chosen since they appear to be the optimal

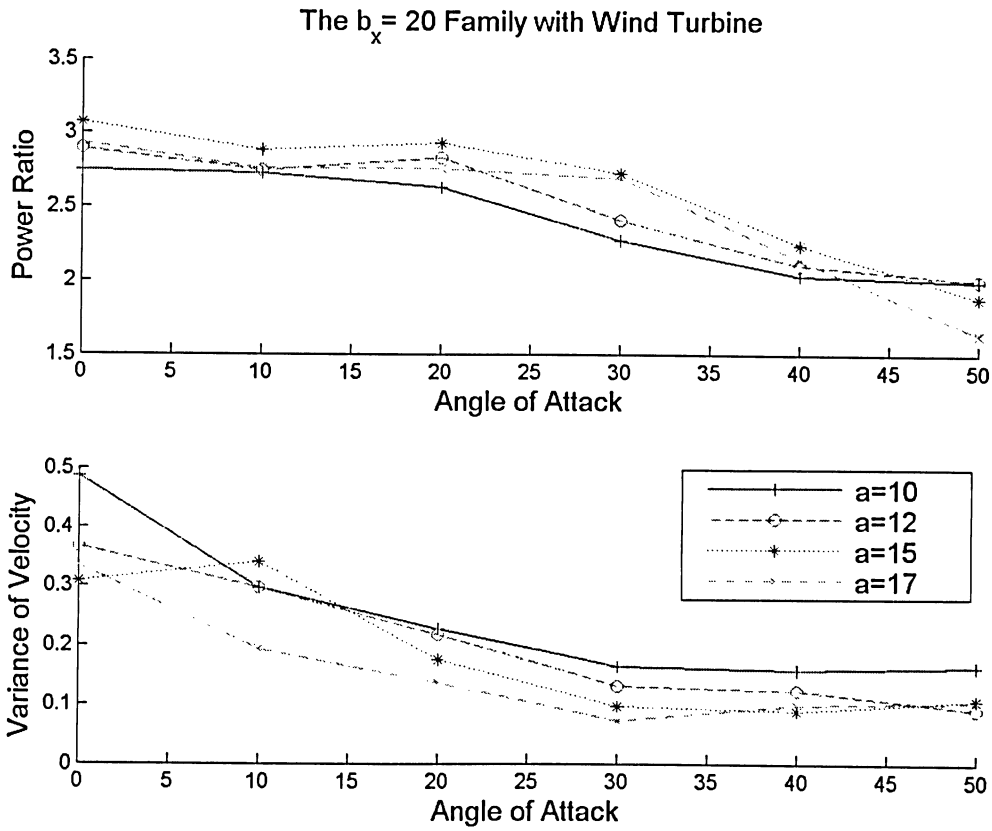


Figure 5.7: The effects of varying the $a$ parameter on power ratio and variance of velocity with the presence of a simulated wind turbine holding $b_x/D_o = 20/20$, $g/D_o = 3/20$ constant at time=730s

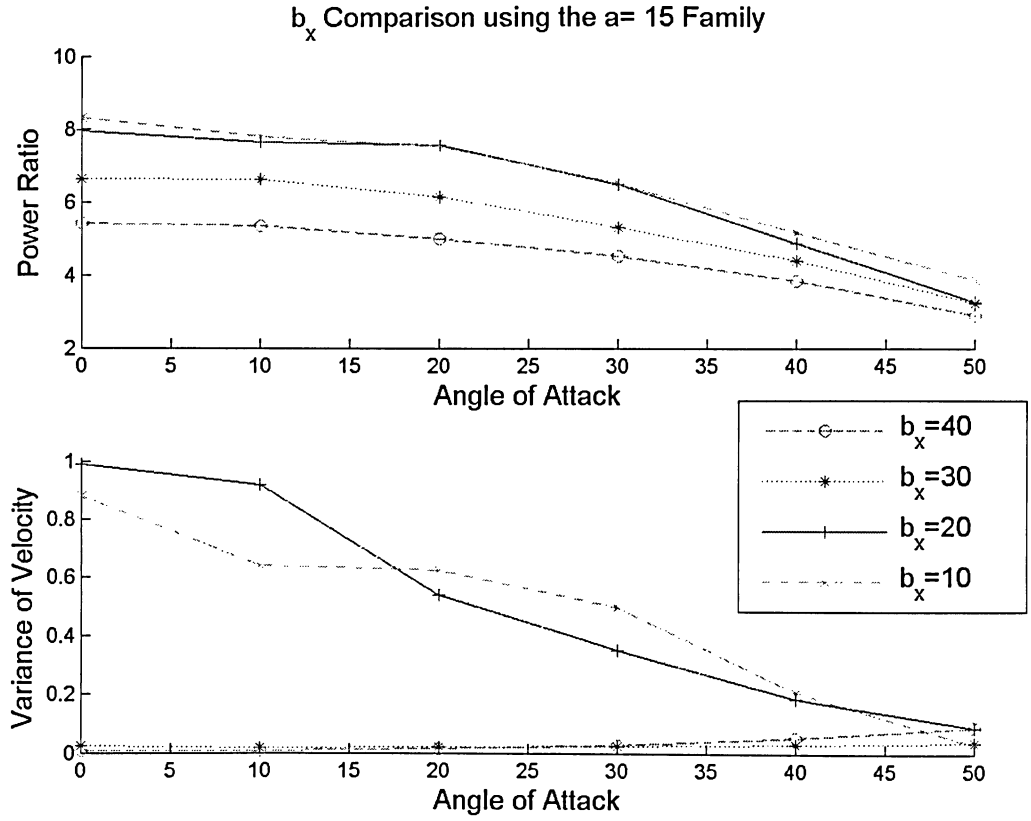


Figure 5.8: The effects of varying the $b_x$ parameter on power ratio and variance of velocity for $a/D_o = 15/40$, $g/D_o = 3/20$ at time=730s

values. The increase in power ratio is associated with an increase in pressure gradient between the upstream flow and in the gap region. The increase in pressure gradient is illustrated in a pressure contour plot in Figure 5.11 and sample pressure points at the inlet and in the gap region are displayed in Table 5.2. At $0^o$ angle of incidence, a substantial pressure difference of 44.7% is shown in case $b_x/D_o = 20/20$ over case $b_x/D_o = 40/20$ in the gap region. This trend can be rationalized by observing the curvature in the gap region and the outer region. By decreasing the $b_x$ parameter, the curvature of the enclosed spline changes such that the curvature at points $B$ and $D$ increase and points $A$ and $C$ decrease. An increase in curvature at $B$, $D$ is associated with an increase in pressure gradient and vice versa, as long as the flow remains attached.

Table 5.2: Pressure Values in Gap region and at inlet for varying $b_x$

| bx | a | aoa | p (Pascals) at inlet | p (Pascals) at x=0 (gap) |
|---|---|---|---|---|
| 20 | 15 | 0 | -1.77 | -39.79 |
| 40 | 15 | 0 | 2.97 | -23.30 |

In cases were $b_x$ is smaller, separation comes into effect because of high curvature at point $B$, decreasing the power ratio at high angles of attack. If the pressure gradient in the gap region is increased, the flow is drawn in and hence in turn increases the power ratio. To justify this rationalization, a set of simulations were conducted with a decrease in the $a$ parameter. By decreasing the oblateness $a$ parameter, the curvature in the gap region increases (point $B$) and decreases on the outer walls (point $D$), which has little effect at zero angle of attack but a significant effect at higher angles of incidence, shown in Figure 5.9. This trend looks similar to an airfoil at an angle of attack and is actually directly related to the lift generated as shown by Fletcher [15] using annular wing sections. Decreasing the oblateness $a$ parameter, the effect is similar to increasing the camber of an airfoil, causing a strengthening of the low pressure region on the upper surface (increased pressure gradient) with increasing angle of incidence. Decreasing the $b_x$, increases the curvature so much near the gap region the pressure gradient changes so rapidly that the flow separates and diverges around the gap region.

High angles of attack and high $b_x$ values cause the geometry to become more blunt in relation to the angle of incidence such that the flow simply travels around both objects. Furthermore, due to a high curvature near the gap entrance, it is difficult for the flow to enter the gap region, shown in the streamline plot in Figure 5.10. However, the cases $b_x/D_o = 10/20$ and $b_x/D_o = 20/20$ are almost identical with the exception that the $b_x/D_o = 10/20$ has a nominal increase in power ratio at angles of incidence $0^o$, $10^o$, $40^o$, $50^o$, indicating a maximum has been reached (Figure 5.8).

The velocity variance plot in Figure 5.8 shows that, if $b_x \leq 20\ m$, the velocity

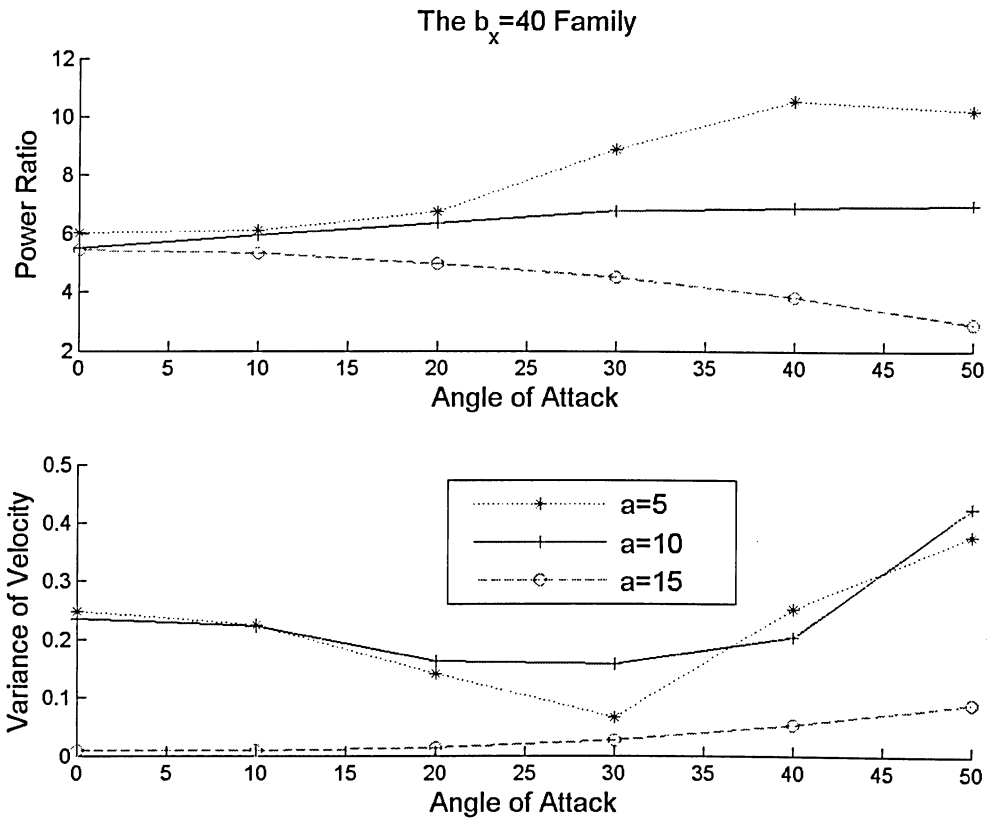


Figure 5.9: Comparision of $b_x = 40/20$ at $g/D_o = 3/20$ at time=730s

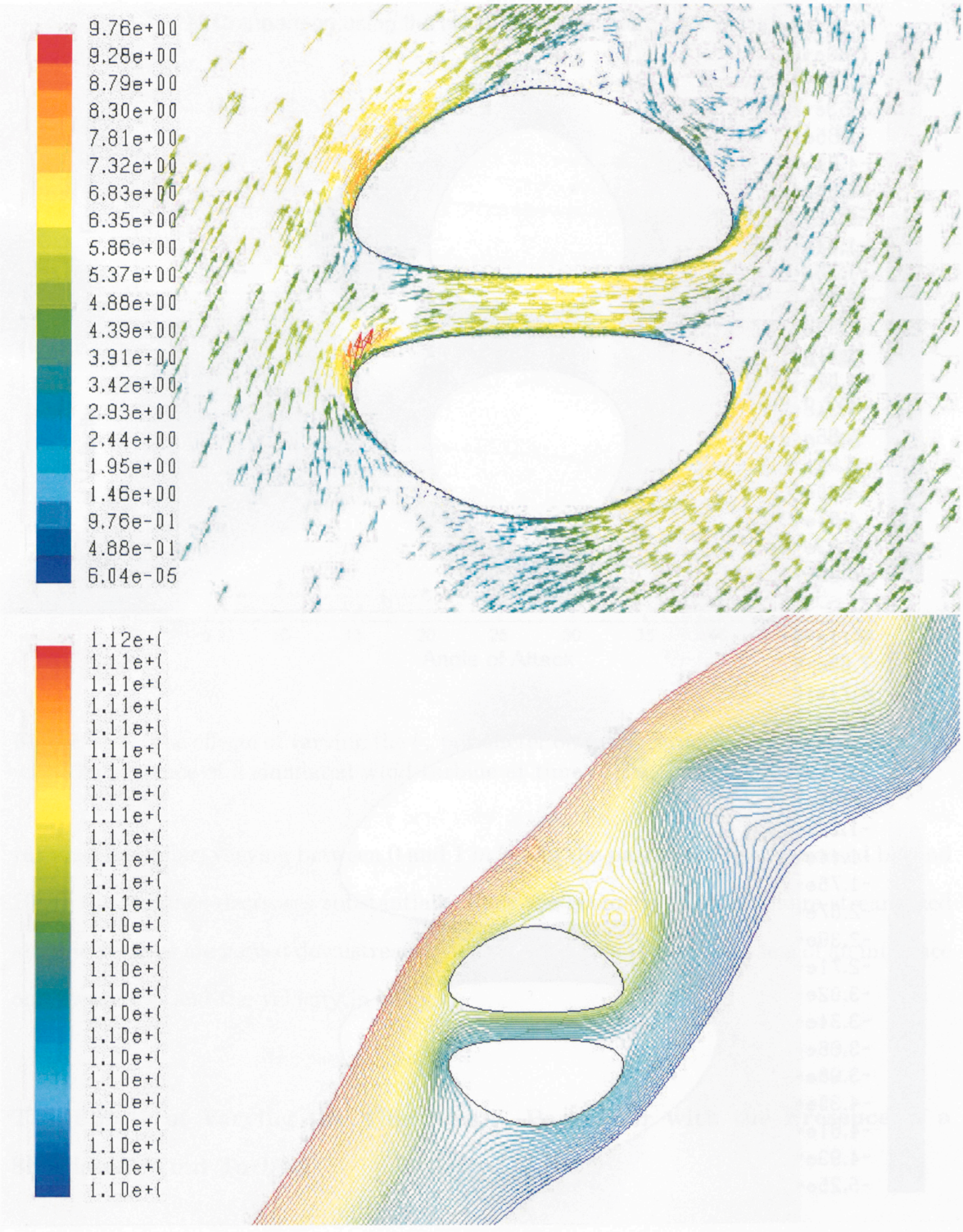


Figure 5.10: Vector (Top) and Pressure Contour plots (Bottom) of $b_x/D_o = 40/20$, $a/D_o = 15/20$, $g = 3/20$ at angle of incidence of $50^o$ at time=730s

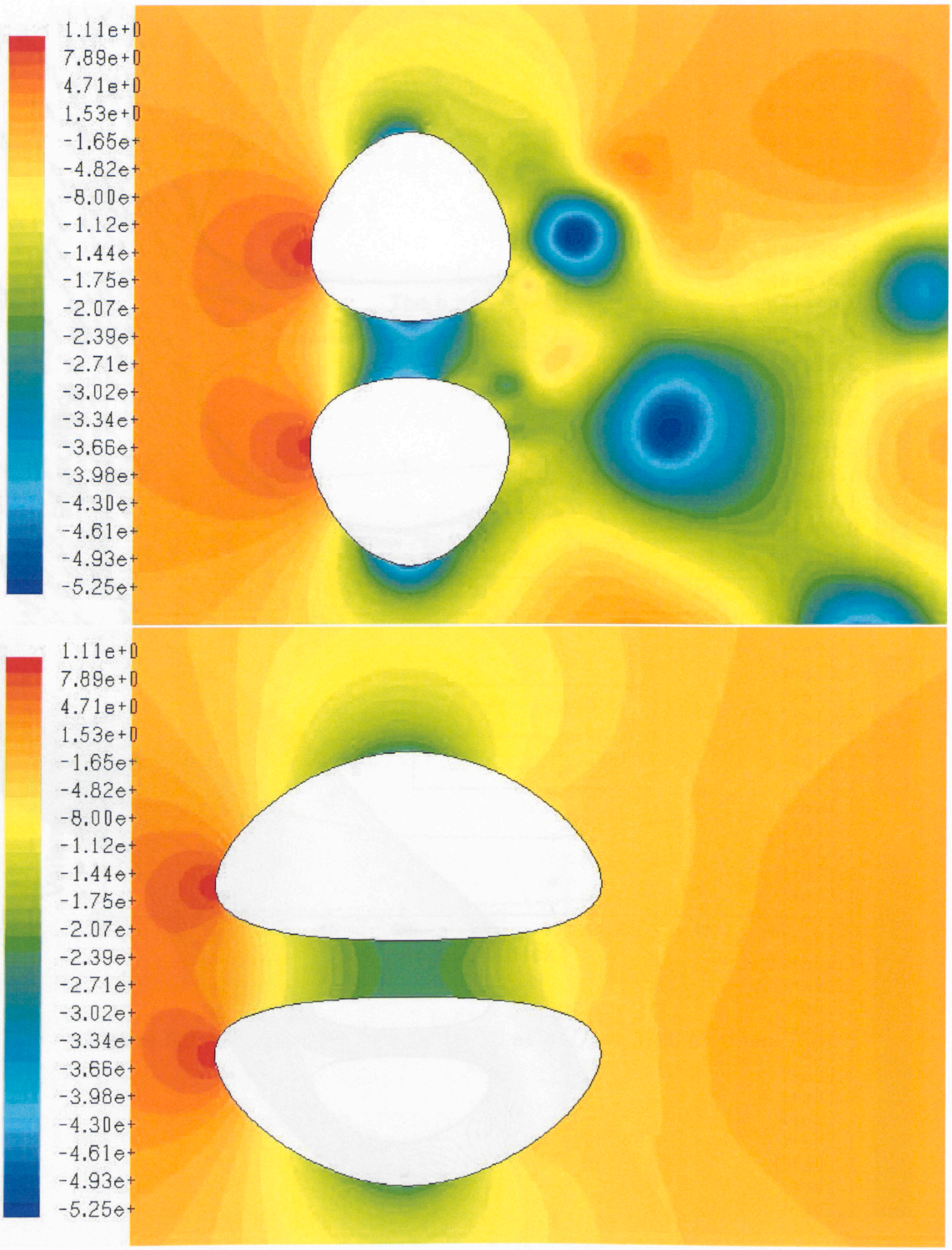


Figure 5.11: Static Pressure Plots for $b_x/D_o = 20/20$ (Top) and $b_x/D_o = 40/20$ (Bottom) at an angle of incidence of $50^o$, $g/D_o = 3/20$, $a/D_o = 15/20$ at time=730s

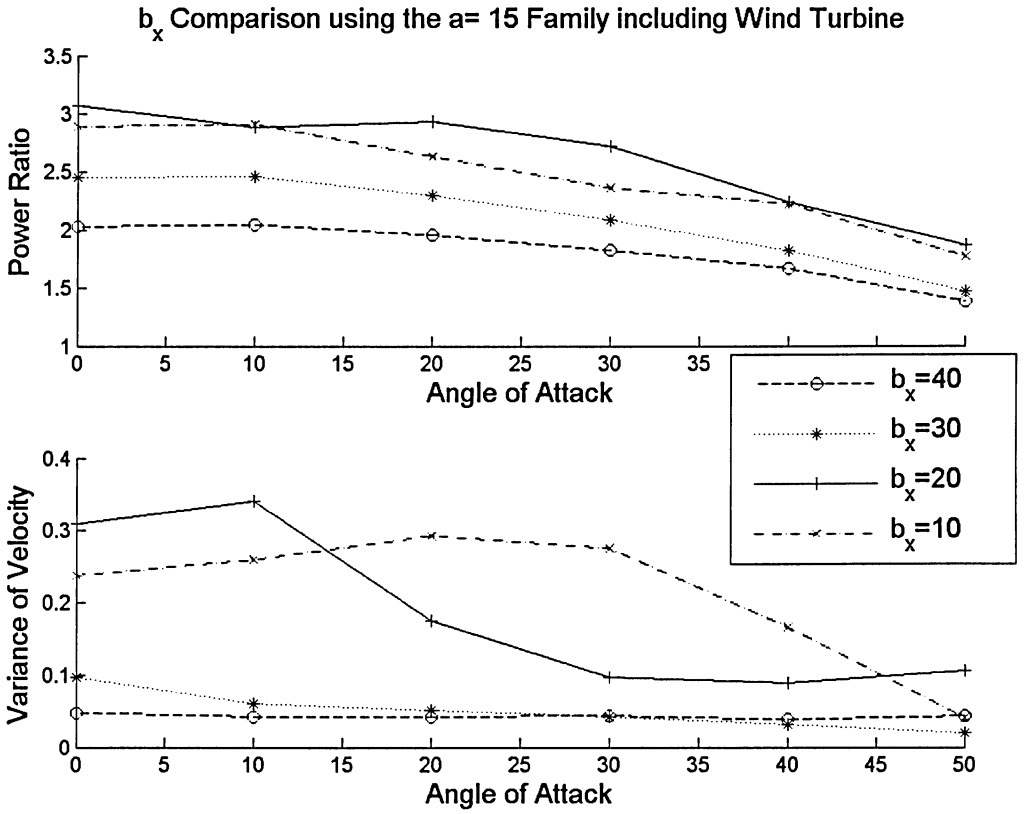


Figure 5.12: The effects of varying the $b_x$ parameter on power ratio and variance of velocity with the presence of a simulated wind turbine at time=730s

variance is similar, varying between 0 and 1 $m/s$. As the parameter $b_x$ is increased beyond 20 $m$, the variance decreases substantially since the geometry becomes more streamlined and the vortices are moved downstream of the gap region and thus have less of an influence on power ratio and the velocity in the gap.

### The Effects of Varying the Thickness $b_x$ Parameter with the Presence of a Simulated Wind Turbine

Similar to the previous section, the study next examined how the presence of a wind turbine would effect the variation on the $b_x$ parameter, shown in Figure 5.12. The plot

shows a general decrease in power ratio, as was discussed in the previous analysis. For the $b_x = 20$ case, a slight improvement was noticed at angles of $20^o$ and $30^o$ over the $b_x = 10\ m$ case. In Figure 5.13, the contours of static pressure are plotted. It is obvious from Figure 5.13 that the increase in power ratio is due to the increase in pressure gradient. Table 5.3 provides pressure values taken at the inlet and an area-weighted average of pressure across the gap region, the $b_x/D_o = 20/20$ having a much higher difference, indicating a higher pressure differential.

Table 5.3: Pressure Values in Gap region and at inlet for varying $b_x$ with the presence of a wind turbine

| bx | a | aoa | p (Pascals) at inlet | p (Pascals) at x=0 (gap) |
|---|---|---|---|---|
| 10 | 15 | 20 | 2.72 | -16.74 |
| 20 | 15 | 20 | -3.08 | -42.85 |

### 5.2.3 The Effects of Varying the Gap size $g/D_o$

The next parameter explored was the gap size. In this portion of the study, the optimal parameters found in the previous sections were held constant at $b_x/D_o = 20/20$, $a/D_o = 15/20$ and $D_o = 20$. Figure 5.15 shows that increasing the gap size decreased the power ratio in all cases. The decrease can be associated with the two low pressure areas of the gap region moving further in proximity to each other and effectively creating a larger less-concentrated low pressure region, resulting in a lower pressure gradient, as shown in Figure 5.14. Sample pressures at the inlet region and area-weighted average pressures are shown in Table 5.4. However, there is a realistic limit to how small the wind turbine can be, based on efficiency, versus size. As the wind turbine becomes smaller, the efficiency of the turbine decreases and the power extracted is directly related to the sweeping area. Increasing the radius of a turbine increases the power extracted through a radius squared relationship. Thus, it is expected that an optimum point should exist, and the subject

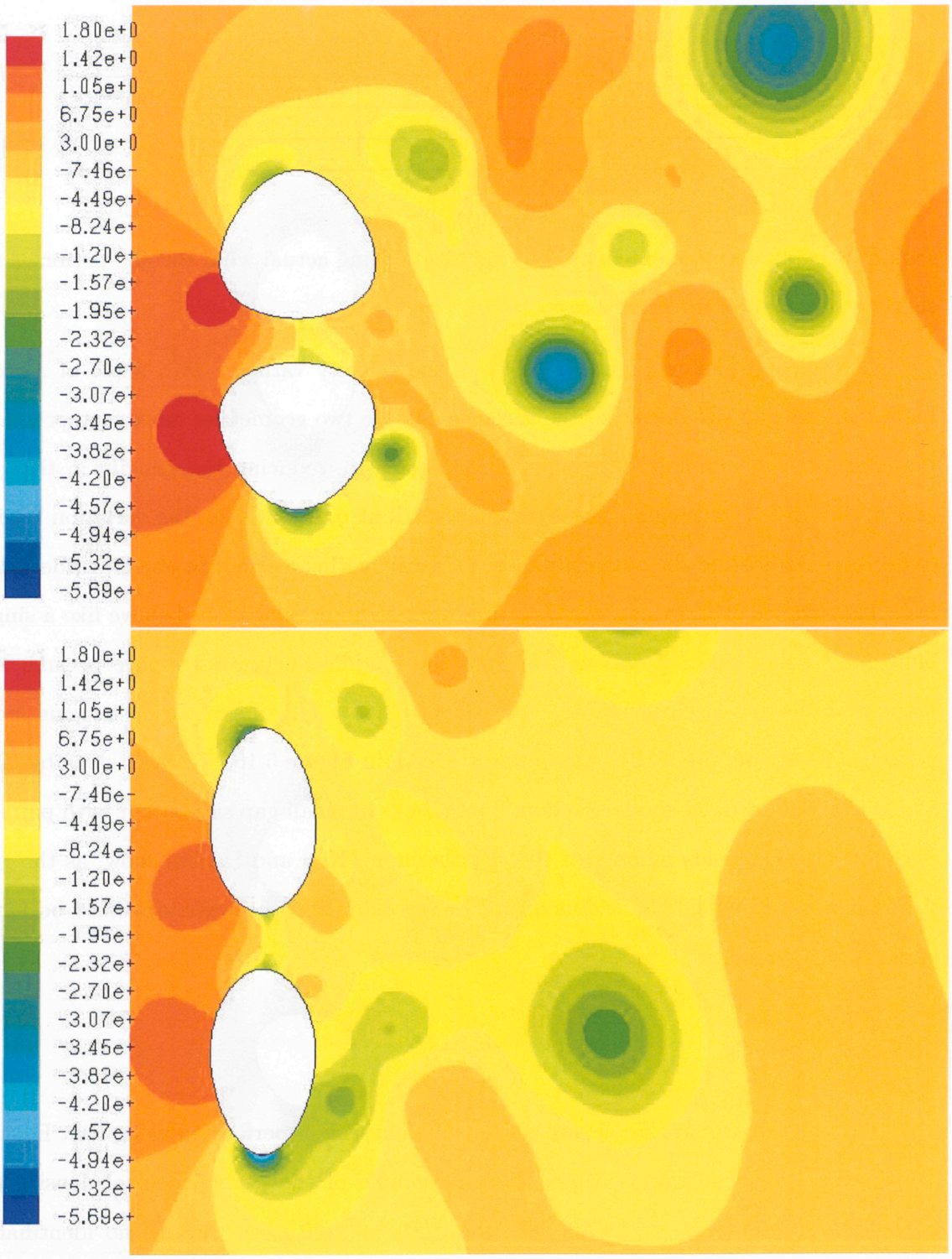


Figure 5.13: Static Pressure Plots for $b_x/D_o = 20/20$ (Top) and $b_x/D_o = 10/20$ (Bottom) at an angle of incidence of $20^o$ at time=730s

Table 5.4: Pressure Values in Gap region and at inlet for varying $g$

| bx | a | aoa | $g/D_o$ | p (Pascals) at inlet | p (Pascals) at x=0 (gap) |
|---|---|---|---|---|---|
| 20 | 15 | 0 | 3/20 | 6.67 | -32.03 |
| 20 | 15 | 0 | 12/20 | -4.44 | -14.04 |

should be explored more extensively in the future using actual wind turbine performance charts at given rotor sweeping areas.

The second plot in Figure 5.15 shows the velocity variance with angle of attack. Increasing the gap size decreases the variance. As the two geometries move further apart, the effects of the combined wake interaction decreases, reducing the velocity in the gap region. When the gap region gets extremely small at $g/D_o = 3/20$, the variation begins to decrease, indicating the augmenters are primarily acting as a single object, rather than two. The smaller the gap size, the more the wake structure begins to behave like a single bluff body wake. Also, it was noticed that the random fluctuating nature became less random as the gap sized increased. At around $g/D_o = 1/2$, the variation became more periodic (steady period of $16s$) and uniform, shown in Figure 5.16. Research done by Kim and Durbin [19] showed similar random fluctuations at small gap sizes occur with pairs of cylinders at a Reynolds number of $10^5$. Furthermore, Kim and Durbin show, as the gap size is increased beyond the radius of one of the cylinders, the wake structure becomes uniform and symmetric.

### Spectral Analysis

To determine the primary frequency a spectral analysis was performed using Fast Fourier Transforms. In Figure 5.17, shows the an example of the power spectral density for $g/D_o = 3/20$ and $g/D_o = 12/20$. For the $g/D_o = 3/20$ case, there is no identifiable primary frequency but the figure shows that all the oscillations occur below 0.1 $Hz$. For the $g/D_o = 12/20$ case, the primary frequency occurs at 0.0625 $Hz$.

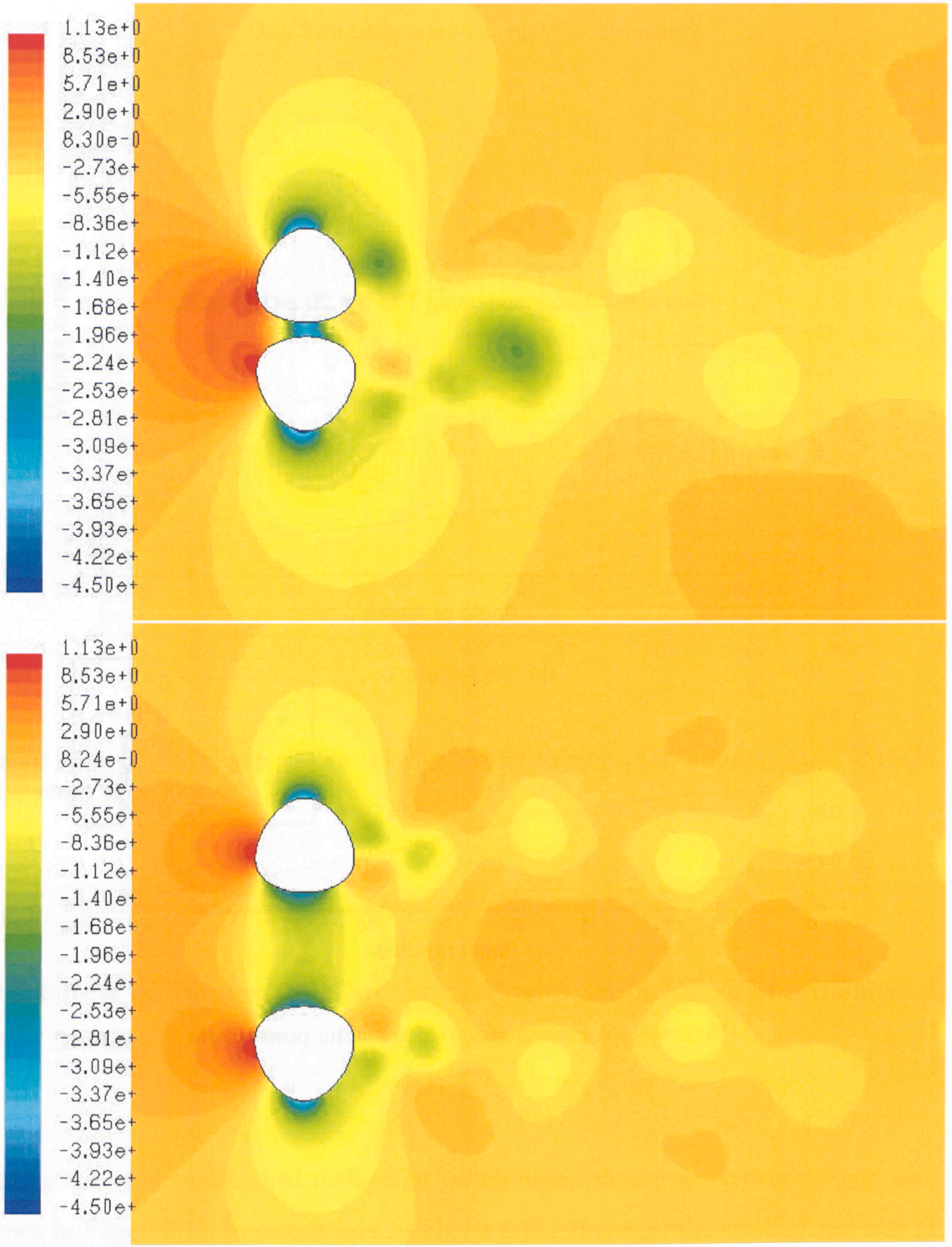


Figure 5.14: Static Pressure Plots for $g/D_o = 3/20$ (Top) and $g/D_o = 12/20$ (Bottom) at an angle of incidence of $0^o$ at time=730s

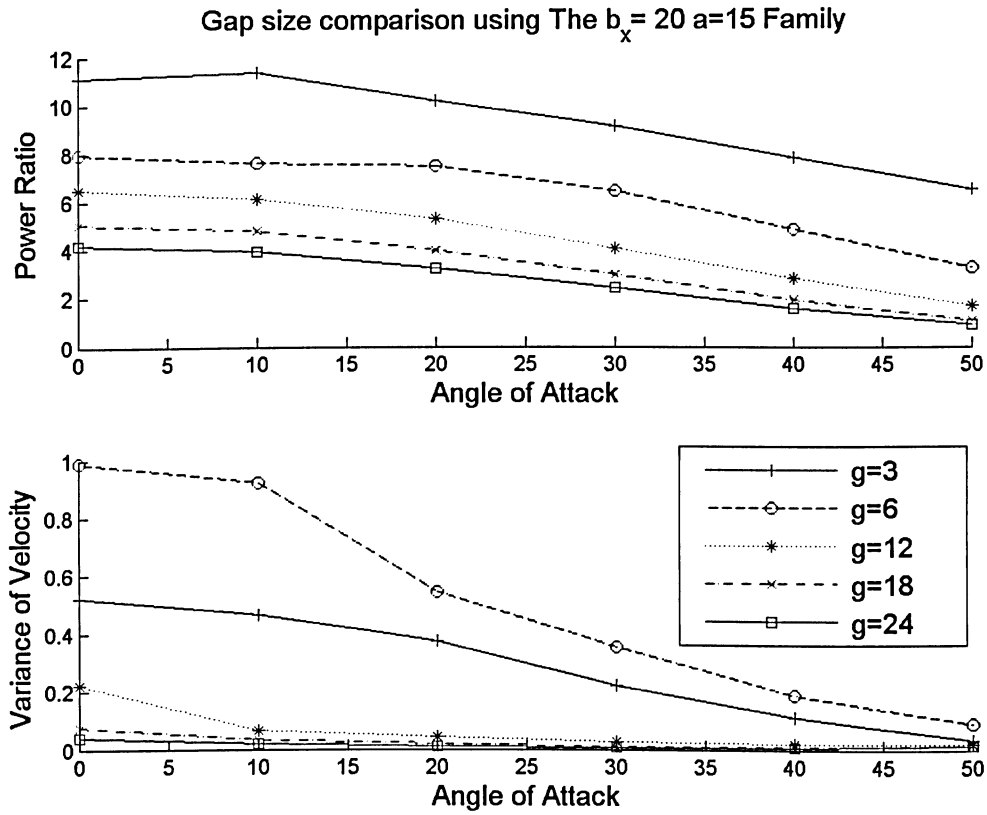


Figure 5.15: Effects of gap size on the power ratio

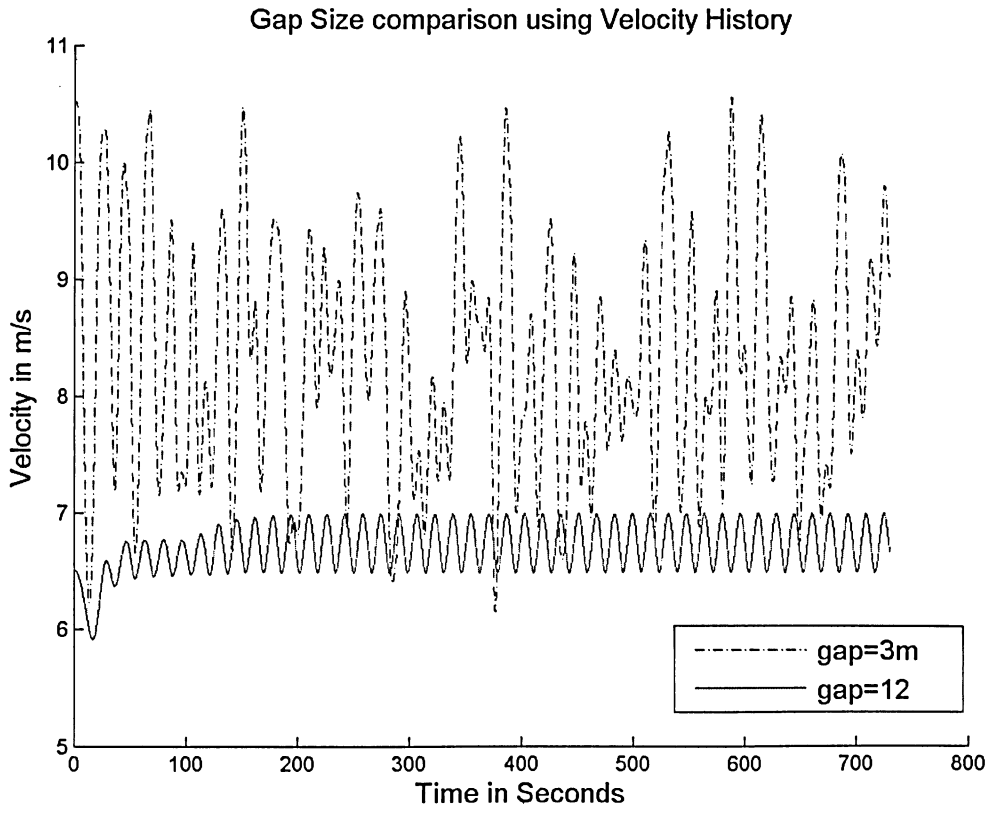


Figure 5.16: Effects of gap size on velocity history using $b_x/D_o = 20/20$, $a/D_o = 15/20$ at $0^o$ angle of incidence

### The Effects of Varying the Gap size $g/D_o$ with the presence of a Simulated Wind Turbine

Adding the wind turbine had little effect on the trend shown by varying the gap size, shown in Figure 5.18, in comparison to Figure 5.15. However, the smallest gap size of $g/D_o = 3/20$ proved to drop the $PR$ the most (by 3.28 times), whereas the largest gap size of $g/D_o = 24/20$ dropped PR by only 2.15 times.

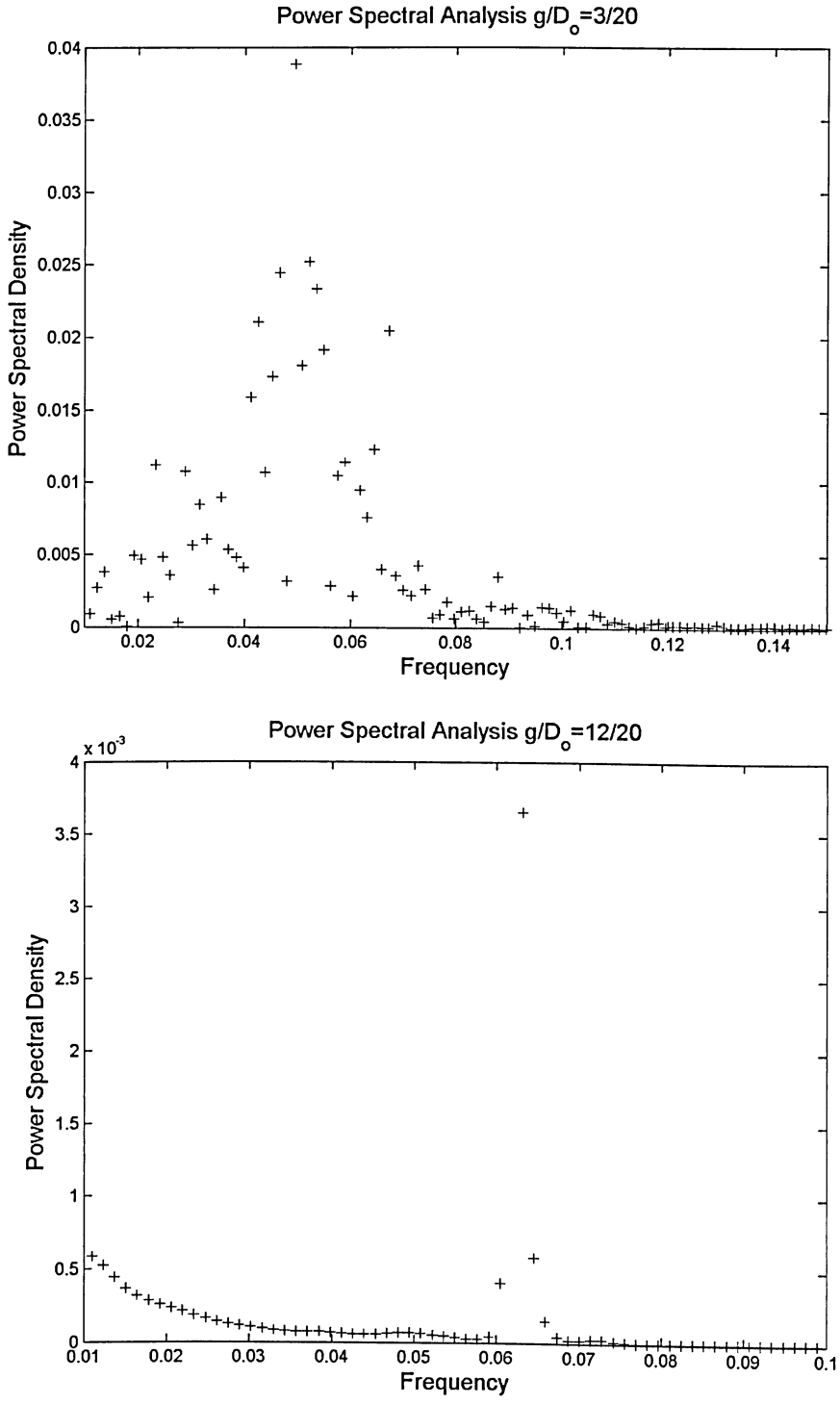


Figure 5.17: Spectral Analysis $g/D_o = 3/20$ (Top) and $g/D_o = 12/20$ (Bottom) at an angle of incidence of $0^o$

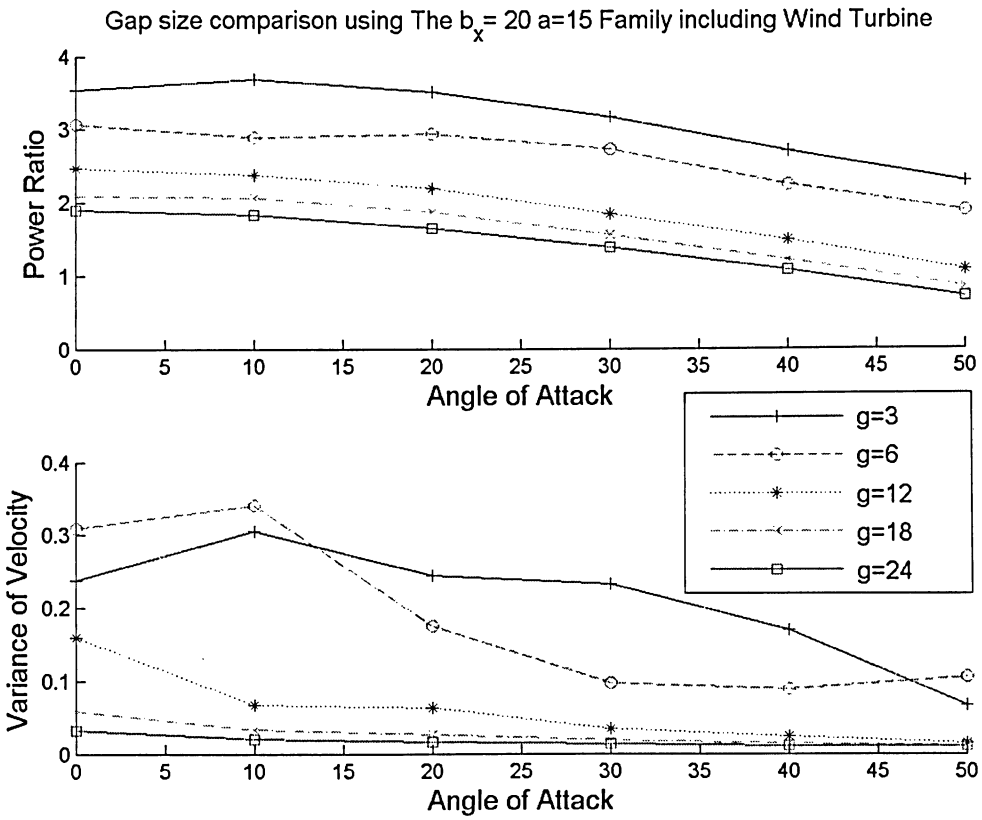


Figure 5.18: Effects of gap size on the power ratio with the presence of the wind turbine at time=730s

### 5.2.4 The Effects of Velocity

The next objective in the study was to determine how velocity affects the power ratio, or, in other words, what the Reynolds number effects were. Simulations were conducted at $V_o = 4.16,\ 8.32,\ 12.48\ m/s$ holding the following variables constants: $a/D_o = 15/20$, $b_x/D_o = 20/20$ and $g/D_o = 3/20$. The effects of velocity on the power ratio are shown in Figure 5.19. The plot reveals that velocity has little effect on the power ratio at angles of attack greater than $20^o$. However, at angles of incidence lower than $20^o$, the power ratio at $V_o = 4.16$ m/s is much less than at $V_o = 8.32$ m/s and $V_o = 12.48$ m/s. These results indicate that the power ratio is independent of Reynolds number above $1 \times 10^6$.

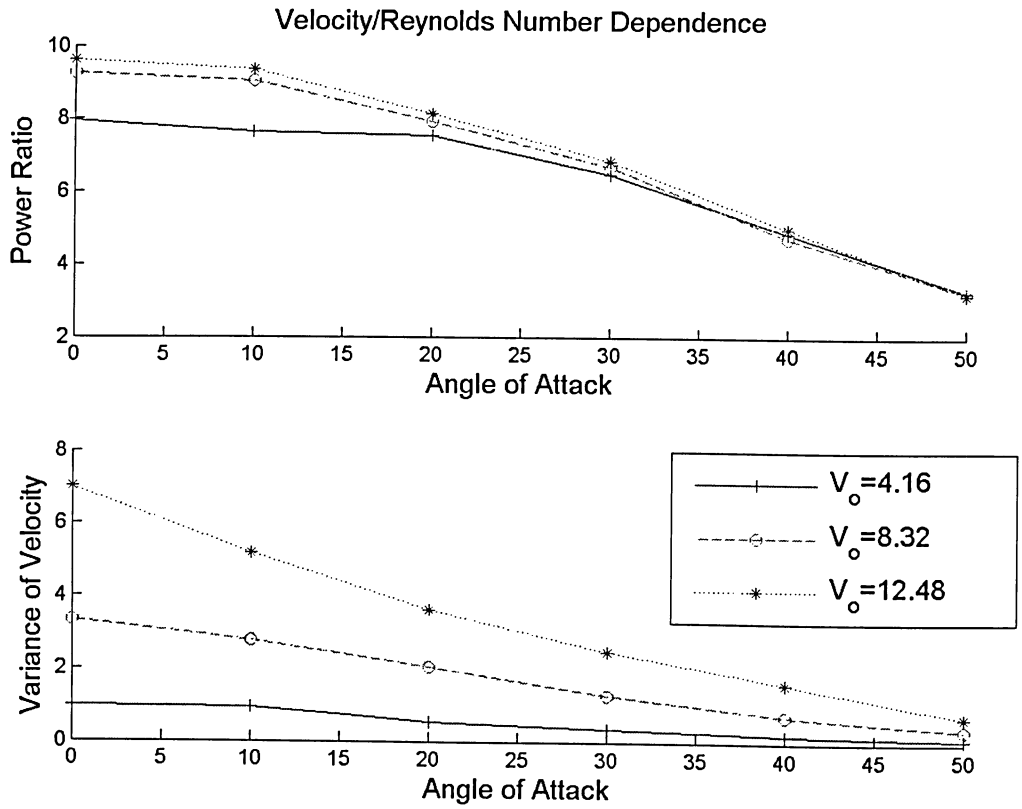


Figure 5.19: Effects of Velocity on power ratio using $b_x/D_o = 20/20$, $a/D_o = 15/20$, $g/D_o = 3/20$ at angle of incidence of $0^o$

However, increasing the had a dramatic effect on the velocity variation through the gap region. Increasing the velocity increases the variation at zero angle of attack by over 3 times for the $V_o = 8.32$m/s case and 7 times for the $V_o = 12.48$ m/s case when compared to the $V_o = 4.16$ m/s case. This indicates increasing the Reynolds number increases the strength of the vortices, and in turn affecting the velocity in between the buildings.

**The Effects of Velocity with the presence of a Simulated Wind Turbine**

The effects of the wind turbine on the velocity study are plotted in Figure 5.20. Adding in the turbine effects showed that Reynolds number has little effect on the power ratio. In contrast to the case where no turbine was present even at low velocities and low angles of incidence, the power ratio proved to be similar to that at the other two velocities.

### 5.2.5 Low Speed Study

The goal of this section was to find the lowest speed possible for wind turbine power generation. For this section, little variation in angle of incidence was assumed, thus, the optimal geometry $b_x/D_o = 20/20$, $a/D_o = 15/20$, $g/D_o = 3/20$ at $0^o$ angle of incidence, was used as the case study. The lowest speed a turbine can generate power economically is 15 $km/hr$ or 4.16 $m/s$ as stated by Ontario Power Generation [21]. Therefore, the study decreased the free stream velocity from 4.16 $m/s$ until a velocity close to $V_o = 4.16$ m/s was achieved in the gap. Figure 5.21 shows that, at a free stream velocity of $V_o = 2$ $m/s$ the throat velocity became $V_2 = 4.16$ $m/s$. This means areas with wind velocities typically at 2 $m/s$, which would not normally be considered feasible for wind turbine power generation, can produce power by using this specific geometry to augment.

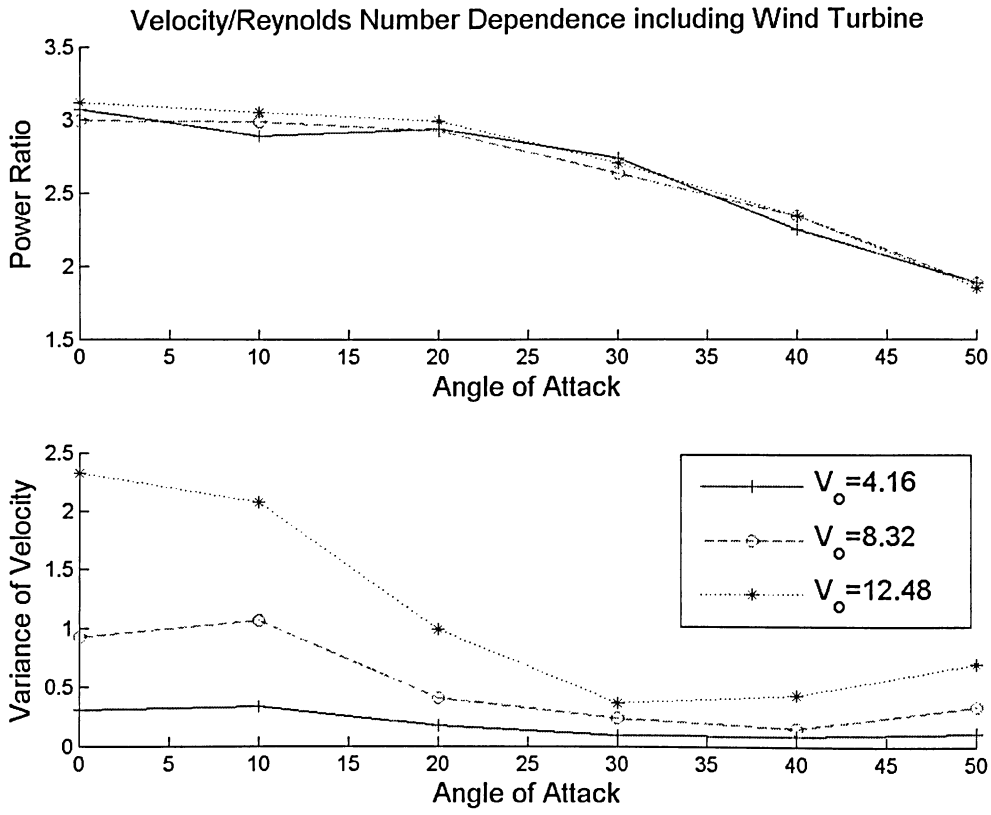


Figure 5.20: Effects of Velocity on power ratio with the presence of the wind turbine

## 5.3 Three Dimensional Results

The three dimensional performance of the augmentors was explored using an extension of the 2D case ($b_x/D_o = 20/20$, $a/D_o = 15/20$, $g = 3/20$) into the $3^{rd}$ dimension at angles of incidence $0^o$, $10^o$, $50^o$. The ground was specified as a no-slip boundary condition while the remaining boundaries were set as velocity-inlets with a uniform velocity of $V_o = 4.16$ m/s. The integrated velocity history plots in the gap region are shown in Figures 5.22, 5.23 and 5.24, for angles $0^o$, $10^o$ and $50^o$, respectively. The plots reveal the gap velocity oscillations have been damped out in the 3D case, with the mean well above the value found in the 2D cases. The reason for this occurrence is the 3D interaction of the vortex shedding dampening out the variance. Furthermore, the abrupt ending of the geometry

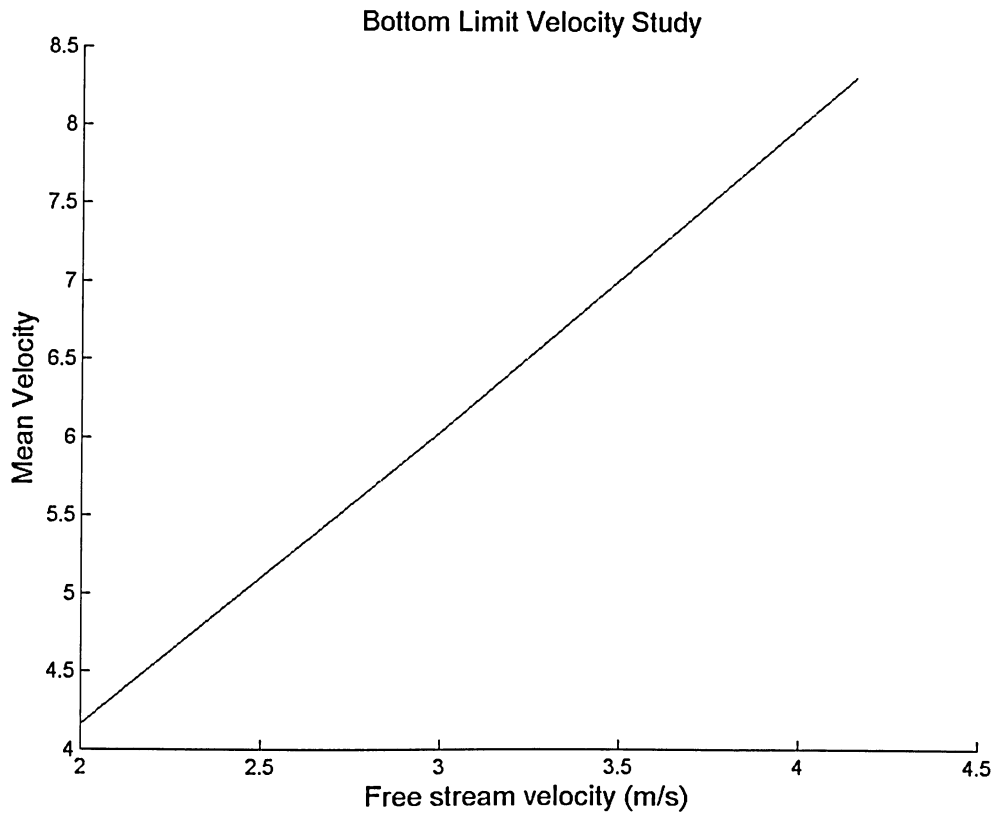


Figure 5.21: Low Velocity Study using $b_x/D_o = 20/20$, $a/D_o = 15/20$, $g/D_o = 3/20$ at $0^o$ angle of incidence

causes particles to be shed off the rooftop causing further 3D mixing shown in the particle release plots in Figure 5.25. Notice the particles that travel over the roof top and descend downwards indicate the shedding off the roof top is causing additional mixing of the wake and in turn dampening out the variance of velocity in the gap region. It should be noted that very little flow is diverted above the geometry making the 2D simulations fairly accurate for optimization purposes. The plots also show that, as the angle increases, the mean of the 3D results increases significantly compared to the 2D results. This indicates more flow is diverted into the gap region at high angles of incidence in comparison to the 2D.

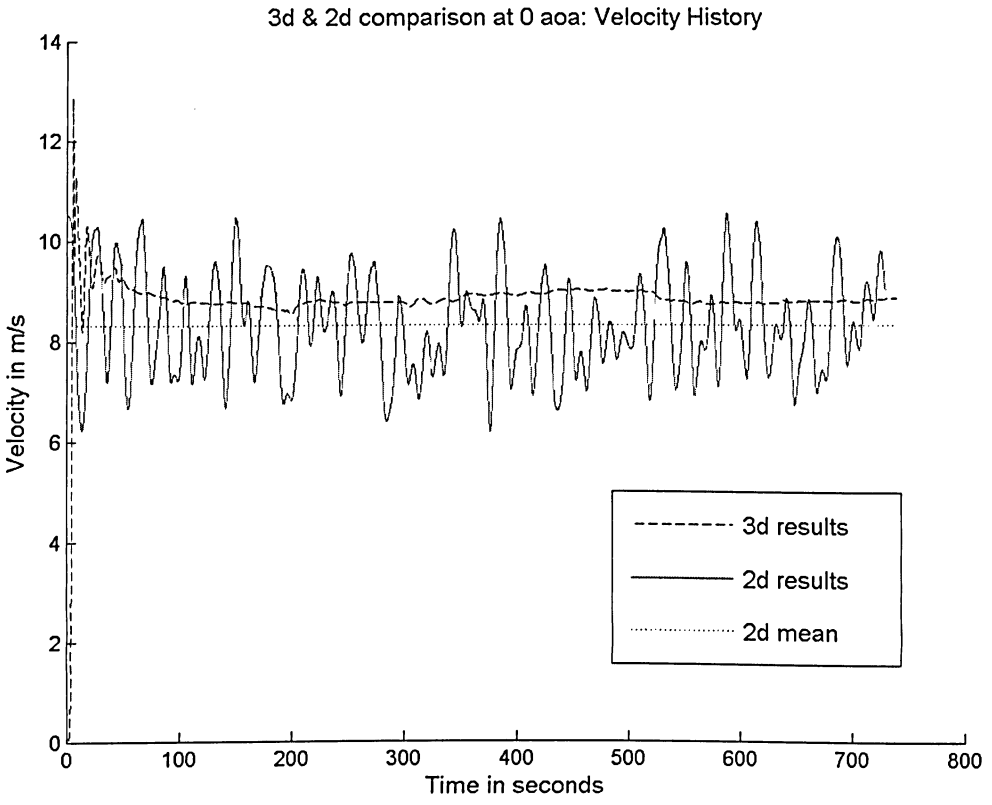


Figure 5.22: 3D compared to 2D at angle of incidence of $0^o$ for $b_x/D_o = 20/20$, $g/D_o = 3/20$, $a/D_o = 15/20$ and $D_o = 20m$ at time=730s

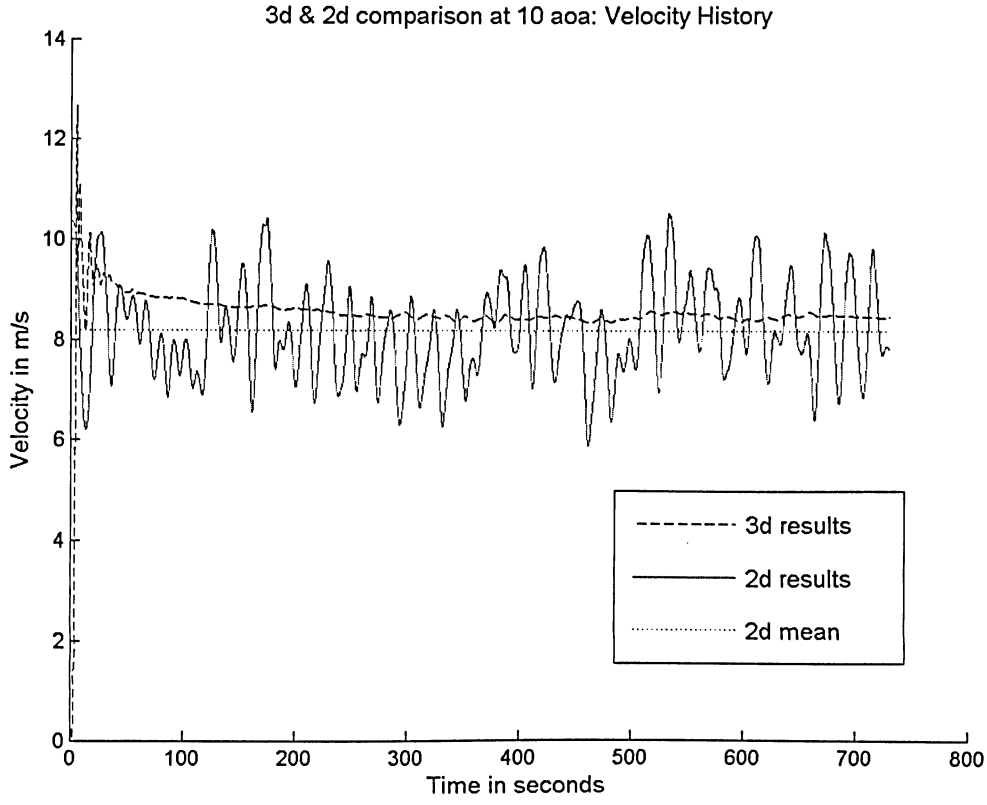


Figure 5.23: 3D compared to 2D at angle of incidence of $10^o$ for $b_x/D_o = 20/20$, $g/D_o = 3/20$, $a/D_o = 15/20$ and $D_o = 20m$ at time=730s

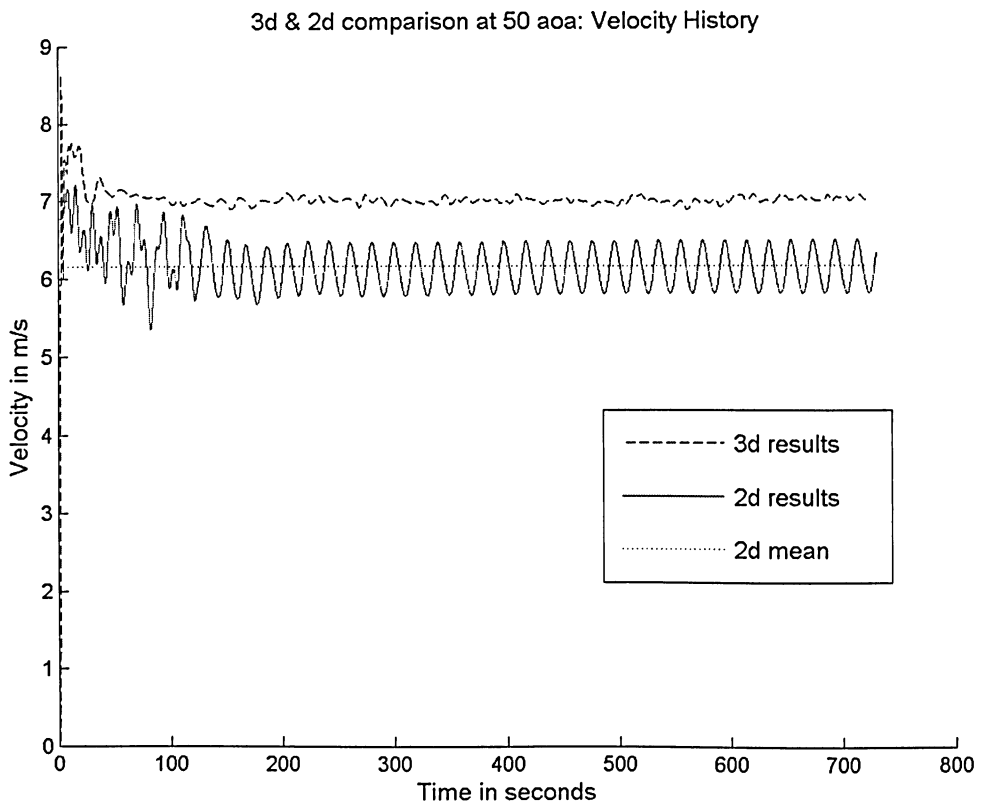


Figure 5.24: 3D compared to 2D at angle of incidence of $50^o$ for $b_x/D_o = 20/20$, $g/D_o = 3/20$, $a/D_o = 15/20$ and $D_o = 20m$ at time=730s

### 5.3.1 Power Ratio as a Function of Building Height

Using the 3D results, an integration of velocity was taken at different heights to find out how the power ratio varied with building height, shown in Figure 5.26. Near the ground, the power ratio drops off to zero which is due to the no-slip condition specified at that boundary. The power ratio increases over the first $20m$ where it reaches a maximum at a $PR = 6.7015$. This maximum occurs due to the boundary layer development along the ground, which causes the flow to divert upwards, at a higher velocity. In between $30m$ and $70m$, the power ratio remains relatively constant with an average $PR = 6.3782$ until it rises again at $80m$ to $PR = 6.5887$ and drops off sharply to 2.6679 at $100m$. This rise and drop is caused by a stagnation condition just aft of the roof geometry in the wake region. In Figure 5.27 the vector plot on the top shows the flow diverting upwards over the roof geometry and descending back into the wake region while the flow just under this is diverting upwards to avoid a large stagnation region near the ground shown in the bottom of Figure 5.27 of the velocity magnitude plot. Therefore, due to the down flow coming off the roof and the up flow coming out of the gap region, the flow is colliding just downwind of the roof section, creating a stagnation and resulting in the power ratio drop off at $100m$. This effect can most likely be reduced by smoothing the roof edges or using a capping geometry to join the buildings. Using an airfoil capping geometry could induce a low pressure region near or on the roof, reducing the separation and forcing more flow through the gap region. Furthermore, experiments found by Campbell *et al* [4] showed numerically and experimentally that shrouding around the turbine can further increase the power ratio.

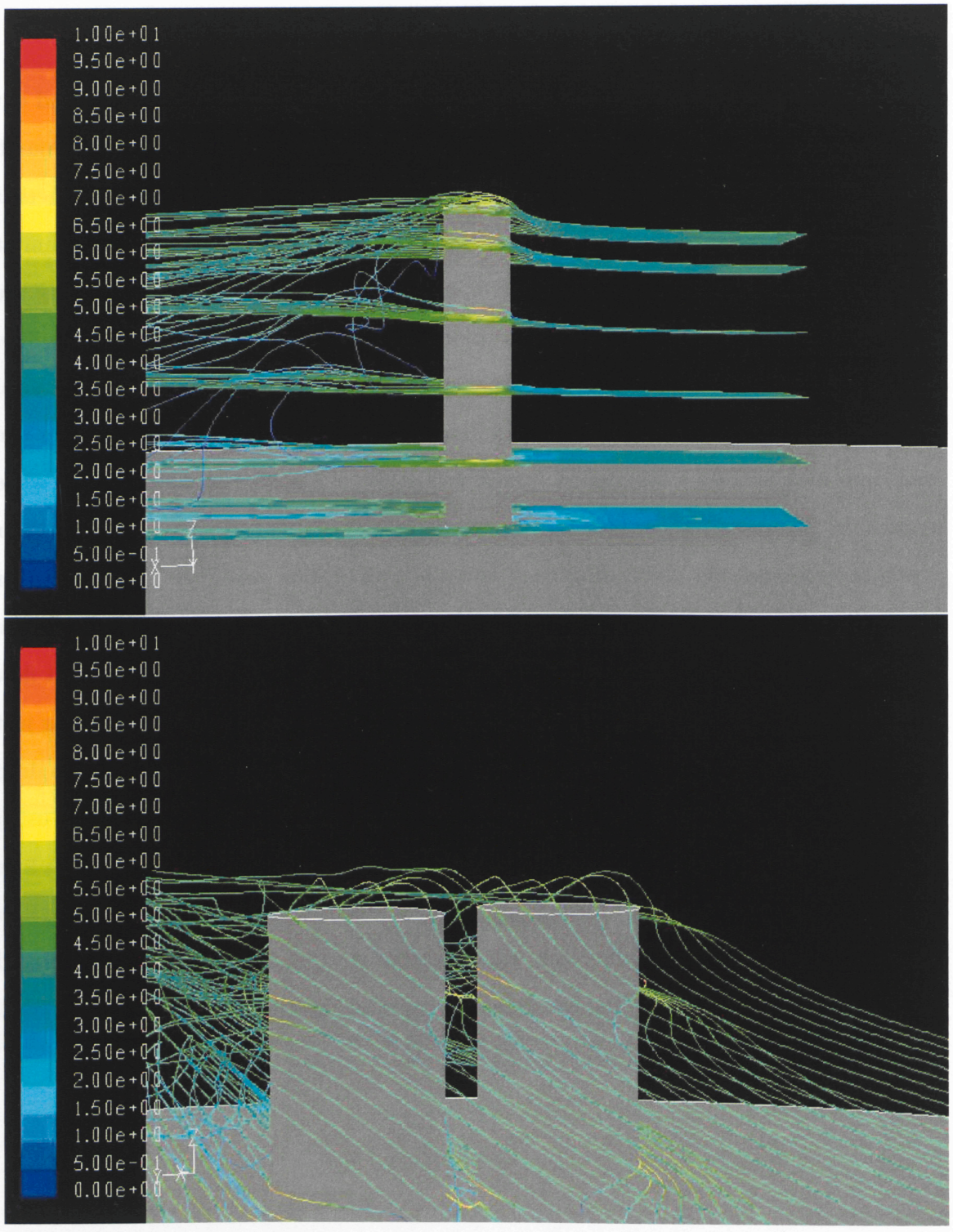


Figure 5.25: 3D Particle release at angle of incidence of $0^o$ for $b_x/D_o = 20/20$, $g/D_o = 3/20$, $a/D_o = 15/20$ and $D_o = 20m$ at time=730s

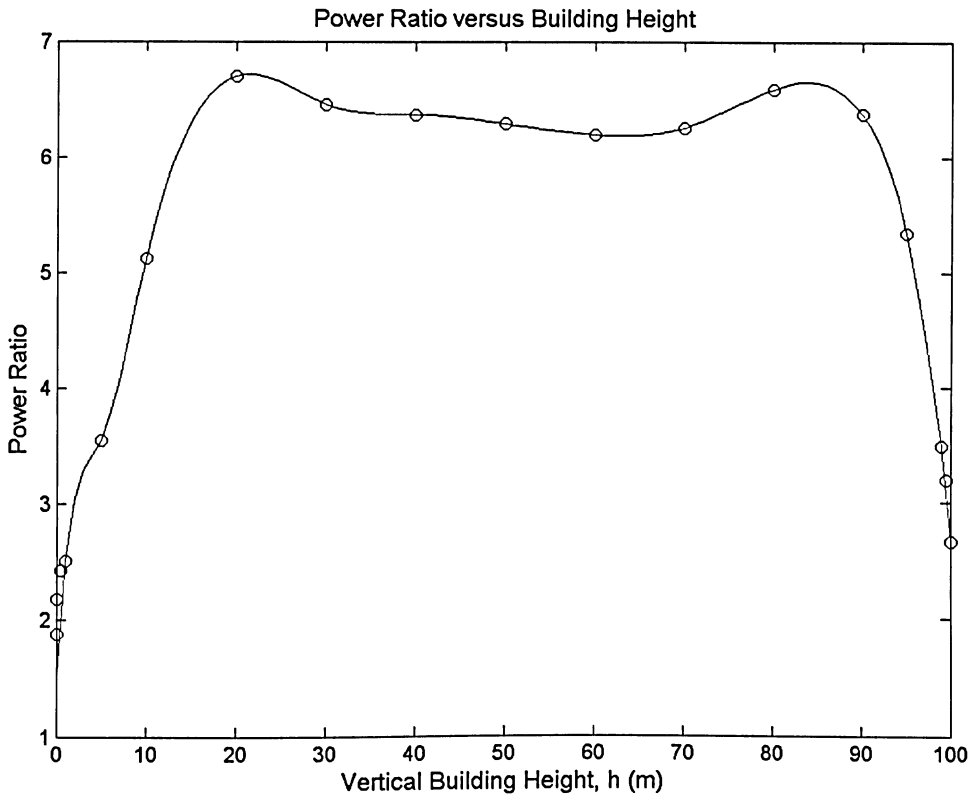


Figure 5.26: Power Ratio as a function of Building height $50^o$ for $b_x/D_o = 20/20$, $g/D_o = 3/20$, $a/D_o = 15/20$, $h/D_o = 100/20$ and $D_o = 20m$

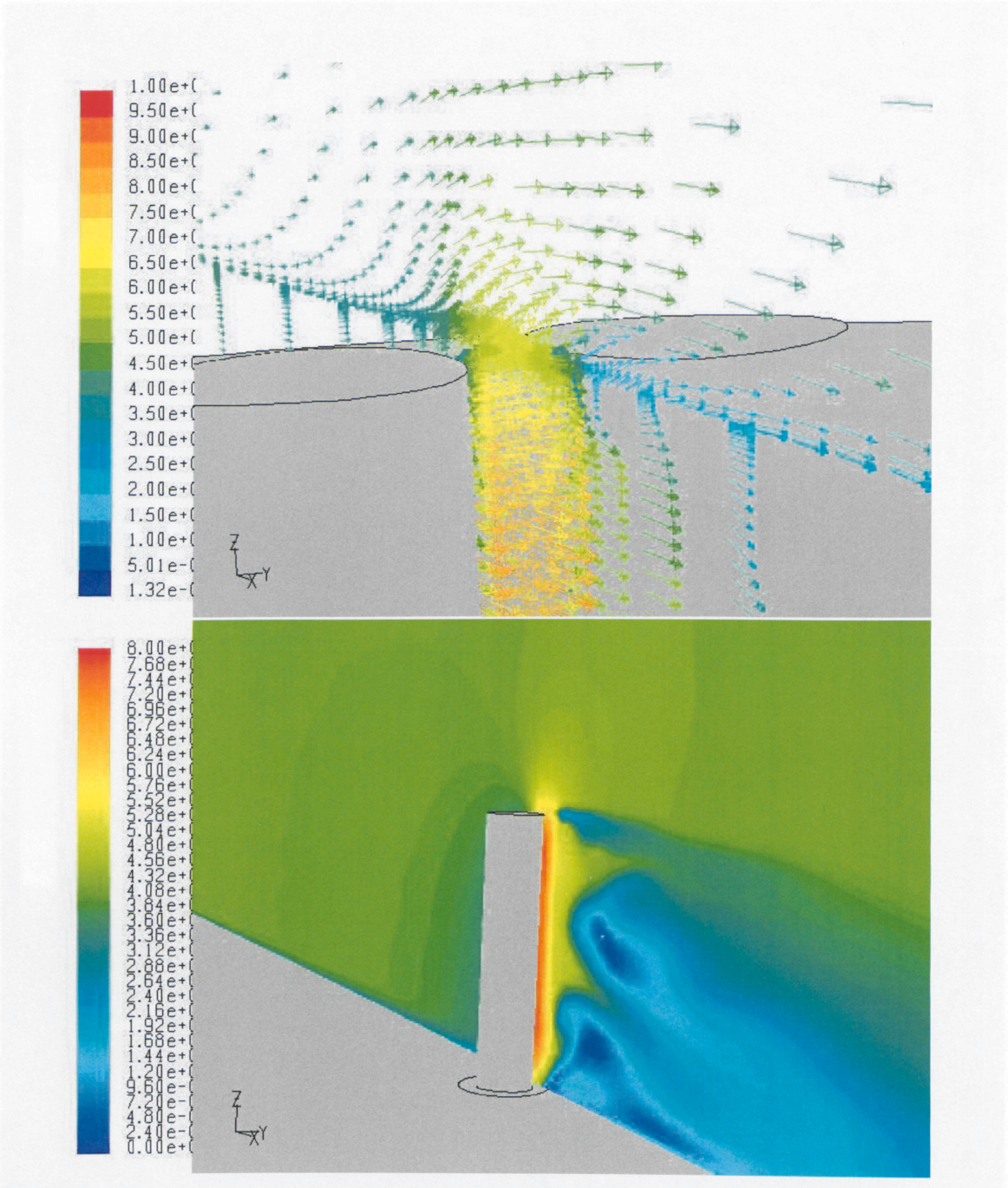


Figure 5.27: 3D Vector Plot at Roof top (Top) Velocity Magnitude Plot (Bottom) for $50^o$ for $b_x/D_o = 20/20$, $g/D_o = 3/20$, $a/D_o = 15/20$, $h/D_o = 100/20$, $D_o = 20m$ at $0^o$ angle of incidence at time=730s

# Chapter 6

# Conclusion

The conclusions from this study are:

1. The results from the oblateness parameter $a$ showed increasing the value increased the PR at low angles of incidence and decreased PR at high angles of incidence. However, if the thickness parameter $b_x$ was increased beyond $b_x/D_o = 30/20$ the trend reverses and the $PR$ increased at high angles of incidence and decreased at low angles of incidence.

2. Using a high value of oblateness $a/D_o = 15/20$, it was shown that, that increasing the thickness parameter $b_x/D_o \geq 20/20$, the $PR$ decreased for all angles of attack. However, increasing the thickness also made the geometry more streamlined, which reduced the variance of velocity in the gap.

3. Increasing the gap parameter $g/D_o$ decreased the $PR$ since the pressure gradient in the gap was reduced, indicating smaller gap sizes produce a higher flow density. However, as the gap size decreased, the variance of velocity in the gap region increased and became more random, due to the flip-flopping of the wake.

4. Varying the velocity had little effect on the power ratio, indicating the solution is

independent of velocity over the range of velocities explored. Therefore, the benefits of using building augmented wind turbines are seen through a wide range of wind speeds.

5. The 3D results showed that the shedding vortices dampened out due to 3D vortex interactions resulting in a higher $PR$ when compared to the 2D results .

6. For high variation in incident angles, the best configuration found was large thickness ($b_x/D_o = 40/20$), a small oblateness ($a/D_o = 5/20$) with a relatively small gap ($g/D_o = 3/20$). For low variation in incident angles, the best configuration found was a moderate thickness ($b_x/D_o = 20/20$), a relatively high oblateness ($a/D_o = 15/20$) with a relatively small gap ($g/D_o = 3/20$).

7. Turbines can operate at low speeds of 2 $m/s$ making turbine power production feasible where thought not to be.

Recommendations:

1. Trade off of gap size and wind turbine sweeping area

2. Capping roof geometry, conjoining the buildings to reduce flow loss

3. Roof geometry (using smooth edges)

4. Cowling around the wind turbines

5. The behavior of power ratio using unsteady free stream velocity

6. The effects of urban wind profiles on power ratio in 3D

# Bibliography


[1] The European Wind Energy Association, Wind Power Installed in Europe by End of 2005 (Cumulative), EWEA, www.ewea.org, 2005.

[2] Global Wind Energy Council, Global Wind 2005 Report, Brussels, Belguim, 2005.

[3] Goodstein, D., Energy, Technology and Climate: Running Out of Gas, Out of Gas, New Dimensions in Bioethics, Yale University Press, 2004.

[4] Campbell, N., Stankovic, S., Graham, M., Parkin, P., Van Duijvendijk, M., de Gruiter, T., Behling, S., Hieber, J., Blanch, M., Wind Energy for the Built Enviroment (Project WEB), Procs. European Wind Energy Conference & Exhibition, Copenhagen, 2-6, July 2001.

[5] Grant, A and Kelly, N., The development of a Ducted Wind Turbine Simulation Model, Eight International IBPSA Conference, Eindhoven, Netherlands, August 11-14, 2003.

[6] Igra, O., Shrouds for Aerogenerators, , AIAA paper 76-181, Washington, D.C. 1976.

[7] Kogan, A. and Nissim, Shrouded Aerogenerator Design Study, Two Dimensional Shroud Performance. Bulletin of the Research Council of Israel, Vol 11c, 1962, pp. 67-88.

[8] Kogan, A. and Seginar, Final Report on Shroud Design, Dept. of Aeronautical Engineering, Technion, T.A.E. Rept. No. 32A, 1963.

[9] Betz, A., 1920, Das Maximum der theoretisch moglichen Ausnutzung des Windes durch Windmotoren, Z. Gesamte Turbinewesen, 26.

[10] Gorban, Alexander N., Gorlov, Alexander M., Silantyev, Valentin M., Limits of the Turbine Efficiency for Free Fluid Flow, Journal of Energy Resource Technology, ASME, Vol. 123, pg311-317, December 2001.

[11] Eldridge, Frank R. Wind Machines: Second Edition, Van Nostrand Reinhold Company, New York, 1980.

[12] Burton, T., Sharpe, D., Jenkins, N., Bossanyi, E. Wind Energy Hand Book, John Wiley and Sons, Ltd, West Sussex, England, Novemeber 2002.

[13] Hills, R. Power from Wind: A History of Windmill Technology, CAmbridge University Press, September 1996.

[14] Webster G W., 1979, Devices for utilizing the power of wind, USA Patent No. 4154556.

[15] Fletcher, H.S., Experimental Investigation of Lift, Drag and Pitching Moment of Five Annular Airfoils, NASA TN 4117, 1957.

[16] Wind Energy in Urban Areas, Refocus, March/April 2002 of cylinder, Ann. Rev. Fluid Mech., 25, 1993, 99-114.

[17] Martin O.L.Hansen: Aerodynamics of Wind Turbines, Rotors, Loads and Structure, James & James Ltd., London 2000, ISBN 1-902916-06-9.

[18] Bearman, P.W. and Wadcock A.J. The interaction between a pair of circular cylinders normal to a stream, Fluid Mechanics, 61, 499, 1973.

[19] H.J. Kim and P.A. Durbin. Investigation of the flow between a pair of circular cylinders in the Floppy Regime. Lewis Research Center, Cleveland, OH, 44135, USA, 1988.

[20] Paracschivoiu, I., Wind Turbine Design: With Emphasis on Darrieus Concept, Ecole Polytechnique de Montreal, 2002.

[21] Bruce Wind Turbine, Ontario Power Generation Inc., www.opg.com, 2001.

[22] White, F., M. Fluid Mechanics Fifth Edition, McGraw-Hill Companies, New York, NY, 2003.

[23] Schetz, J.A., Boundary Layer Analysis, Prentice-Hall Inc., Upper Saddle, NJ, 1993.

[24] T. J. Barth and D. Jespersen. The design and application of upwind schemes on unstructured meshes. Technical Report AIAA-89-0366, AIAA 27th Aerospace Sciences Meeting, Reno, Nevada, 1989.

[25] P. Spalart and S. Allmaras. A one-equation turbulence model for aerodynamic flows. Technical Report AIAA-92-0439, American Institute of Aeronautics and Astronautics, 1992.

[26] Sutherland, W., The viscosity of gases and molecular force. Philosophical Magazine, S.5, 36 (1893), 507-531.

[27] FLUENT 6.1 Documentation: User's Guide, Fluent Inc., 2003.

[28] Kang, Sangmo, Characteristics of Flow over two circular cylinders in a side-by-side arrangement at low Reynolds number, Physics of Fluids, Volume 15, Number9, September 2003.

[29] Shih, W. C. L., Wang, C., Coles, D., Roshko, A. Experiments on flow past rough circular cylinders at large Reynolds numbers, J. Wind Engg and Industrial Aerodynamics, 49, 251-361.

[30] Wang, M., Catalano, P., Laccarino, G., Prediction of high Reynolds number flow over a circular cylinder using LES with wall modeling.

# Appendix A

# Appendix: Derived Quantities

## A.1 RANS Derivations

### A.1.1 Time average of variables

The mean of a variable is defined as,

$$F = \frac{1}{t - t_o} \int_{to}^{t} f(t)dt \tag{A.1}$$

By definition,

$$\bar{f} = \frac{1}{t - t_0} \int_{to}^{t} f(t)dt \tag{A.2}$$

which leads to,

$$\begin{aligned} \bar{f}' = 0, \quad \bar{F} = F, \quad \bar{f} = F \\ \overline{f+g} = F + G, \quad \overline{F \cdot g} = FG, \quad \int \bar{f} ds = \int F ds \\ \overline{F \cdot g'} = 0, \quad \overline{\frac{\partial f}{\partial x}} = \frac{\partial F}{\partial x} \end{aligned}$$

where $g = G + g'$ is just some other property.

### A.1.2 Continuity Equation

Starting with the continuity equation:

$$\frac{\partial \rho}{\partial t} + \frac{\partial (\rho u_i)}{\partial x_i} = 0 \tag{A.3}$$

Assuming a steady flow $\partial/\partial x_i = 0$ and density fluctuations are small, the continuity equation becomes:

$$\frac{\partial(u_i)}{\partial x_i} = 0 \tag{A.4}$$

Substituting in,

$$u_i = \bar{u}_i + u_i' \tag{A.5}$$

to yield,

$$\frac{\partial(\bar{u}_i + u_i')}{\partial x_i} = 0 \tag{A.6}$$

expanding out:

$$\frac{\partial(\bar{u}_i)}{\partial x_i} + \frac{\partial(u_i')}{\partial x_i} = 0 \tag{A.7}$$

Time averaging both sides of the equation yields:

$$\int_0^t \frac{\partial(\overline{u}_i)}{\partial x_i} + \int_0^t \frac{\partial(u_i')}{\partial x_i} = \overline{\frac{\partial(\overline{u}_i)}{\partial x_i}} + \overline{\frac{\partial(u_i')}{\partial x_i}} = 0 \tag{A.8}$$

The time average of the fluctuating terms goes to zero over a sufficiently long time since the fluctuating will be completely random. Therefore, the continuity equation becomes,

$$\frac{\partial(\overline{u}_i)}{\partial x_i} = 0 \tag{A.9}$$

This is identical to the original definition. So we can conclude the fluctuating velocity components didn't effect the continuity, as expected.

### A.1.3 Momentum Equation

The steady Momentum equations from the Navier-Stokes equations are defined as,

$$\rho u_i \frac{\partial u_j}{\partial x_i} = -\frac{\partial p}{\partial x_j} + \frac{\partial}{\partial x_i}\left[\mu\left(\frac{\partial u_i}{\partial x_j} + \frac{\partial u_j}{\partial x_i}\right)\right] \tag{A.10}$$

where, $j = 1, 2, 3$ which corresponds to $x_1 = x$, $x_2 = y$, $x_3 = z$. We will start the derivation with the convective terms in the momentum equation,

$$\rho u_i \frac{\partial u_j}{\partial x_i} \tag{A.11}$$

substituting in the mean and fluctuating components,

$$\rho(\overline{u}_i + u_i')\frac{\partial(\overline{u}_j + u_j')}{\partial x_i} = \rho(\overline{u}_i)\frac{\partial(\overline{u}_j)}{\partial x_i} + \rho(u_i')\frac{\partial(\overline{u}_j)}{\partial x_i} + \rho(\overline{u}_i)\frac{\partial(u_j')}{\partial x_i} + \rho(u_i')\frac{\partial(u_j')}{\partial x_i} \tag{A.12}$$

and taking the time average yields:

$$\overline{\rho(\overline{u}_i)\frac{\partial(\overline{u}_j)}{\partial x_i}} + \overline{\rho(u_i')\frac{\partial(u_j')}{\partial x_i}} \tag{A.13}$$

Note that we have an extra turbulence term when compared to the original convective terms. We can further simplify this by first multiplying the continuity equation by $u_j$ so:

$$u_j\frac{\partial u_i}{\partial x_i} = 0 \tag{A.14}$$

now substituting in the fluctuating velocity expressions,

$$(\overline{u_j} + u_j')\frac{\partial(\overline{u}_i + u_i')}{\partial x_i} = 0 \tag{A.15}$$

expanding through,

$$(\overline{u_j})\frac{\partial(\overline{u}_i)}{\partial x_i} + (u_j')\frac{\partial(\overline{u}_i)}{\partial x_i} + (\overline{u_j})\frac{\partial(u_i')}{\partial x_i} + (u_j')\frac{\partial(u_i')}{\partial x_i} = 0 \tag{A.16}$$

and time averaging the equation yields:

$$\overline{(\overline{u_j})\frac{\partial(\overline{u}_i)}{\partial x_i}} + \overline{(u_j')\frac{\partial(u_i')}{\partial x_i}} = 0 \tag{A.17}$$

But $\partial\overline{u_i}/\partial x_i = 0$ is the continuity equation, so the above equation reduces to:

$$\overline{u_j'}\frac{\partial(\overline{u}_i')}{\partial x_i} = 0 \tag{A.18}$$

However, by using the product rule,

$$\frac{\partial(a(x)b(x))}{\partial x} = b(x)\frac{\partial a(x)}{\partial x} + a(x)\frac{\partial b(x)}{\partial x} \tag{A.19}$$

or:

$$\frac{\partial(a(x)b(x))}{\partial x} - a(x)\frac{\partial b(x)}{\partial x} = b(x)\frac{\partial a(x)}{\partial x} \tag{A.20}$$

The turbulence term in equation (1) can be expressed as,

$$(\overline{u}_i')\frac{\partial(\overline{u}_j')}{\partial x_i} = \frac{\partial(\overline{u_j'u_i'})}{\partial x_i} - \overline{u}_j'\frac{\partial\overline{u}_i'}{\partial x_i} \tag{A.21}$$

where, the last term in the above equation we just proved to be zero through the manipulated continuity equation. The convective terms can now be simply expressed as,

$$\rho u_i \frac{\partial u_j}{\partial x_i} + \frac{\partial(\rho \overline{u_j' u_i'})}{\partial x_i} \tag{A.22}$$

0The remaining terms left in the momentum equation have a similar solution to the continuity equation (linear terms) which results in no added turbulence terms. Therefore, the entire the *RANS* equation is,

$$\rho \frac{\partial u_j}{\partial t} + \rho u_i \frac{\partial u_j}{\partial x_i} = -\frac{\partial p}{\partial x_j} + \frac{\partial}{\partial x_i}\left[\mu\left(\frac{\partial u_i}{\partial x_j} + \frac{\partial u_j}{\partial x_i}\right)\right] + \frac{\partial(-\rho \overline{u_j' u_i'})}{\partial x_i} \tag{A.23}$$

## A.2 Mean and Variance

### A.2.1 Mean

The mean of a data spread is calculated using,

$$\bar{X} = \frac{\sum X}{N} \tag{A.24}$$

where $X$ is the data point and $N$ is the number of data points.

### A.2.2 Variance

To calculate the variance $S^2$ of a data spread,

$$S^2 = \frac{\sum (X - \bar{X})^2}{N - 1} \tag{A.25}$$

# Appendix B

# Appendix: Additional Plots

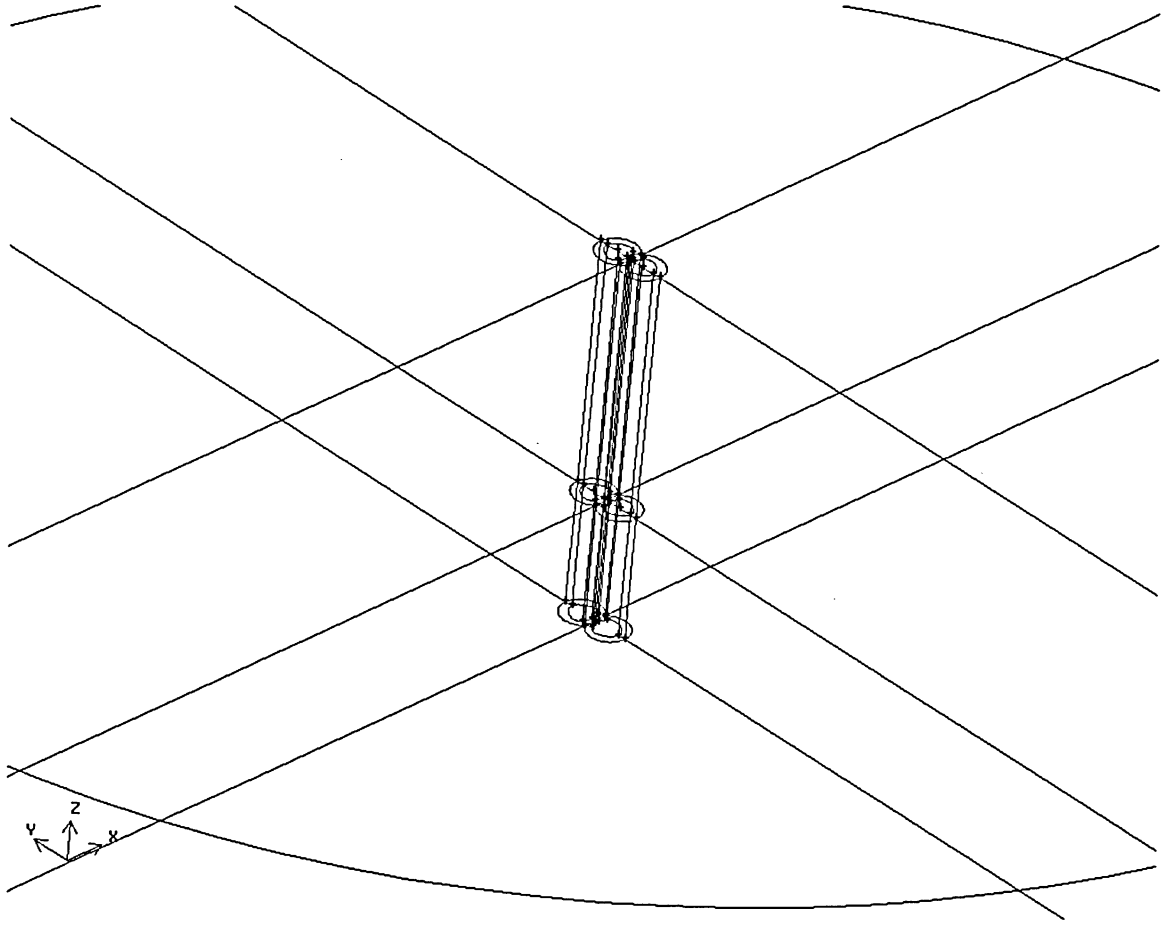


Figure B.1: Isometric View of 3D grid schematic $b_x/D_o = 20/20$, $g/D_o = 3/20$, $a/D_o = 15/20$ and $D_o = 20m$

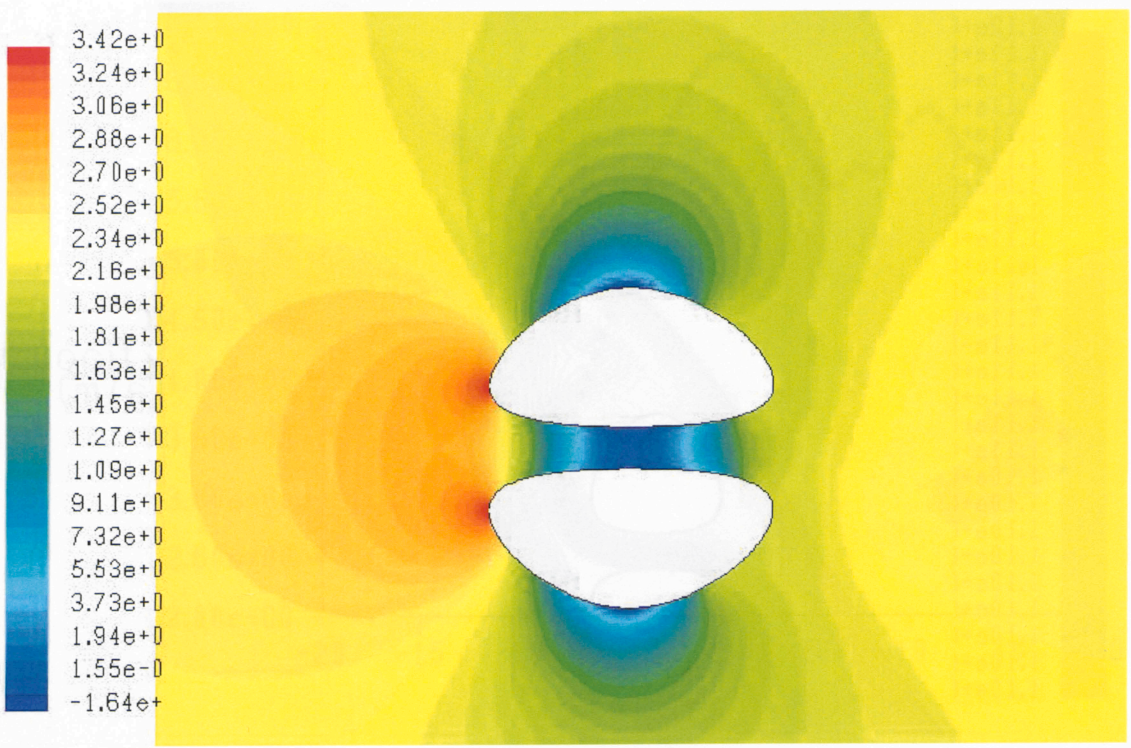


Figure B.2: Snap shot of static pressure for $b_x/D_o = 40/20$, $a/D_o = 15/20$, $g = 3/20$ at angle of incidence of $0^o$

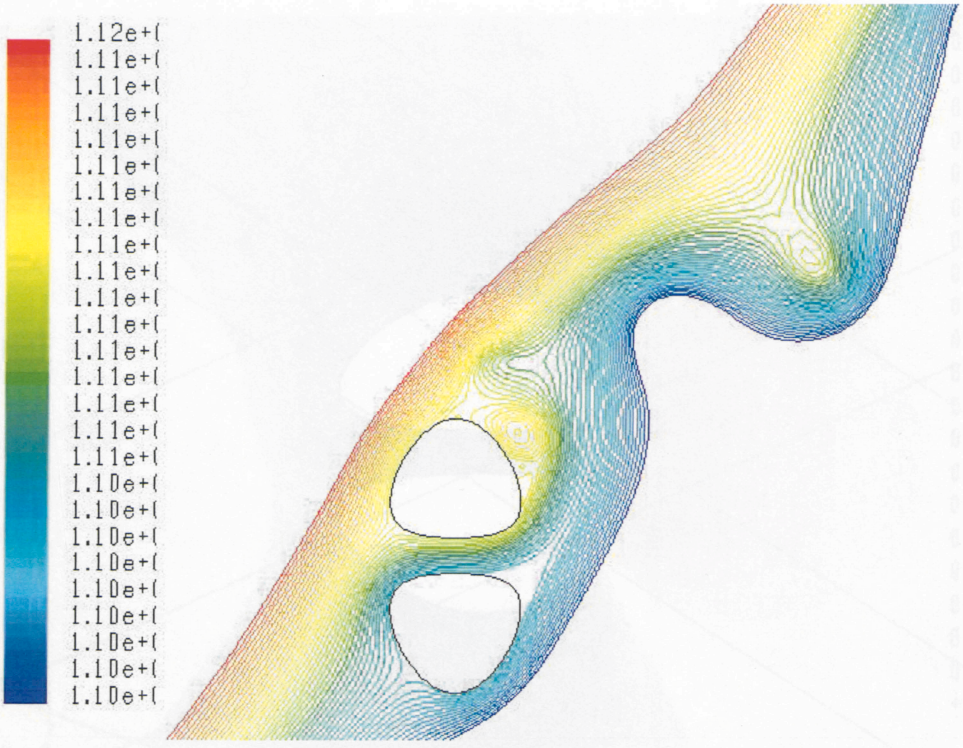


Figure B.3: Snap shot of $b_x/D_o = 20/20$, $a/D_o = 17/20$, $g/D_o = 3/20$ at angle of incidence of $50^o$

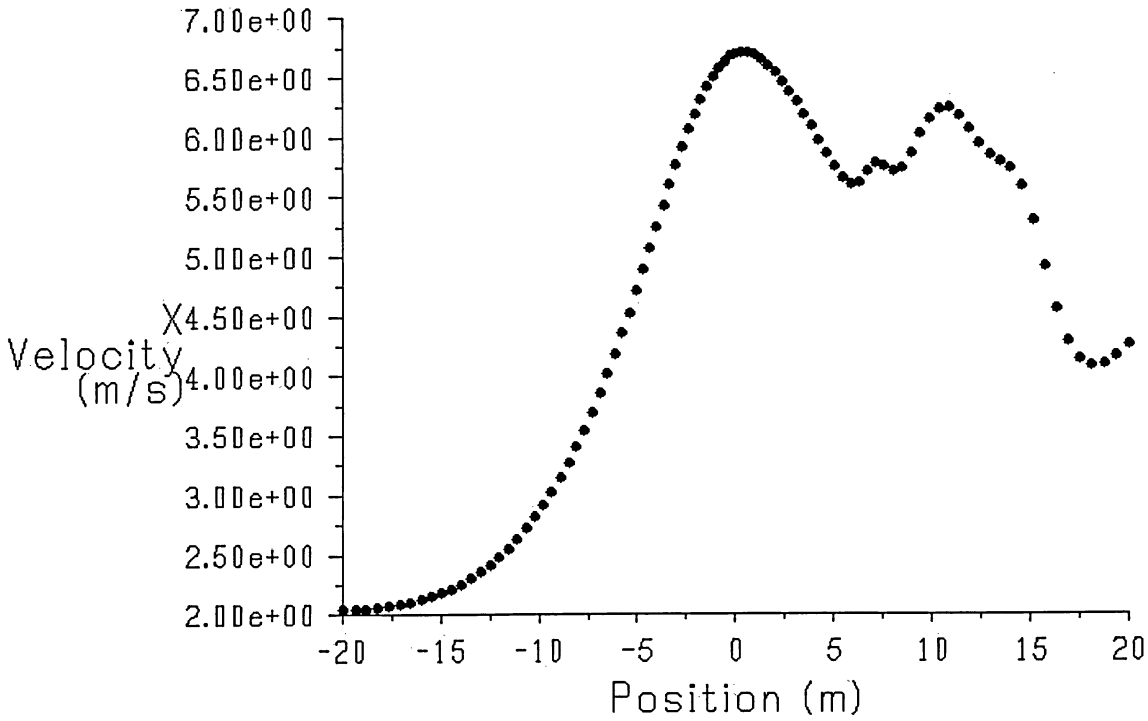


Figure B.4: Velocity Profile along vector $x = 1, y = 0$ for $b_x/D_o = 20/20$, $a/D_o = 10/20$, $g/D_o = 3/20$ at angle of incidence of $50^o$

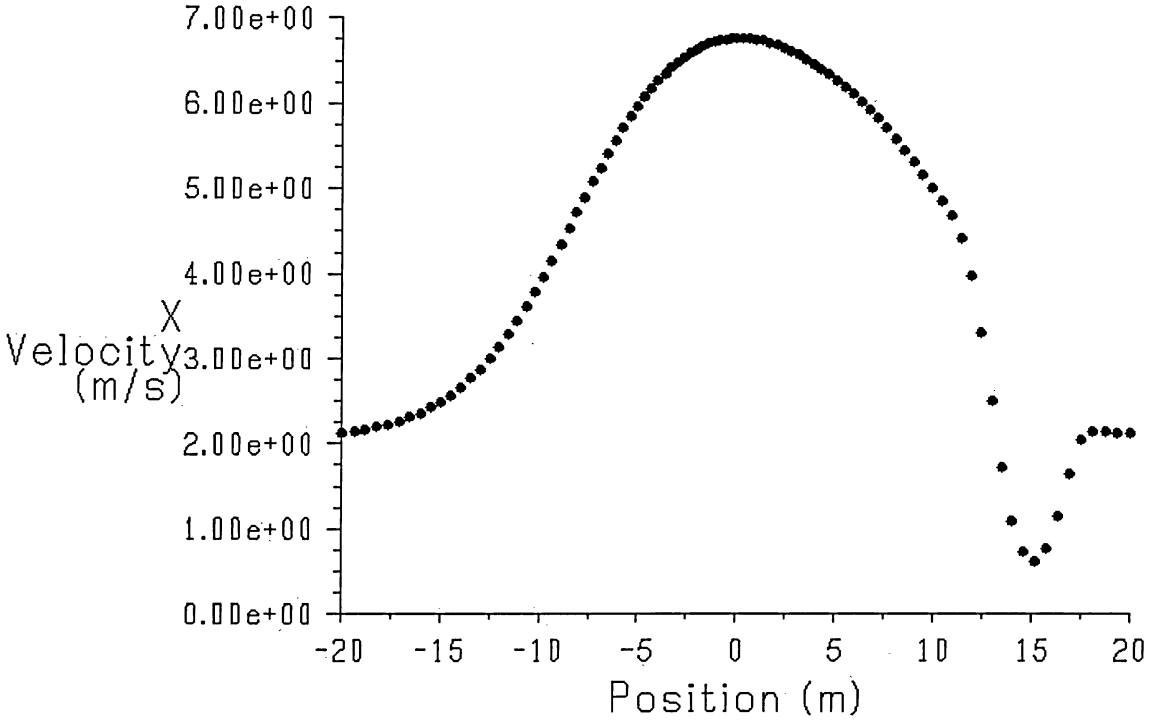


Figure B.5: Velocity Profile along vector $x = 1, y = 0$ for $b_x/D_o = 20/20$, $a/D_o = 17/20$, $g/D_o = 3/20$ at angle of incidence of $50^o$

# Appendix C

# Appendix: Additional Tables

Table C.1: Node Density Break down see Figure 2.3

| Line | Norm | Med | Fine | X-fine |
|---|---|---|---|---|
| a-b | 12 | 25 | 25 | 25 |
| b-c | 6 | 10 | 16 | 16 |
| c-d | 38 | 63 | 100 | 100 |
| d-e | 7 | 8 | 18 | 18 |
| e-f | 1 | 1 | 2 | 2 |
| f-g | 200 | 300 | 500 | 700 |
| g-h | 42 | 44 | 50 | 57 |
| h-i | 100 | 160 | 300 | 500 |
| a-g | 100 | 140 | 210 | 220 |
| i-j | 77 | 102 | 150 | 197 |
| j-e | 200 | 300 | 500 | 700 |
| j-c | 34 | 50 | 80 | 80 |

# Appendix D

# Appendix: Fluent Settings and Scripts

## D.1 Fluent Sample Input File

```
[\sourcetabsize]
rc bx20a15g3.cas
/define/boundary-conditions/zone-type
a_2
porous-jump
/define/boundary-conditions/porous-jump
a_2
1e+10
1
0.4
/define/boundary-conditions/velocity-inlet
velocity_inlet.1
no
yes
yes
no
3.909121302469378877665094593670 9
no
1.422803796234781929463454397078 2
no
300
no
no
yes
no
10
/solve/init/init
/solve/set/time-step 0.1
/solve/dual-time-iterate 7300 20
wd data_1.dat
exit
yes
```

## D.2 Summary of Fluent Settings

```
[\sourcetabsize]

FLUENT Version: 2d, segregated, S-A, unsteady (2d, segregated,
Spalart-Allmaras, unsteady) Release: 6.1.22 Title:

Models
------

   Model                        Settings
   ---------------------------------------------------------------
   Space                        2D
   Time                         Unsteady, 2nd-Order Implicit
   Viscous                      Spalart-Allmaras turbulence model
   Production Option            Strain/Vorticity
   Heat Transfer                Enabled
   Solidification and Melting   Disabled
   Radiation                    None
   Species Transport            Disabled
   Coupled Dispersed Phase      Disabled
   Pollutants                   Disabled
   Soot                         Disabled

Boundary Conditions
-------------------

   Zones

      name               id   type
      ---------------------------------------
      fluid              2    fluid
      wall               3    wall
      a_2                4    interior
      symmetry           5    interior
      velocity_inlet.1   6    velocity-inlet
      default-interior   8    interior

   Boundary Conditions

      fluid

         Condition                                                  Value
         ---------------------------------------------------------------
         Material Name                                              air
         Specify source terms?                                      no
         Source Terms                                               ()
         Specify fixed values?                                      no
         Fixed Values                                               ()
         Motion Type                                                0
         X-Velocity Of Zone                                         0
         Y-Velocity Of Zone                                         0
         Rotation speed                                             0
         X-Origin of Rotation-Axis                                  0
         Y-Origin of Rotation-Axis                                  0
         Deactivated Thread                                         no
         Laminar zone?                                              no
         Set Turbulent Viscosity to zero within laminar zone?       yes
         Porous zone?                                               no
         X-Component of Direction-1 Vector                          1
         Y-Component of Direction-1 Vector                          0
         Direction-1 Viscous Resistance                             0
```

| | |
|---|---|
| Direction-2 Viscous Resistance | 0 |
| Direction-1 Inertial Resistance | 0 |
| Direction-2 Inertial Resistance | 0 |
| C0 Coefficient for Power-Law | 0 |
| C1 Coefficient for Power-Law | 0 |
| Porosity | 1 |
| Solid Material Name | aluminum |

wall

| Condition | Value |
|---|---|
| Wall Thickness | 0 |
| Heat Generation Rate | 0 |
| Material Name | aluminum |
| Thermal BC Type | 1 |
| Temperature | 300 |
| Heat Flux | 0 |
| Convective Heat Transfer Coefficient | 0 |
| Free Stream Temperature | 300 |
| Wall Motion | 0 |
| Shear Boundary Condition | 0 |
| Define wall motion relative to adjacent cell zone? | yes |
| Apply a rotational velocity to this wall? | no |
| Velocity Magnitude | 0 |
| X-Component of Wall Translation | 1 |
| Y-Component of Wall Translation | 0 |
| Define wall velocity components? | no |
| X-Component of Wall Translation | 0 |
| Y-Component of Wall Translation | 0 |
| External Emissivity | 1 |
| External Radiation Temperature | 300 |
| Wall Roughness Height | 0 |
| Wall Roughness Constant | 0.5 |
| Rotation Speed | 0 |
| X-Position of Rotation-Axis Origin | 0 |
| Y-Position of Rotation-Axis Origin | 0 |
| X-component of shear stress | 0 |
| Y-component of shear stress | 0 |
| Surface tension gradient | 0 |

a_2

| Condition | Value |
|---|---|

symmetry

| Condition | Value |
|---|---|

velocity_inlet.1

| Condition | Value |
|---|---|
| Velocity Specification Method | 1 |
| Reference Frame | 0 |
| Velocity Magnitude | 0 |
| X-Velocity | 4.1599998 |
| Y-Velocity | 0 |
| X-Component of Flow Direction | 1 |
| Y-Component of Flow Direction | 0 |

| | |
|---|---|
| X-Component of Axis Direction | 1 |
| Y-Component of Axis Direction | 0 |
| Z-Component of Axis Direction | 0 |
| X-Coordinate of Axis Origin | 0 |
| Y-Coordinate of Axis Origin | 0 |
| Z-Coordinate of Axis Origin | 0 |
| Angular velocity | 0 |
| Temperature | 300 |
| Turbulence Specification Method | 2 |
| Modified Turbulent Viscosity | 0.001 |
| Turbulence Intensity | 0.1 |
| Turbulence Length Scale | 1 |
| Hydraulic Diameter | 1 |
| Turbulent Viscosity Ratio | 10 |
| is zone used in mixing-plane model? | no |

default-interior

| Condition | Value |
|---|---|

Solver Controls

Equations

| Equation | Solved |
|---|---|
| Flow | yes |
| Modified Turbulent Viscosity | yes |
| Energy | yes |

Numerics

| Numeric | Enabled |
|---|---|
| Absolute Velocity Formulation | yes |

Unsteady Calculation Parameters

| | |
|---|---|
| Time Step (s) | 1 |
| Max. Iterations Per Time Step | 20 |

Relaxation

| Variable | Relaxation Factor |
|---|---|
| Pressure | 0.30000001 |
| Density | 1 |
| Body Forces | 1 |
| Momentum | 0.69999999 |
| Modified Turbulent Viscosity | 0.80000001 |
| Turbulent Viscosity | 1 |
| Energy | 1 |

Linear Solver

| Variable | Solver Type | Termination Criterion | Residual Reduction Tolerance |
|---|---|---|---|

| | | | |
|---|---|---|---|
| Pressure | V-Cycle | 0.1 | |
| X-Momentum | Flexible | 0.1 | 0.7 |
| Y-Momentum | Flexible | 0.1 | 0.7 |
| Modified Turbulent Viscosity | Flexible | 0.1 | 0.7 |
| Energy | Flexible | 0.1 | 0.7 |

Discretization Scheme

| Variable | Scheme |
|---|---|
| Pressure | Standard |
| Pressure-Velocity Coupling | SIMPLE |
| Momentum | Second Order Upwind |
| Modified Turbulent Viscosity | Second Order Upwind |
| Energy | Second Order Upwind |

Solution Limits

| Quantity | Limit |
|---|---|
| Minimum Absolute Pressure | 1 |
| Maximum Absolute Pressure | 5000000 |
| Minimum Temperature | 1 |
| Maximum Temperature | 5000 |
| Maximum Turb. Viscosity Ratio | 100000 |

## Material Properties

Material: aluminum (solid)

| Property | Units | Method | Value(s) |
|---|---|---|---|
| Density | kg/m3 | constant | 2719 |
| Cp (Specific Heat) | j/kg-k | constant | 871 |
| Thermal Conductivity | w/m-k | constant | 202.4 |

Material: air (fluid)

| Property | Units | Method | Value(s) |
|---|---|---|---|
| Density | kg/m3 | constant | 1.225 |
| Cp (Specific Heat) | j/kg-k | constant | 1006.43 |
| Thermal Conductivity | w/m-k | constant | 0.0242 |
| Viscosity | kg/m-s | sutherland | (1.716e-05 273.10999 110.56 ) |
| Molecular Weight | kg/kgmol | constant | 28.966 |
| L-J Characteristic Length | angstrom | constant | 3.711 |
| L-J Energy Parameter | k | constant | 78.6 |
| Thermal Expansion Coefficient | 1/k | constant | 0 |
| Degrees of Freedom | | constant | 0 |

# Appendix E

# Appendix: Matlab Scripts

## E.1 Richardsons Extrapolation

```
%
clear all clc
%...Collecting Data.....................................
 D1(1,:,:)=load('\Time Step Analysis\dt0001\monitor-1.txt');
  D2(1,:,:)=load('\Time Step Analysis\dt001\monitor-1.txt');
  D3(1,:,:)=load('\No Porous Simulations\bx20a15\bx20a15_aoa0\monitor-1.txt');
  D4(1,:,:)=load('\Time Step Analysis\dt1\monitor-1.txt');
  D5(1,:,:)=load('\Time Step Analysis\dt10\monitor-1.txt');

   E(1,1:5)=[log10(0.001) log10(0.01) log10(0.1) log10(1) log10(10)]; %angle of attack
  E(2,1)=20; % bx value
  E(3,1)=15;  % a
  E(4,1)=6; % gap size
  V_in3=4.16;
  E(5,1)=mean(D1(1,:,2)); % mean
  E(6,1)=var(D1(1,:,2)); %variance
  E(7,1)=(mean(D1(1,:,2)))^3/V_in3^3; % power ratio
  E(5,2)=mean(D2(1,:,2)); % mean
  E(6,2)=var(D2(1,:,2)); %variance
  E(7,2)=(mean(D2(1,:,2)))^3/V_in3^3; % power ratio
  E(5,3)=mean(D3(1,:,2)); % mean
  E(6,3)=var(D3(1,:,2)); %variance
  E(7,3)=(mean(D3(1,:,2)))^3/V_in3^3; % power ratio
  E(5,4)=mean(D4(1,:,2)); % mean
  E(6,4)=var(D4(1,:,2)); %variance
  E(7,4)=(mean(D4(1,:,2)))^3/V_in3^3; % power ratio
  E(5,5)=mean(D5(1,:,2)); % mean
  E(6,5)=var(D5(1,:,2)); %variance
  E(7,5)=(mean(D5(1,:,2)))^3/V_in3^3; % power ratio
%%%%%%%%%%%%%%%%%%%%%%%%%%%%%%%%%%%%%%%%%%%%%%%%%%%%%%%%%%%%%%%%%%%%%%%%%%%%%%%
%...Richerdson's Extrap.....................................%
%%%%%%%%%%%%%%%%%%%%%%%%%%%%%%%%%%%%%%%%%%%%%%%%%%%%%%%%%%%%%%%%%%%%%%%%%%%%%%%
%fine grid
h1 = 0.001; %Grid size
M1 = E(7,1); %Respective Mass Flow rate
%intermediate grid
h2 = 0.01; %Grid Size
M2 = E(7,2); %Respective Mass Flow rate
%coarse grid
```

```
h3 = 0.1; %Grid Size
M3 = E(7,3); %%Respective Mass Flow rate
r21 = h2/h1 %Grid Refinement Factor 1
r32 = h3/h2 %Grid Refinement Factor 2
s = sign((M3-M2)/(M2-M1)) %Sign of Ratio
p=1; %Order Initialization
resid =1 %Residual Initialization
while abs(resid) > 0.000001 %Iterative Loop for calculate order
p=p-0.000001; q = log(((r21^p)-s)/((r32^p)-s)); resid = p -
(abs(log(abs((M3-M2)/(M2-M1)))+q))/log(r21); end
M_fine = ((r21^p)*M1-M2)/(r21^p-1) %Calculating Extrapolated Value
%%%%%%%%%%%%%%%%%%%%%%%%%%%%%%%%%%%%%%%%%%%%%%%%%%%%
%...Ploting.....................................%
%%%%%%%%%%%%%%%%%%%%%%%%%%%%%%%%%%%%%%%%%%%%%%%%%%%%
    subplot(2,1,1)
    hold on
    A(1:5)=E(1,1:5);
    B(1:5)=E(7,1:5);
    plot(A,B, '--o');
    plot([-5 1], [M_fine M_fine], '-.g')
    hx=xlabel('Time StepX10^x')
    h_text = findobj(hx,'type','text');
    set(h_text,'FontUnits','points','FontSize',12)
    hy=ylabel('Power Ratio')
    h_text = findobj(hy,'type','text');
    set(h_text,'FontUnits','points','FontSize',12)
    htitle=title(['Velocity/Reynolds Number Dependence'])
    h_text = findobj(htitle,'type','text');
    set(h_text,'FontUnits','points','FontSize',12)
    hold off
    subplot(2,1,2)
    hold on
    A(1:5)=E(1,1:5);
    B(1:5)= E(6,1:5);
    plot(A,B, '--o');
    hx=xlabel('Time Step X10^x')
    h_text = findobj(hx,'type','text');
    set(h_text,'FontUnits','points','FontSize',12)
    hy=ylabel('Variance of Velocity')
    h_text = findobj(hy,'type','text');
    set(h_text,'FontUnits','points','FontSize',12)
    %h_legend=legend(['V_o=' num2str(V_in)], ['V_o=' num2str(V_in2)], ['V_o=' num2str(V_in3)],-1)
    hold off
    print -djpeg100 TimeStudy.jpg
%%%%%%%%%%%%%%%%%%%%%%%%%%%%%%%%%%%%%%%%%%%%%%%%%%%%
% Calc error Mean at every time step              %
%%%%%%%%%%%%%%%%%%%%%%%%%%%%%%%%%%%%%%%%%%%%%%%%%%%%
     e1=(mean(D1(1,1:700,2)))^3/V_in3^3;
     e2=(mean(D1(1,1:600,2)))^3/V_in3^3;
     (e1-e2)/e2*100
     e1=(mean(D2(1,1:700,2)))^3/V_in3^3;
     e2=(mean(D2(1,1:600,2)))^3/V_in3^3;
     (e1-e2)/e2*100
     e1=(mean(D3(1,1:700,2)))^3/V_in3^3;
     e2=(mean(D3(1,1:600,2)))^3/V_in3^3;
     (e1-e2)/e2*100
     e1=(mean(D4(1,1:700,2)))^3/V_in3^3;
     e2=(mean(D4(1,1:600,2)))^3/V_in3^3;
     (e1-e2)/e2*100
```

## E.2 Calculating Steady State Mean

```
%
clear Dmean x r=length(D1(1,:,2)) count=100; t=0.001 for
i=count:count:r
    Dmean(i/count)=mean(D1(1,1:i,2));
    x(i/count)=D1(1,i,1);
    if i>count
        error(i/count)=(Dmean((i-count)/count)-Dmean(i/count))/Dmean((i-count)/count);
        xerror(i/count)=D1(1,i,1);
    end
end

r=length(D2(1,:,2)) count=10; t=0.01 for i=count:count:r
    Dmean2(i/count)=mean(D2(1,1:i,2));
    x2(i/count)=D2(1,i,1);
     if i>count
        error2(i/count)=(Dmean2((i-count)/count)-Dmean2(i/count))/Dmean2((i-count)/count);
        xerror2(i/count)=D2(1,i,1);
    end
end r=length(D3(1,:,2)) count=1; for i=count:count:r
    Dmean3(i/count)=mean(D3(1,1:i,2));
    x3(i/count)=D3(1,i,1);
    if i>count
        error3(i/count)=(Dmean3((i-count)/count)-Dmean3(i/count))/Dmean3((i-count)/count);
        xerror3(i/count)=D3(1,i,1);
    end
end r=length(D4(1,:,2)) count=1; for i=count:count:r
    Dmean4(i/count)=mean(D4(1,1:i,2));
    x4(i/count)=D4(1,i,1);
    if i>count
        error4(i/count)=(Dmean4((i-count)/count)-Dmean4(i/count))/Dmean4((i-count)/count);
        xerror4(i/count)=D4(1,i,1);
    end
end r=length(D5(1,:,2)) count=1; for i=count:count:r
    Dmean5(i/count)=mean(D5(1,1:i,2));
    x5(i/count)=D5(1,i,1);
    if i>count
        error5(i/count)=(Dmean5((i-count)/count)-Dmean5(i/count))/Dmean5((i-count)/count);
        xerror5(i/count)=D5(1,i,1);
    end
end hold on plot(x*0.001, Dmean(:),'-.r') plot(x2*0.01,
Dmean2(:),'--b') plot(x3*0.1, Dmean3(:),'-.m') plot(x4,
Dmean4(:),'--g') plot(x5*10, Dmean5(:),'-.') plot([0 730],
[(M_fine*4.16^3)^(1/3) (M_fine*4.16^3)^(1/3)], '-.g') hold off
hx=xlabel('Time in Seconds') h_text = findobj(hx,'type','text');
set(h_text,'FontUnits','points','FontSize',12) hy=ylabel('Power
Ratio') h_text = findobj(hy,'type','text');
set(h_text,'FontUnits','points','FontSize',12)
h_legend=legend('\Delta t=0.001','\Delta t=0.01','\Delta
t=0.1','\Delta t=1','\Delta t=10', 'Richardson Extrapolation')
h_text = findobj(h_legend,'type','text');
set(h_text,'FontUnits','points','FontSize',12) htitle=title(['Mean
March vs. Time']) h_text = findobj(htitle,'type','text');
set(h_text,'FontUnits','points','FontSize',12) set(h_legend,
'position', [.45 .65 .45 .2]) print -djpeg100 meanmarch_dt01.jpg
hold on plot(xerror3*0.1, abs(error3*100)) plot([0 730], [0.005
0.005], '--y')
%plot([0 730], [-0.005 0.-005], '--y')
hold off
h_legend=legend('% Diff.', 'Upper Limit')
h_text = findobj(h_legend,'type','text');
```

```
set(h_text,'FontUnits','points','FontSize',12)
 set(h_legend, 'position', [.65 .45 .25 .2])
htitle=title(['Mean March Percent Error vs. Time']) h_text =
findobj(htitle,'type','text');
set(h_text,'FontUnits','points','FontSize',12) hx=xlabel('Time in
Seconds') h_text = findobj(hx,'type','text');
set(h_text,'FontUnits','points','FontSize',12) hy=ylabel('Power
Ratio') h_text = findobj(hy,'type','text');
set(h_text,'FontUnits','points','FontSize',12) print -djpeg100
meanmarch_error_dt01.jpg
```

## E.3 Data Collection, Variance, Mean and Plotting

```
%-------------------------------------------------------------------------%
%              - Mean Variance Collection and Analysis -                  %
%                          by: Hans D. Hamm                               %
%-------------------------------------------------------------------------%

  clear all;

%...Simulation Variables.....................................................
  V_in=4.16 % ambient flow velocity
  %...Load in Monitor Data from fluent.....................................
  %(1)bx20a10..............................................................
  D(1,:,:)=load('\bx20a10\bx20a10_aoa0\monitor-1.txt');
  D(2,:,:)=load('\bx20a10\bx20a10_aoa10\monitor-1.txt');
  D(3,:,:)=load('\bx20a10\bx20a10_aoa20\monitor-1.txt');
  D(4,:,:)=load('\bx20a10\bx20a10_aoa30\monitor-1.txt');
  D(5,:,:)=load('\bx20a10\bx20a10_aoa40\monitor-1.txt');
  D(6,:,:)=load('\bx20a10\bx20a10_aoa50\monitor-1.txt');

  E(1,1,1:6)=[0 10 20 30 40 50]; %angle of attack
  E(1,2,1)=20; % bx value
  E(1,3,1)=10;  % a
  E(1,4,1)=6;
  for i=1:6
      E(1,5,i)=mean(D(i,:,2));
      E(1,6,i)=var(D(i,:,2));
      E(1,7,i)=(mean(D(i,:,2)))^3/V_in^3;
  end
```